Imperial College London
Department of Electrical and Electronic Engineering

Data-Driven Stability-Constrained Optimisation for Software-Defined Power Systems with High IBR Penetration

Qian Chen

Supervisor: Prof. Goran Strbac

A thesis submitted to Imperial College London
for the degree of Doctor of Philosophy, April 2025

To my family and friends.

Declaration of Originality

The material contained within this thesis is my own work, except where other work is appropriately referenced. Any use of the first-person plural is for reasons of clarity.

Copyright Declaration

The copyright of this thesis rests with the author. Unless otherwise indicated, its contents are licensed under a Creative Commons Attribution-Non Commercial 4.0 International Licence (CC BY-NC).

Under this licence, you may copy and redistribute the material in any medium or format. You may also create and distribute modified versions of the work. This is on the condition that: you credit the author and do not use it, or any derivative works, for a commercial purpose.

When reusing or sharing this work, ensure you make the licence terms clear to others by naming the licence and linking to the licence text. Where a work has been adapted, you should indicate that the work has been changed and describe those changes.

Please seek permission from the copyright holder for uses of this work that are not included in this licence or permitted under UK Copyright Law.

Abstract

The high penetration of inverter-based resources (IBRs) represents both a challenge and an opportunity for modern power systems. While the reduced inertia and fast dynamics of IBRs complicate traditional stability paradigms, advancements in control strategies—such as virtual inertia, adaptive controls, and grid-forming inverters—offer promising paths to secure and resilient power system operation. However, the intermittent nature of renewable energy sources (RES) and the distinct characteristics of IBRs introduce new challenges in achieving stable, reliable, and efficient power system operation.

Hence, the evolution toward software-defined power systems (SDPS) is driven by the need to create a more resilient, flexible, and efficient grid capable of handling the complexities introduced by renewable energy integration and distributed generation. SDPS decouples control functions from the physical grid, enabling dynamic, real-time management through advanced software, high-speed communication, and centralized decision-making platforms.

This thesis develops robust preventive control strategies that optimize system operation and ensure grid security and stability by harnessing the rapid, precise control of IBR units and leveraging advanced parameter tuning within a software-defined power system framework. To achieve these goals, we investigate a diverse range of challenges spanning multiple domains.

One key issue this thesis addresses is the challenge of system frequency and low inertia. We integrate data-driven based frequency dynamics into an algebraic optimization framework and effectively utilise frequency support from various sources. At the transmission level, our data-driven approach optimizes system scheduling to minimize operating costs while ensuring frequency security by leveraging support from wind turbines adaptively.

Another issue tackled in this thesis is the stability challenge in inverter-dominated, carbon-neutral power systems, where poorly damped oscillations occur. We propose an optimal power flow framework that integrates data-driven small-signal stability constraints and dynamically optimizes inverter control parameters. A participation-based sampling strategy is used to define stability boundaries efficiently.

Acknowledgements

I am deeply grateful to my supervisor, Prof. Goran Strbac, for his exceptional mentorship and unwavering support throughout my PhD at Imperial. His insightful guidance and our stimulating discussions have been truly invaluable.

I also extend my sincere thanks to Dr. Fei Teng and Dr. Yunjie Gu, outstanding young lecturers from the Control & Power group at Imperial, whose inspiring research and engaging discussions have greatly enriched my work.

Sincere gratitude goes to Dr. Luis Badesa and Dr. Zhongda Chu, who have been more like friends than mere colleagues within the Control & Power group. Their wealth of insightful ideas and unwavering technical support proved invaluable throughout the course of the PhD.

Furthermore, I would like to thank my colleagues Dr. Yitong Li, Dr. Wangkun Xu, and Dr. Yue Zhu. Dr. Li's expertise in power electronics—particularly in system topologies and control algorithms—and his development of the open-source 'Simplus-Grid-Tool' for dynamic analysis and time-domain simulation have been invaluable. Dr. Xu has provided significant inspiration in optimization and machine learning, while Dr. Zhu's guidance on the participation-based grey-box approach has greatly contributed to my research.

Finally, I extend my gratitude to every reader who has taken an interest in this work. Completing a PhD requires considerable effort, and it is truly rewarding to see that my research on achieving power system stability resonates with others. I hope this thesis serves as a valuable resource to spark innovative ideas and contributes to our collective pursuit of a robust, reliable, and carbon-free power system.

Contents

Abstract **9**

Acknowledgements **11**

List of Acronyms **17**

List of Figures **21**

List of Tables **23**

1 Introduction **25**

1.1 Background and Motivation 25

1.2 Problem Statement and Research Scope 35

1.3 Original Contributions 38

1.4 Thesis Outline 40

1.5 Publications 42

2 Efficient Sampling for Data-Driven Frequency Stability Constraint via Forward-Mode Automatic Differentiation **43**

2.1 Introduction 45

2.2 Data-driven Frequency Stability Assessment 46

2.2.1 Dynamic Model 46
2.2.2 Frequency Stability 50
2.3 Gradient-based Sampling under Forward-Mode Automatic Differentiation 51
2.3.1 Forward-mode Automatic Differentiation 53
2.3.2 Gradient Surgery 55
2.3.3 Computation and Discussion 57
2.4 Case Study 58
2.5 Conclusion 61

3 Adaptive Droop Gain Control for Optimal Kinetic Energy Extraction from Wind Turbines to Support System Frequency 63

3.1 Introduction 64
3.1.1 Optimal FFS from a System Perspective 65
3.1.2 Modelling Approaches for System Frequency Security 67
3.1.3 Present Work 71
3.2 Adaptive Fast Droop Control Strategy 72
3.2.1 Model for Variable Speed WT System 73
3.2.2 Proposed Adaptive Fast Droop Control 76
3.3 Frequency-secured System Operation via Data-driven Constraints 81
3.3.1 Multivariate Optimal Classification Tree with Frequency-Security Guarantees 82
3.3.2 Second-Order Cone OPF with Mixed-Integer Linear Frequency-Security Constraints 87
3.4 Case Studies 88

3.4.1 Impact of System-Wide Conditions on Optimal $\widetilde{K}_{\text{sys}}$ 91

3.4.2 Assessment of Conservativeness and Reliability of Secure OCT(M) 95

3.4.3 Validation of Frequency-Security Constraints 98

3.4.4 Impact of Optimal FFS on Power System Operating Cost 100

3.5 Conclusion and Future Work 102

4 Efficient Sampling for Data-Driven Small-Signal Stability Constraints via Participation Analysis 104

4.1 Introduction 105

4.2 Participation-Analysis Sampling Based on Impedance Model 112

4.2.1 Preliminaries 112

4.2.2 Motivation 116

4.2.3 Feature Selection via Participation Analysis 118

4.2.4 Sampling Strategy Description 122

4.2.5 Practical Implementation 125

4.3 Small-Signal Stability Constrained OPF 127

4.4 Case Study 129

4.4.1 Performance of the Proposed Sampling Strategy 130

4.4.2 Performance of the Small-Signal Stability Constrained OPF 134

5 Conclusions and Future Work 136

5.1 Summary and Conclusion 136

5.2 Future Work 137

A Supplementary Material for Efficient Sampling for Data-Driven Frequency Stability Constraint via Forward-Mode Automatic Differentiation **141**

A.1 Derivation of $\dot{\omega}(t = 0^+)$ in (2.5) 141

A.2 Derivation of the Augmented ODE (2.8b) 142

A.3 Baseline Methods 143

A.3.1 Unrolling Differentiation 143

A.3.2 Finite Difference 144

Bibliography **144**

List of Acronyms

AD	Automatic Differentiation
ADG	Adaptive Droop Gain
ANN	Artifical Neural Network
BMI	Bilinear Matrix Inequality
CART	Conventional Decision Tree
COI	Centre-of-Inertia
DFIG	Doubly Fed Induction Generatior
DT	Decision Tree
FDC	Fast Droop Control
FFS	Fast Frequency Support
FM	Forward-Mode
FN	Frequency Nadir
GB	Great Britain
GFM	Grid-Forming
GSC	Grid-Side Converter
IBG	Inverter-Based Generation
IBR	Inverter-Based Resources

JVPs Jacobian-Vector Products

KE Kinetic Energy

LCF Load Frequency Control

MILP Mixed-Integer Linear Programming

MPPT Maximum Power Point Tracking

ODE Ordinary Differential Equation

OCT Optimal Classification Tree

OPF Optimal Power Flow

PMSG Permanent Magnet Synchronous Generator

PLL Phase-Locked Loop

RES Renewable Energy Sources

RoCoF Rate of Change of Frequency

RSC Rotor-Side Converter

SDP Semideinite Programming

SDPS Software-Defined Power Systems

SG Synchronous Generator

SI Synthetic Inertia

SM Synchronous Machines

SOCP Second-Order Cone Programming

SFD Second Frequency Dip

SS Steady-State

SSSC-OPF Small-Signal Stability Constrained Optimal Power Flow

SVM Support Vector Machine

VSM Virtual Synchronous Mode

WF Wind Farm

WT Wind Turbine

List of Figures

1.1 Scheme of power system operation within the framework of the thesis 37

1.2 Research workflow in this thesis 38

2.1 Two examples of the proposed sampling method: (a). Search from 'stable' sample to 'unstable' sample; and (b). Search from 'unstable' sample to 'stable' sample. 59

3.1 Turbine power characteristics (pitch angle $\beta = 0°$). 74

3.2 Pitch angle control system. 75

3.3 Control scheme for the proposed adaptive droop gain. 81

3.4 Demonstration model of multivariate OCT. 84

3.5 Concise equivalent model for multivariate OCT demonstration. 86

3.6 IEEE 14-bus test system. 89

3.7 Results for Case A-1: (a) System frequency; (b) Active power output of WF; (c) Rotor speed of WTs. 92

3.8 Optimal $\widetilde{K}_{\text{sys}}$ versus wind speed and wind penetration level '*pl*'. 94

3.9 Prediction performance versus negative sample's weight ω. 96

3.10 Learning curve of OCT(M): relationship between prediction accuracy and training set size. 98

3.11 Three-day wind and load profiles and optimal $\widetilde{K}_{\text{sys}}$. 98

3.12 Dynamic simulations from five different OPF solutions. 99

3.13 Impact of optimal FFS on the weekly cost of frequency services. 101

3.14 Weekly generation cost with different control strategies, for a 50% wind penetration level. 101

4.1 Demonstration of the whole-system admittance model. Virtual voltage injection $\hat{v}$ to generate Δi. 114

4.2 Feature selection cycle based on participation analysis. 119

4.3 Sampling strategy framework. 125

4.4 Modified IEEE 14-bus test system. 130

4.5 Bode diagram of whole system admittance $\hat{Y}_{kk}$ at apparatus bus in *dd* axis. . . . 131

4.6 Participation analysis of the critical under-damped mode in Stage-1 and Stage-2 of the sampling strategy, where the results in Stage-2 are normalised to the base value. 131

4.7 Overall stability observation during sampling. 132

4.8 Comparison of the generation costs under one selected day for three OPF scenarios 134

List of Tables

2.1 Power System Parameters 58

2.2 Performance comparison on different gradient-based sampling methods. The errors are the maximum absolute percentage errors with respect to the solution by Unrolling AD. The performances are recorded based on 5 runs. 62

3.1 Summary of control schemes for FFS from WTs 66

3.2 Parameters of Variable Speed Wind Turbine 75

3.3 Thermal generation mix within test case 90

3.4 Assessment indices of three classification models 96

3.5 Frequency nadir assessment 99

3.6 Dispatch results under Secure vs. Standard OCT(M) 99

Chapter 1

Introduction

In this chapter, the background of the thesis is introduced, explaining the motivation of related research problems. The original contributions of the work and the outline of the thesis are presented, followed by publications related to this thesis.

1.1 Background and Motivation

With ever-increasing global awareness of the environmental issues associated with conventional synchronous machine (SM)–based generation and the sustainability benefits of renewable energy sources (RES), modern power systems are undergoing a profound transformation. This shift—largely driven by the rapid expansion of wind and solar generation—is central to ambitious decarbonisation strategies worldwide. For example, the European Union and the United

Kingdom have both set targets to achieve climate neutrality by 2050, while China has committed to peaking its emissions before 2030 and reaching carbon neutrality by 2060 [1–3]. The latest technical reports underscore that, despite their environmental advantages, the intermittent nature of RES and the distinctive characteristics of their power converter interfaces introduce significant challenges in grid control, operation, and planning. According to the International Energy Agency's World Energy Outlook 2023 [4] and the International Renewable Energy Agency's Renewable Capacity Statistics 2023 [5], issues such as maintaining grid stability, managing voltage fluctuations, and ensuring robust transient response have become focal points for researchers and policymakers. Furthermore, recent industry analyses [6, 7] emphasize that addressing these challenges requires the development of advanced control strategies, innovative energy management systems, and improved forecasting techniques to ensure the reliable integration of RES into modern power networks.

In general, control strategies for fast frequency support (FFS) from variable speed wind turbines (WTs) without additional energy storage systems are categorised into two groups [8]. The first group is de-loading control, which operates WTs in a suboptimal mode with a certain amount of reserved power available, to be used in the event of a frequency contingency [9, 10]. Known as overproduction control, the second group is based on providing an additional power injection temporarily from stored kinetic energy [11].

The de-loading control strategy is not preferred for implementation in slightly or even moder-

ate wind-penetrated systems, due to its suboptimal efficiency during normal operation. WT operators may forego important revenues from selling energy, as de-loading implies some power curtailment. Therefore, overproduction control is typically more advantageous, since WTs are enabled to operate following a maximum-power-point-tracking (MPPT) curve under normal conditions [12]. However, several issues may arise from overproduction control, such as a second frequency dip (SFD) and over-deceleration [11, 13].

Overproduction control resorts to the available kinetic energy (KE) stored in WTs, which depends on the pre-disturbance rotor speed and the minimum permissible rotor speed that ensures the mechanical stability of WTs [13]. A temporary overproduction of the power delivered to the grid results in a deceleration of the rotor speed, which drives the operating points of WTs away from the MPPT curve, leading to a lower conversion efficiency of wind power. To regain the maximal power capture and the frequency regulation capability to tackle consecutive under-frequency events, a recovery process of WT's rotor speed is necessary. The rotor speed recovery may entail an output power drop of WTs following the KE extraction process, possibly giving rise to an SFD [14].

Based on the foregoing analysis, to lessen or even eliminate an SFD, it is indispensable to prevent a large and steep electrical power drop from WTs at the end of a rotor deceleration process, which necessitates a smooth decline of reference power for the WTs. An extensive research effort has been conducted to alleviate or erase the SFD. The minimum rotor speed has

been preset considering the rate of change of mechanical power versus rotor speed to prevent large power drops [15]. Several shaping functions of the power drop curve have been proposed in [11] to retard a large power drop at the end of the frequency-support period.

On the other hand, several ameliorative strategies have been put forward to avoid an over-deceleration of WTs during the frequency-supporting process. In [16], the WT's post-fault power output trajectory has been devised with significant attention on the chosen rotor speed at the beginning of rotor speed restoration of WTs. Reference [17] has proposed a scheme by navigating the electrical power output of WTs as a specified Gaussian distribution trajectory controlled by the computed standard deviation values, which guarantees the declining rotor speed strictly larger than the minimum permissible rotor speed. The authors in [13,18] employed an adaptive droop gain (ADG) in the control loop, which is temporally proportional to the KE stored in WTs to improve the frequency nadir (FN) without the possibility of an over-deceleration. Notably, ADG serves as a function of the WTs' real-time rotor speed and/or Rate of Change of Frequency (RoCoF) of the system to maximise the frequency-supporting capability.

Another challenge due to the increasing deployment of inverters in power systems, raising concerns about system dynamics and stability [19]. Incidents have linked inverters to issues such as unexpected disconnections during fault events and poorly damped responses to voltage fluctuations [20]. It is particularly problematic that instability may arise in the phase-locked

loops of grid-following inverters integrated into a grid with low strength, often denoted as a weak grid [21]. Operators noted the emergence of poorly damped oscillations in areas where inverters dominate, expecting further investigation [22]. These stability challenges may intensify as inverter-based resources play a pivotal role in carbon-neutral power systems.

As previously elaborated, potential dynamic stability concerns, including small-signal instability, may manifest when integrating these resources into a weak grid [23]. In addition, the variable nature of renewable resources, such as wind and solar, possibly exposes power systems to small-signal instability, as a result of rapid variations of operating points of systems [24]. On the other hand, non-synchronous generations based on IBRs are steadily displacing conventional generators in current power systems, by which the inverters generally fail to enhance system inertia and thus small-signal stability [25]. Therefore, the small-signal security assessment is warranted to be carried out in the course of economic dispatching, such as Optimal Power Flow (OPF). The Small-Signal Stability Constrained Optimal Power Flow (SSSC-OPF) is an exemplary model that provides comprehensive re-dispatch details to ensure small-signal stability, taking into account both economic goals and technical limitations. Modeling the SSSC-OPF directly is challenging due to the spectral abscissa's implicit dependence and non-Lipschitz behavior within the system state matrix. The papers solving SSSC-OPF are categorised as follows, considering small-signal stability constraints endowed with the non-smooth and non-linear nature.

- Iterative methods utilising eigenvalue sensitivities: This group of methods have used first-order and/or second-order Taylor series expansion of small-signal stability constraints where the gradients and/or Hessian matrices are evaluated by perturbations or computed by closed-form formulations in each iteration step. [26] developed an SSSC-OPF model to maintain security under stressed conditions by approximating the small-signal stability constraint with a first-order Taylor series expansion and successively solving SSSC-OPF. In addition to first-order sensitivities, [27–30] have also utilized second-order sensitivities to track dominant eigenvalues as accurately as possible and facilitate the efficiency of the iteration process.

- Noniterative methods based on semidefinite programming (SDP) from Lyapunov stability criterion: Without resorting to eigenvalue analysis, this category of methods derives explicit and equivalent small-signal stability constraints through working over differential-algebraic equations describing dynamic and algebraic relationships in power systems. Building on the insights from [31], [32] proposed to use a bilinear matrix inequality (BMI) for small-signal stability and SDP with objective penalization for efficient large-scale system modelling. To ensure sufficient stability margins in inverter-based microgrids during optimal power generation, [33] applied SDP and parabolic relaxation to address nonlinear, non-convex BMIs, preserving the conditions for small-signal stability [34], which is prohibitive for the current optimization tools.

Nevertheless, iterative methods relying on eigenvalue analysis face substantial computational challenges due to the repeated updates of the gradient and/or Hessian matrix, coupled with model linearization after each iteration, resulting in significant time consumption. In contrast, non-iterative methods based on SDP bypass these iterative updates but present two key challenges. First, ensuring a guarantee of convergence is essential to secure reliable solutions within a reasonable timeframe, especially in non-convex optimization problems where convergence is not inherently assured. Second, developing tighter convex relaxations is critical for enhancing solution accuracy by minimizing the gap between the relaxed and true optimal solutions, making the approach more effective and suitable for real-world applications. Furthermore, the aforementioned methods cannot be utilized when analytical models are unavailable, a likely scenario, as state-space models require detailed knowledge of each machine's hardware design and control algorithms. Unfortunately, this information is often inaccessible due to manufacturers withholding it and the lack of standardization across suppliers [22].

By reducing reliance on iterative eigenvalue computations and minimizing dependence on SDP relaxations, data-driven methods lower computational burdens and enhance real-time decision-making [35]. These methods effectively capture the system's underlying properties by concentrating on key security attributes and the most relevant features, eliminating the need for complex model-based analysis while preserving essential dynamic information [36]. Advancements in data-driven methods have reshaped power system analysis, enabling more effective

stability assessment and control. The Koopman operator framework has emerged as a powerful technique for capturing system dynamics and estimating the region of attraction through dominant eigenfunction analysis, eliminating the reliance on explicit system models [37]. Similarly, data-driven Lyapunov functions have been developed using real-time measurement data, offering a model-free approach to stability certification while bypassing traditional analytical formulations [38]. In operational stability analysis, techniques such as inertia estimation and frequency monitoring have been seamlessly integrated with wide-area measurement systems, leveraging machine learning algorithms for real-time grid monitoring [39]. Model Predictive Control has also benefited from data-driven enhancements, enabling adaptive and optimal decision-making in rapidly changing environments [40]. Furthermore, reinforcement learning has advanced learning-based controllers by enabling autonomous system operation under uncertain and dynamic conditions [41]. Collectively, these innovations demonstrate the transformative potential of data-driven approaches in modern power system stability and control through adaptive, scalable, and model-free frameworks.

Recent developments in machine learning (ML) and hybrid approaches for power system dynamic security assessment (DSA) have extended beyond conventional data-driven methods. In particular, a growing body of research explores embedding physics-based constraints, integrating sampling optimization techniques, and leveraging model-informed learning architectures.

Traditional DSA methods rely heavily on detailed numerical simulations of system dynamics

governed by ordinary differential equations (ODEs). In recent work, hybrid approaches have emerged, where machine learning models learn from data generated by ODE-based simulations. For example, Stiasny et al. [42] introduce a modular ML framework for power system security assessment that integrates ODE-based simulations with neural network learning pipelines. In such "ML-in-the-loop" designs, a surrogate model approximates the security margin computed from dynamic simulations, providing fast inference while retaining physical interpretability.

Several works incorporate ODEs for a few simulation steps to initialise or guide ML model training. The notion of embedding "physics-informed" insights into ML models is further exemplified in Ren and Xu [43], where a generative adversarial network (GAN) is used to augment missing PMU measurements, thereby supporting dynamic security assessment even under incomplete data. This contrasts with purely black-box methods and reflects a shift toward hybrid and resilient DSA models.

In terms of data generation, significant progress has been made toward efficient and targeted sampling for classifier training. The literature has consistently shown that the accuracy and generalizability of DSA models—especially classifiers—depend strongly on the information content and representativeness of the training database.

Importance sampling techniques have been proposed as a solution to the computational challenges of rare-event estimation in power systems. For instance, Hamon et al. [44] introduce an efficient importance sampling scheme tailored to probabilistic security assessment. Their

method uses second-order approximations of the stability boundary to guide sampling toward high-impact operating points, thereby reducing Monte Carlo simulation effort by several orders of magnitude. Similar benefits are seen in Krishnan et al. [45], who present a two-stage sampling method for decision tree-based voltage stability assessment. Their approach includes a directed walk to identify regions near the classification boundary, followed by biasing sampling distributions via importance weighting.

The use of directed walk strategies, as seen in the framework proposed by Stiasny et al. [42], further strengthens model training by enriching datasets with samples concentrated around the stability boundary. Such boundary-focused data generation improves classifier sharpness and reduces false positive/negative rates near critical margins. Moreover, ensemble methods leveraging multiple classifiers trained on diverse feature subspaces, as in Xu et al. [46], can provide robustness and interpretability in classification tasks for dynamic security.

On the probabilistic side, the incorporation of stochastic forecast error distributions in security analysis has gained traction. Hamon et al. [44] discuss how risk measures derived from forecast uncertainty can inform real-time control decisions. The corresponding sampling distributions, often modelled using Gaussian copulas or non-Gaussian marginals (e.g., Beta for wind), must be carefully tuned to reflect realistic operating conditions.

Regarding system observability and incomplete data, the work of Ren and Xu [43] offers a data-driven solution that bypasses conventional observability constraints. Their GAN-based

model recovers missing measurements and integrates seamlessly with ensemble DSA classifiers, enhancing reliability without increasing infrastructure costs.

Finally, several authors advocate embedding ML surrogates within traditional optimization-based frameworks such as security-constrained optimal power flow (SCOPF). For instance, Capitanescu et al. [47] explore contingency filtering and ranking within preventive SCOPF workflows, where ML-based classification or regression could offer scalable surrogates for post-contingency evaluations.

1.2 Problem Statement and Research Scope

This thesis examines the challenges of operating power systems with a high proportion of IBRs and presents a novel scheduling strategy that leverages the flexible control features of these resources. The study demonstrates that both system-level optimization and device-level control are crucial to maintaining stability, with each level informing and enhancing the other. In particular, system-level analysis establishes the performance targets for device operations, while individual IBR units contribute essential support services. Relying solely on device-level control can be insufficient, especially during transient events when IBRs approach their current and power limits. An effective solution requires coordinated management across the entire system to ensure stability and optimize economic performance. Unlike traditional approaches that treat

system optimization and device control as separate challenges, this work integrates stability constraints directly into the scheduling framework, accounting for local device capabilities.

As shown in Fig. 1.1, the process begins by fitting a statistical model to historical operating data. Next, this model is used to sample a range of potential operating points that may occur in the upcoming hours or days. A series of contingency scenarios is simulated for each sampled point to determine post-fault security. Finally, the pre-fault variables serve as features and the post-fault security outcomes as labels to train a classifier using standard machine learning techniques [48]. The classifier can be encoded into the optimisation framework while maintaining tractability. Thus, power system scheduling considers data-driven stability constraints, sets operating points and produces optimal parameters for local controllers. This research first embeds stability requirements into the optimization model. Then it enables the scheduling process to determine optimal control parameters, bridging the gap between system-level strategies and device-level control. It is worthwhile noting that the system-level strategy is denoted by dashed lines and device-level control is plotted in solid lines. The thesis has not covered the state estimation work, but leaving the block here to reserve the framework's integrity.

The objective is to reduce overall system operating costs while ensuring stability and security during the scheduling process by optimally managing various services and variables. As depicted in Fig. 1.2, presenting the stability categories in power systems. Note that the black part represents the stability categories of generator-based power systems, and the blue part

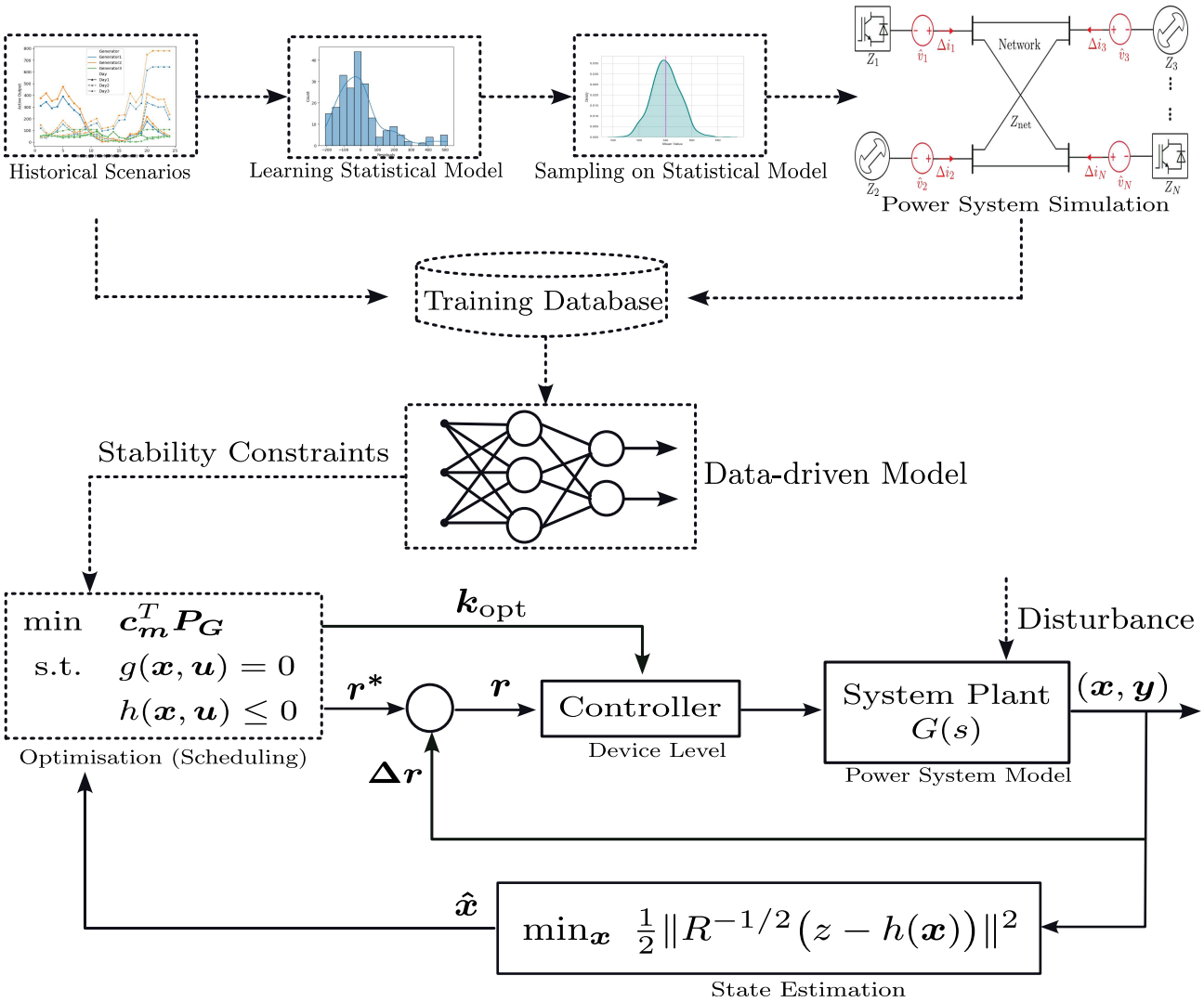

Figure 1.1: Scheme of power system operation within the framework of the thesis

represents the new categories introduced by converter controls [49]. The workflow in the thesis follows three main steps:

a. Modelling System Dynamics: Accounting for IBR characteristics and their interactions to establish the system dynamics.

b. Developing Stability Criteria: Developing explicit stability criteria describing data-driven models, mapping the relationship between power system operating conditions and their corresponding security status.

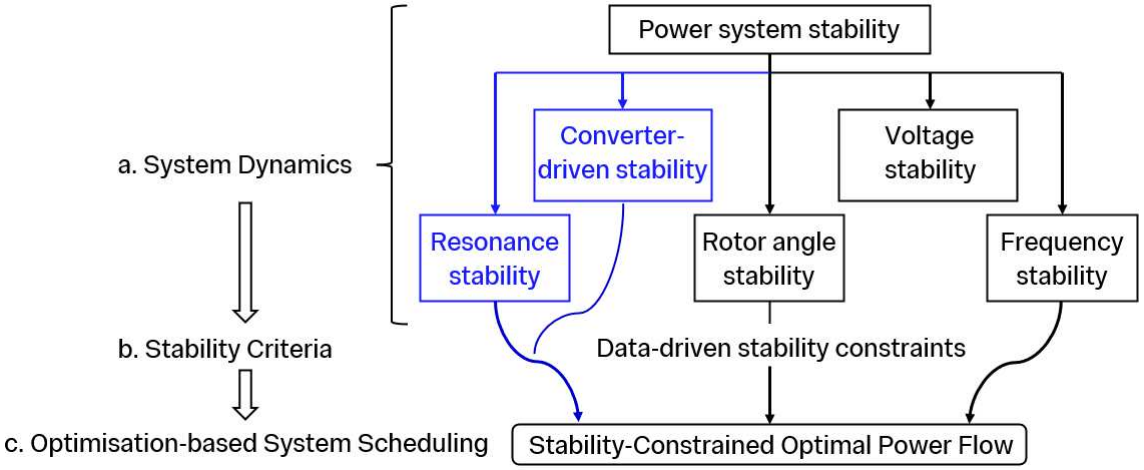

Figure 1.2: Research workflow in this thesis

c. Integrating into the Optimisation Model: Maintaining the stability criteria's tractability and incorporating them into a generalised optimisation framework capable of handling broader constraints.

1.3 Original Contributions

To address the challenges outlined above, this thesis presents the following two key contributions:

- **Formulation of Data-Driven Stability Criteria Linking Static Operating Points and Inverter Controls**

  We introduce a novel formulation of frequency and small-signal stability criteria as data-driven functions of both static system-level operating points and inverter control parameters (e.g., virtual inertia, damping coefficients). This framework allows the stability

assessment to reflect not only the operating condition of the grid, but also the tunable dynamics of inverter-based resources (IBRs). By embedding inverter control degrees of freedom into the stability formulation, we bridge the gap between system-level operation and device-level control. This connection enables co-optimisation of IBR settings within day-ahead scheduling, thereby unlocking new control flexibility that can enhance grid security and operational efficiency.

- **Efficient Sampling Strategy for Generating Informative and Balanced Training Data**

  To improve classifier performance near stability boundaries, we propose a two-pronged data sampling strategy that targets critical operating points:

  a. Forward-Mode Automatic Differentiation (FMAD):A sensitivity-based sampling method designed for state-space stability models. It computes the derivatives of stability margins with respect to control variables, enabling efficient gradient-guided sampling near critical boundary regions.

  b. Participation-Based Sampling: A lightweight technique developed for impedance-based stability models. It identifies the most influential control and state variables through participation analysis, directing sampling toward high-impact directions in the operating space.

1.4 Thesis Outline

This thesis is structured into four technical chapters, each dedicated to a specific contribution outlined above. Given the diverse topics covered, each chapter includes its own targeted literature review.

- Chapter 2 focuses on a gradient-based sampling method to efficiently compute the Jacobian of various frequency criteria with respect to stationary operating points, we construct an augmented system of ODEs that incorporates both the original states and their corresponding tangent states.

- Chapter 3 proposes an ADG control strategy to fully utilise the frequency-supporting capability of WFs, while the ADG parameter is introduced as a decision variable in the data-driven frequency-security constraints, and optimised within a system scheduling framework.

- Chapter 4 develops an innovative sampling scheme that employs participation analysis to pinpoint critical samples near the stability boundary, thereby enriching the training database with essential information and proposes a constrained logistic regression-based stability assessment model to capture the most recent static operating status, dynamic IBR control strategies, and stability performance. Once trained, the stability assessment is encoded as a stability constraint into real-time OPF with limited computation and cost

overhead.

Finally, Chapter 5 distills the principal findings of this thesis and outlines directions for future research.

1.5 Publications

Articles in peer-reviewed journals:

[1] **Q. Chen**, W. Xu and G. Strbac, "Unlocking Flexibility of Heterogeneous IBRs for Data-Driven Stability-Constrained OPF," in IEEE Transaction on Power Systems, under review.

[2] **Q. Chen**, L. Badesa, Z. Chu and G. Strbac, "Adaptive Droop Gain Control for Optimal Kinetic Energy Extraction from Wind Turbines to Support System Frequency," in IEEE Access, 2024.

Conference contributions:

[3] Xu, Wangkun, **Qian Chen**, Pudong Ge, Zhongda Chu, and Fei Teng. "Efficient Sampling for Data-Driven Frequency Stability Constraint via Forward-Mode Automatic Differentiation." In 2024 IEEE PES Innovative Smart Grid Technologies Europe (ISGT EUROPE), pp. 1-5. IEEE, 2024.

Chapter 2

Efficient Sampling for Data-Driven Frequency Stability Constraint via Forward-Mode Automatic Differentiation

Efficient and balanced sampling of stable and unstable operating points is a critical challenge in frequency stability analysis. Conventional random sampling techniques often produce imbalanced datasets, undermining the performance of data-driven models that assess stability criteria. This chapter introduces a novel gradient-based data generation approach that directly

tackles this sampling challenge by leveraging forward-mode automatic differentiation. In our method, the original dynamic system is augmented with additional states that capture the sensitivities of the system's variables, allowing the entire augmented system to be solved with any ODE solver in a single pass. Furthermore, to address conflicting gradients stemming from multiple frequency stability criteria, we employ a gradient surgery technique that projects each gradient onto the normal plane of the others. Implementation details and source code are available at `https://github.com/xuwkk/frequency_sample_ad`.

2.1 Introduction

Ensuring stability in power systems is fundamental for maintaining secure and reliable operations [50]. The growing integration of renewable energy sources has led to reduced system inertia, increasing susceptibility to disturbances and cyber-attacks [51]. This has prompted significant research into incorporating stability constraints directly into system operations. Depending on the chosen system model and type of stability under consideration, different mathematical formulations are used to embed these constraints into solvable optimization problems.

In small-signal stability analysis, the dominant eigenvalue of the system state matrix serves as a stability indicator [52], and its sensitivities are often used as gradients within optimization routines like sequential quadratic programming and interior-point methods. On the other hand, frequency stability is more difficult to assess, as it depends on the dynamic response following a disturbance, which is typically governed by differential equations. Some studies have derived approximate frequency constraints in closed-form, capturing metrics like steady-state frequency deviation, nadir, and RoCoF [53, 54]. However, these simplifications often sacrifice accuracy for analytical convenience.

Time-domain simulations retain full system dynamics but are computationally intensive when embedded in optimization frameworks. This challenge has led to growing interest in data-driven approaches for frequency stability assessment [48, 55, 56].

The effectiveness of such data-driven models relies heavily on the quality of the training data [57]. A representative dataset must include both stable and unstable operating points and should ideally focus on points close to the actual decision boundary [52]. Yet, without access to gradient information, it is difficult to sample informative points strategically. As a result, random sampling remains the default in many studies [58], despite its inefficiency.

To address this, our work introduces a gradient-informed data sampling technique. We formulate an augmented system of ODEs that includes both the original system dynamics and their tangent counterparts, enabling computation of Jacobians with respect to steady-state operating points. These tangent equations form a linear system that can be integrated simultaneously with the original system. Additionally, to resolve conflicts between gradients from different frequency stability criteria, we adopt a technique known as gradient surgery, which eliminates inconsistent components and improves sampling effectiveness.

2.2 Data-driven Frequency Stability Assessment

2.2.1 Dynamic Model

While the proposed algorithm is broadly applicable to dynamic power system models governed by a variety of stability metrics, this work specifically focuses on frequency stability under load frequency control (LFC) with adaptive synthetic inertia. In particular, we consider wind tur-

bines operating in grid-forming (GFM) mode, where system dynamics are governed by nonlinear ordinary differential equations (ODEs), as detailed in [59].

We begin with a classical second-order representation of the frequency dynamic model with state feedback control using the adaptive model [60], expressed as:

$$M \cdot \dot{\omega} = \Delta P + q - D \cdot \omega \tag{2.1a}$$

$$\tau \cdot \dot{q} = -r^{-1} \cdot \omega - q \tag{2.1b}$$

In this work, we adopted the aggregated multi-machine system frequency response model proposed in [61]. This model unifies the dynamic behaviour of synchronous generators, virtual synchronous generators, and droop-controlled grid-forming inverters into a swing-equation-based representation. It offers a simplified yet effective means of capturing the system-wide frequency response by aggregating inertia and damping parameters. This approach is chosen for its analytical tractability and compatibility with control-aware, data-driven stability assessment. While it does not model saturation effects or nonlinear protective actions such as current or voltage limiters, it has been shown to provide accurate representations of system frequency dynamics under small and moderate disturbances. For large-disturbance scenarios where nonlinearities dominate, further modeling extensions would be required. This limitation is noted, and the scope of applicability is confined accordingly in this study. Here, M and D

denote the normalised inertia and damping coefficients, respectively. The variable ω represents frequency deviation, while q and ΔP correspond to perturbed mechanical and electrical power inputs, with ΔP representing a step disturbance. Parameters r and τ are the governor's droop gain and time constant.

Assuming a step disturbance ΔP and eliminating q, the equations reduce to a second-order differential equation for ω:

$$\ddot{\omega} = -\left(\frac{D}{M} + \frac{1}{\tau}\right)\dot{\omega} - \left(\frac{1}{r\tau M} + \frac{D}{\tau M}\right)\omega + \frac{\Delta P}{\tau M} \tag{2.2}$$

Introducing the state vector $x = [\omega, \dot{\omega}]^T$, we rewrite the dynamics in state-space form as:

$$\dot{x}_1 = x_2 \tag{2.3a}$$

$$\dot{x}_2 = -\left(\frac{1}{r\tau M} + \frac{D}{\tau M}\right)x_1 - \left(\frac{D}{M} + \frac{1}{\tau}\right)x_2 + \frac{\Delta P}{\tau M} \tag{2.3b}$$

We then incorporate a converter operating in Virtual Synchronous Machine (VSM) mode, where inertia M and damping D are modulated through full-state feedback control [62]:

$$\begin{bmatrix} M \\ D \end{bmatrix} = \begin{bmatrix} M_0 \\ D_0 \end{bmatrix} - \begin{bmatrix} K_{11} & K_{12} \\ K_{21} & K_{22} \end{bmatrix} \begin{bmatrix} x_1 \\ x_2 \end{bmatrix} \tag{2.4}$$

In this formulation, M_0 and D_0 represent the nominal inertia and damping values, and the matrix K contains the adaptive control gains. Substituting (2.4) into the state-space model (2.3) yields the closed-loop system for the LFC dynamics with adaptive synthetic inertia:

$$(2.3), ; (2.4), ; x(t=0) = [0, \dot{\omega}(t=0^+)]^T \tag{2.5}$$

The initial frequency derivative after a disturbance is given by:

$$\dot{\omega}(t=0^+) = \frac{M_0 - \sqrt{M_0^2 - 4K_{12}\Delta P}}{2K_{12}} \tag{2.6}$$

A full derivation of this expression is available in Appendix A.1. Note (2.6) should keep consistent even under the case of 'without feedback control', implying (2.6) becomes $\dot{\omega}(t=0^+) = \frac{\Delta P}{M_0}$ when no feedback control implemented, i.e. matrix $K = \mathbf{0}$. This formulation also allows us to characterise the admissible range for the gain K_{12} so that $M_0^2 - 4K_{12}\Delta P \geq 0$. It can be further verified that for any negative disturbance $\Delta P < 0$, the initial frequency derivative satisfies $\dot{\omega}(t=0^+) \leq 0$ regardless of the chosen K_{12}, through examining the positivity or negativity of the enumerate and denominator in (2.6).

2.2.2 Frequency Stability

Frequency stability is typically assessed using three key metrics: maximum admissible Rate of Change of Frequency (RoCoF) denoted as $\dot{f}_{max}$, maximum frequency deviation Δf_{max}, and maximum admissible frequency deviation at quasi-steady-state f_{max}^{ss}. In practical systems, ROCOF is measured using devices such as phasor measurement units (PMUs), which estimate frequency derivatives over short time windows using filtering and numerical differentiation. These measurements are not instantaneous but time-averaged to reduce noise and improve reliability.

In this work, I adopt the analytical instantaneous ROCOF, defined as the derivative of frequency at the initial moment of disturbance. While this differs from practical measurements, it serves as a meaningful proxy for assessing initial frequency response trends in offline studies. This abstraction allows consistent comparison across operating conditions and facilitates tractable analysis within the system frequency response model. In our analysis, the simulation spans the interval $t \in [0, T]$, where T is the total simulation duration. The time instances at which each metric reaches its critical value are labeled t_{rocof}, t_{nadir}, and $t_{ss} = T$, respectively.

Since the system dynamics described by (2.5) are nonlinear, there is no closed-form time-domain solution available, as in prior work [59, 62]. Therefore, identifying these critical time points requires numerically solving the full dynamic model. This presents a challenge when attempting to embed frequency stability constraints directly into an optimisation framework,

as it demands explicit, differentiable formulations of these criteria, which will be discussed in a detailed level in Section 3.1.2.

For linearised versions of (2.5), it is sometimes possible to obtain analytical expressions under simplifying assumptions. These reveal how stability metrics depend on parameters such as inertia M, droop gain r, and damping D [63]. However, even in the linear case, incorporating such expressions directly into optimisation problems remains nontrivial.

Given the inherent difficulty of encoding either the nonlinear dynamics or their linear approximations within optimisation constraints, data-driven approaches have emerged as a practical alternative. These methods aim to learn tractable surrogate models—such as convex or mixed-integer linear approximations—that map operating conditions (e.g., control parameters K from the ODE model) to the three frequency stability metrics.

2.3 Gradient-based Sampling under Forward-Mode Automatic Differentiation

In this section, we study how to efficiently construct the dataset $\theta = [K_{11}, K_{12}, K_{21}, K_{22}]^T \times y \in \mathcal{D} = \mathcal{X} \times \mathcal{Y}$ under predefined disturbances ΔP. $y \in 0, 1$ with 0 representing a stable operation such that all three criteria are satisfied. We assume that there exists a dataset $\mathcal{D}_0$ of historical randomly-sampled operating conditions. The dataset is either insufficient in size or

strongly biased to one class, and our goal is to efficiently increase the size of the dataset with **controllable** labelling.

In the scope of this chapter, I focus on a fixed operating condition, meaning the dataset θ is constructed by varying feedback gains while keeping the underlying system operating point constant. This approach allows a clean analysis of the influence of control design on stability. Nevertheless, the proposed method can be extended to varying operating conditions by linearising the system at multiple representative operating points and applying the same gain scheduling procedure to each case. This would allow gain sets to be selected adaptively based on real-time system conditions.

In general, denote the non-linear closed-loop dynamic (2.5) as

$$\frac{dx(t)}{dt} = f(x(t), \theta), \quad x(t=0) = x_0 \tag{2.7}$$

When the stability label y' for a sample θ' equals 0 (stable operating point), an efficient sampling strategy may be to find an unstable sample $\bar{\theta}'$ which is the "closest" to the original sample θ'. Intuitively, such a sampling method may construct a dataset that can better represent the true stability boundary and give benefits in training the data-driven assessor with less data. One direct consideration is to use the local sensitivity of θ to iteratively approach the stability boundary. Similar consideration has been adopted in sampling data for assessing small-signal

stability [52]. However, as neither $x(t)$ has a closed form nor the critical t values can be specified in advance, the sensitivity-based method needs to be reconsidered for frequency stability.

The sampling strategy proposed here assumes that the stability boundary is locally smooth and that the nearest points to the boundary are most informative for learning. While this is effective in many cases, it may be suboptimal if instability regions are non-contiguous, highly non-convex, or fractured across the control space. In such situations, more global or adaptive sampling strategies may be needed to ensure full boundary coverage and avoid missing isolated unstable pockets.

2.3.1 Forward-mode Automatic Differentiation

Our objective is to compute the sensitivity of the system state $x(t)$ with respect to the parameters θ. This is characterized by the Jacobian matrix $\frac{\partial x(t)}{\partial \theta}$ evaluated at specific time instances $t \in t_{ss}, t_{rocof}, t_{nadir}$, which fully captures the direction in parameter space for updating θ.

To compute $\frac{\partial x(t)}{\partial \theta}$ efficiently, we adopt forward-mode automatic differentiation (FMAD). The key idea is to augment the original ODE system with additional equations that track the evolution of sensitivities—referred to as *tangent vectors*—throughout the integration.

Given that $\theta \in \mathbb{R}^4$, we define four new state variables $\hat{x}_i = \frac{\partial x}{\partial \theta_i} = \frac{\partial x}{\partial \theta} e_i$ for $i = 1, \ldots, 4$, where $e_i \in \mathbb{R}^4$ is the standard basis vector with a one in the i-th position. The augmented ODE

system under FMAD can be written as:

$$\frac{dx(t)}{dt} = f(x(t), \theta) \tag{2.8a}$$

$$\frac{d\hat{x}_i(t)}{dt} = \frac{\partial f}{\partial x}\hat{x}_i(t) + \frac{\partial f}{\partial \theta}e_i, \quad i = 1, \ldots, 4 \tag{2.8b}$$

The corresponding initial conditions are given by:

$$x(t = 0^+) = x_0 \tag{2.9a}$$

$$\hat{x}2(t = 0^+) = \begin{bmatrix} 0 & \frac{\partial \dot{\omega}(t=0^+)}{\partial K12} \end{bmatrix} \tag{2.9b}$$

$$\hat{x}_i(t = 0^+) = 0, \quad i = 1, 3, 4 \tag{2.9c}$$

A full derivation is provided in Appendix A.2. It is worth noting that the initial value of $\hat{x}_2$ depends on the controller parameters K. With a **single** call to **any** standard ODE solver on the augmented system (2.8), one obtains both the solution $x(t)$ to the original system (2.7) and the complete set of sensitivities $\frac{\partial x(t)}{\partial \theta_i}$ for $i = 1, \ldots, 4$ over the time horizon $t \in [0, T]$.

Compared to the original ODE (2.7), the FMAD-augmented system introduces four additional linear *inhomogeneous differential equations*, each with non-zero initial conditions, enabling efficient and accurate sensitivity analysis.

It is noted that assigning stability labels still requires evaluating the system's dynamic response by solving the underlying differential equations. While this introduces computational cost, the proposed sampling method is designed to minimise the number of simulations needed. By focusing on regions near the stability boundary and using gradient-guided sampling, the process avoids wasteful evaluation of clearly stable or unstable cases and concentrates resources on informative points. As a result, the overall computational burden is reduced compared to exhaustive or random sampling, while maintaining high quality in the training dataset.

2.3.2 Gradient Surgery

As established earlier, the Jacobians $\frac{\partial x(t)}{\partial \theta}$, evaluated at key time instances $t \in \{t_{ss}, t_{rocof}, t_{nadir}\}$, provide all the necessary information for determining the search direction in the parameter space θ.

Take RoCoF as an illustrative case. The critical time t_{rocof} can be identified as:

$$t_{rocof} = \arg\max_{t} |x_2(t)|. \tag{2.10}$$

If the condition $|x_2(t_{rocof})| > \tau_{rocof}$ is violated and the objective is to stabilise the sample, then θ is updated according to:

$$\theta^{+} = \theta + \alpha \cdot g_{rocof}(\theta), \tag{2.11}$$

where the gradient is defined as:

$$g_{rocof}(\theta) = -\frac{\partial |x_2(t_{rocof})|}{\partial \theta}, \tag{2.12}$$

and α is a predetermined step size.

Similarly, gradients for the steady-state frequency and frequency nadir are computed as:

$$g_{ss}(\theta) = \pm\frac{\partial |x_1(t_{ss})|}{\partial \theta}, \quad g_{nadir}(\theta) = \pm\frac{\partial |x_1(t_{nadir})|}{\partial \theta}. \tag{2.13}$$

The sign $\pm$ depends on the search direction: a negative sign is used when navigating from an unstable to a stable operating point, and a positive sign when moving in the opposite direction. For clarity, we assume in the following that all gradients g have been assigned with the correct sign.

However, during the update process, one may observe that the magnitudes of the three gradients differ significantly, and their directions may even oppose each other. A naive linear combination in such cases may only be effective for one stability criterion, while potentially degrading others.

To address this, we employ the *gradient surgery* technique from multi-task learning [64]. This approach systematically projects each gradient onto the normal plane of the others if their cosine similarity is negative, thereby eliminating destructive interference. The pseudocode for

this procedure is presented in Algorithm 1.

Algorithm 1: Gradient Surgery

Input : set of gradients $\mathcal{G} = \{g_{rocof}, g_{ss}, g_{nadir}\}$
Output : aggregated gradient $\hat{g}$
$\bar{g} = 0$
for $g \in \mathcal{G}$ **do**
  $g^p = g$
  for $g' \in \mathcal{G} \setminus g$ **do**
    `/* Project to normal space */`
    if $(g^p)^T \cdot g' < 0$ **then**
      $g^p := g^p - \frac{(g^p)^T \cdot g^p}{\|g'\|^2} g'$
    end
  end
  $\bar{g} = \bar{g} + g^p$
end

2.3.3 Computation and Discussion

In (2.8b), the Jacobians $\frac{\partial f}{\partial x}$ and $\frac{\partial f}{\partial \theta}$ can be computed either analytically or using automatic differentiation tools such as `autograd` or `PyTorch`. Since these Jacobians must be repeatedly updated during the integration of the ODE, a more efficient and stable strategy is to compute the *Jacobian-Vector Products* (JVPs) [65] for the two terms on the right-hand side of (2.8), following the FMAD approach discussed earlier. Consequently, evaluating (2.8) requires four evaluations of $f(\cdot)$ at the point (x, θ) to recover the ten augmented states, without the need to explicitly construct or store the full Jacobian matrices. Moreover, by leveraging the parallelism offered by modern AD libraries, we can sample a batch of θ values and solve (2.8b) in parallel for improved computational efficiency.

The pseudocode for the proposed sampling method is summarized in Algorithm 2.

Algorithm 2: Stationary Point Sampling Using FMAD

Input : initial dataset Θ_0, system parameters r, τ, M_0, D_0, ΔP, ODESolver, batch size b, maximum iteration m, sampling rule R, step size α

Output : augmented dataset Θ

$\Theta = \{\cdot\}$, $k = 1$

for $\{\theta^i\}^{i=1,\cdots b} \in \Theta_0$ **do**

  `/* Sample mini-batch */`

  while $k \leq m$ *and* R *is not satisfied* **do**

    $\{x^i(t)\}^{i=1,\cdots b}_{t\in[0,T]}, \{\frac{\partial x^i(t)}{\partial \theta^i}\}^{i=1,\cdots b}_{t\in[0,T]} \xleftarrow[\text{in parallel}]{\text{ODESolver}}$ (2.8) with initial condition (2.9) and parameters $\{\theta^i\}^{i=1,\cdots b}$

    Find the critical time steps: $\{t_{ss}\}^{i=1,\cdots b}$, $\{t_{rocof}\}^{i=1,\cdots b}$, $\{t_{nadir}\}^{i=1,\cdots b}$

    `/* Find the stability gradients */`

    $\{g^i_{ss}\}^{i=1,\cdots b}$, $\{g^i_{rocof}\}^{i=1,\cdots b}$, $\{g^i_{nador}\}^{i=1,\cdots b} \leftarrow \{\frac{\partial x^i_1(t_{ss})}{\partial \theta^i}\}^{i=1,\cdots b}$, $\{\frac{\partial x^i_2(t_{rocof})}{\partial \theta^i}\}^{i=1,\cdots b}$, $\{\frac{\partial x^i_1(t_{nadir})}{\partial \theta^i}\}^{i=1,\cdots b}$

    `/* Gradient surgery */`

    $\{\bar{g}^i\}^{i=1,\cdots,b} \xleftarrow{\text{Algorithm 1}} \{g^i_{ss}\}^{i=1,\cdots b}$, $\{g^i_{rocof}\}^{i=1,\cdots b}$, $\{g^i_{nador}\}^{i=1,\cdots b}$

    Update $\{\theta^i\}^{i=1,\cdots b} = \{\theta^i\}^{i=1,\cdots b} + \alpha \cdot \{\bar{g}^i\}^{i=1,\cdots,b}$

    $k = k + 1$

  end

  Add $\theta^i, i = 1, \cdots b$ to Θ

end

2.4 Case Study

In the case study, we examine the power system dynamics described by (2.5), with parameters provided in Table 2.1. All ordinary differential equations (ODEs) are solved using Euler's method. The experiments are conducted on a machine running Ubuntu 18.04, equipped with an Intel Xeon Gold 6230R CPU @ 2.10GHz.

Table 2.1: Power System Parameters

Parameter	Value	Parameter	Value
r	0.06 p.u.	f^{ss}_{max}	0.5 Hz
τ	10.0 s	f_{max}	0.8 Hz
M_0	6.0 s	$\dot{f}_{max}$	1.0 Hz/s
D_0	5.0 p.u.	ΔP	-0.12 p.u.

The initial dataset Θ_0, consisting of 100 samples, is randomly drawn from a normal distribution with mean 0 and standard deviation 50. The augmented dataset Θ can be generated in parallel for all 100 samples in Θ_0. We also observe that the steady-state deviation is independent of

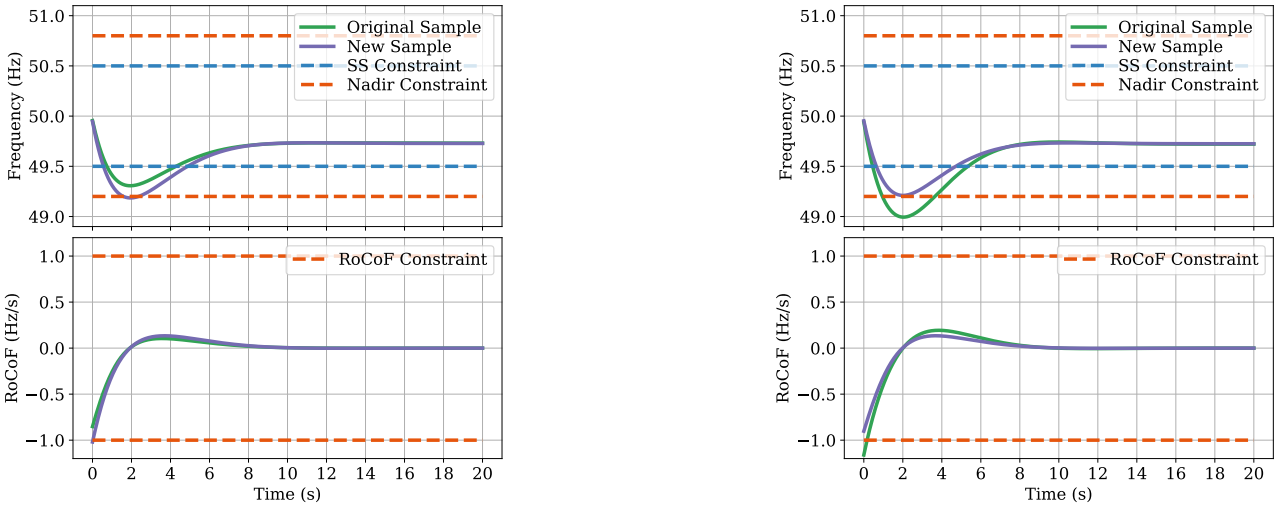

(a) (b)

Figure 2.1: Two examples of the proposed sampling method: (a). Search from 'stable' sample to 'unstable' sample; and (b). Search from 'unstable' sample to 'stable' sample.

the parameter K in the dynamic model (2.5). While this can be formally proven using the approach outlined in [60], the proof is omitted here due to space constraints. Consequently, the steady-state criterion is excluded from the subsequent analysis.

Two Examples

Fig. 2.1 illustrates two examples of transitions from an original sample (in green) in Θ_0 to a newly generated sample (in purple) in Θ. In the first example, the frequency response of the original sample satisfies all three stability criteria. The proposed algorithm successfully identifies an unstable counterpart and terminates precisely at the boundary of instability. In contrast, the second example starts with an original sample exhibiting instability in both nadir and RoCoF. The algorithm can shift it toward a stable counterpart.

Computational Performance

To evaluate the efficiency of the proposed FMAD approach, both computational time and memory usage are measured across several gradient-based methods. Two baseline methods are used for comparison: *unrolling differentiation* and *finite difference*, briefly reviewed in Appendix A.3. For a fair comparison, all methods are applied to the **same, randomly sampled** parameter set Θ_0 in a **batched** manner. Specifically, gradients are computed in parallel for a batch of 20 samples, with results averaged over five runs. Memory usage is monitored using the `psutil` Python package. Table 2.2 also presents the maximum absolute percentage errors of the FMAD and finite difference methods relative to the unrolling method.

The results indicate that, although the finite difference method requires four additional evaluations of $f(\cdot)$, it achieves the lowest memory usage and fastest runtime, owing to its avoidance of gradient computation and intermediate variable storage. However, its accuracy is highly sensitive to the choice of perturbation size ϵ, which can introduce truncation and round-off errors [65], making it unsuitable for practical use. In contrast, forward-mode AD (FMAD) achieves up to 25× memory savings over unrolling AD by eliminating the need to store intermediate states and gradients on the computational graph. Furthermore, FMAD delivers gradient accuracy on par with unrolling AD, up to machine precision. The main trade-off is a higher computational cost due to the additional evaluations of $f(\cdot)$.

In summary, while all methods achieve comparable gradient accuracy under ideal conditions,

the primary benefit of FMAD lies in its memory efficiency. Unlike reverse-mode AD with unrolling, which stores intermediate computational states over the entire time horizon, FMAD propagates derivatives forward without retaining past states, reducing memory usage by up to 25×. Although this comes at the cost of additional function evaluations, FMAD still outperforms finite difference methods in terms of gradient robustness and numerical stability, making it a practical choice for large-scale or long-horizon systems

2.5 Conclusion

This work presents an efficient gradient-based sampling method for constructing frequency stability datasets in power system operations. Gradients with respect to stationary parameters are computed by solving an augmented ODE via forward-mode automatic differentiation (FMAD). Compared to the unrolling method, FMAD significantly reduces memory usage, making it scalable to longer time horizons and larger systems. However, this comes at the cost of a notable increase in computational time—approximately 2× in the test case—highlighting a trade-off that must be considered in large-scale deployments.

Table 2.2: Performance comparison on different gradient-based sampling methods. The errors are the maximum absolute percentage errors with respect to the solution by Unrolling AD. The performances are recorded based on 5 runs.

Method	**Computation Performance**		**Max. Absolute Percentage Err.**				
	Memory (MB)	Time (s)	$\lvert\Delta x(t_{ss})\rvert$	$\lvert\Delta x(t_{nadir})\rvert$	$\lvert\Delta x(t_{rocof})\rvert$	$\lvert\Delta g_{nadir}\rvert$	$\lvert\Delta g_{rocof}\rvert$
Finite Difference ($\epsilon = 10^{-12}$)	7.41	0.22	$\leq 10^{-14}$			5.29	3.90
Finite Difference ($\epsilon = 10^{-14}$)	7.39	0.22	$\leq 10^{-14}$			10086.3977	5952.6488
Unrolling AD	1021.46	1.54	N/A				
Forward-Mode AD	38.76	3.52	$\leq 10^{-14}$				

Chapter 3

Adaptive Droop Gain Control for Optimal Kinetic Energy Extraction from Wind Turbines to Support System Frequency

Low-inertia power grids would benefit from frequency support from inverter-based generation, given the scarcity of synchronous generators as decarbonisation efforts progress. Wind turbines store kinetic energy in their rotors as they produce electric power, which can be partially released to the grid in the event of a generation loss, in order to contain the frequency drop.

This thesis introduces a novel fast droop control for WTs based on an adaptive droop gain strategy, extracting the optimal amount of kinetic energy depending on the overall system conditions. This requires mapping the low-level inverter controls into a system-wide economic optimisation, which has not been successfully addressed yet. To overcome this challenge, we propose a data-driven methodology for integrating frequency stability constraints into an OPF formulation, which is explicitly dependent on the low-level control parameters of the wind turbines' converters. A modified OCT is used to encode frequency-security guarantees for the grid, due to its suitable structure for being included in optimisation while maintaining tractability. Through relevant case studies, we demonstrate the effectiveness of the proposed system-aware control for WTs, achieving over 8% system cost savings compared to a system-unaware controller.

3.1 Introduction

Several ameliorative strategies have been put forward to avoid an over-deceleration of WTs during the frequency-supporting process. In [16], the WT's post-fault power output trajectory has been devised with significant attention on the chosen rotor speed at the beginning of rotor speed restoration of WTs. Reference [17] has proposed a scheme by navigating the electrical power output of WTs as a specified Gaussian distribution trajectory controlled by the computed standard deviation values, which guarantees the declining rotor speed strictly larger than the

minimum permissible rotor speed. The authors in [13, 18] employed an ADG in the control loop, which is temporally proportional to the KE stored in WTs to improve the FN without the possibility of an over-deceleration. Notably, ADG serves as a function of the WTs' real-time rotor speed and/or RoCoF of the system to maximise the frequency-supporting capability.

3.1.1 Optimal FFS from a System Perspective

The aforementioned approaches focused on the improvement of frequency dynamics on a device level, instead of the aggregate performance of WTs within a wind farm (WF). FFS from WTs should be optimised on a system level, considering the combined response of a number of WTs, since the optimal performance for a single WT does not necessarily correspond to the best solution for the entire power system [66]. Therefore, it is necessary to determine, on a system level, the optimal frequency support from WFs while considering the actual dynamic conditions for individual WTs.

A few papers have addressed the issue of how to optimise FFS from WTs from a system perspective. The authors in [67,68] utilised the gain scheduling approach, namely a population of parameter settings in dynamic simulations with a variety of system conditions. Reference [67] argues that the synthetic inertia (SI) control can be viably reduced to a fast droop control (FDC), where the droop gain is tuned depending on the specific configuration of the power system. In [68], the authors have explored the best performance of FFS from WTs from a

Table 3.1
Summary of control schemes for FFS from WTs

Ref.	Preventing WT's over-deceleration	Lessening/Eliminating SFDs	Optimised on system level	Benefiting system operational
[9]	✓ [1]	✓	✗ [2]	✗
[10]	✓	✓	✗	✗
[12]	✗	✓	✓	✗
[13]	✓	✗	✗	✗
[15]	✓	✓	✗	✗
[16]	✓	✓	✗	✗
[17]	✓	✗	✗	✗
[18]	✓	✗	✗	✗
[67]	✗	✗	✓	✗
[68]	✗	✓	✓	✓
[69]	✗	✓	✓	✓

[1] '✓' indicates the inclusion of the technique in the paper.
[2] '✗' indicates the non-inclusion.

system perspective, which is jointly evaluated by the improvement of the FN, the recovery time of frequency response and the presence of an SFD.

However, few previous works have placed this problem within a framework of system scheduling. While the work in [69] demonstrated the significant economic benefits of FFS from WFs, highlighting the added economic value of dynamically optimising this FFS service, the detailed dynamics of WTs were not incorporated into the unit commitment model. This issue was addressed in [12], where the SI provision from WTs was optimised in a unit commitment model, by using analytical system-frequency constraints considering the detailed dynamics of WTs. Table 3.1 has synthesized the preceding papers from the technical perspectives: preventing WT's over-deceleration, lessening/eliminating SFDs, optimised on the system level and benefiting the system operational cost. However, our proposed method has accounted for all these techniques, which will be demonstrated in the following sections.

3.1.2 Modelling Approaches for System Frequency Security

In order to optimise the volumes of different frequency-supporting services in an economic setting, security rules are needed that describe the safe region for frequency stability. These rules can then be included as constraints in an economic optimisation model. The state-of-the-art approaches to formulating frequency constraints within system scheduling models can be classified into two groups, i.e. analytical approaches using the swing equation and data-driven

approaches based on a time-domain model.

Analytical approaches either model the distinct frequency support services as a set of ramp functions with different slopes and time delays [53, 70], or obtain an analytical expression of frequency deviation based on a multi-machine system frequency response model [71] or an equivalent aggregate system frequency response model [54]. Nevertheless, analytical approaches sacrifice some detail in modelling system frequency dynamics, as it is necessary to forego some accuracy in modelling the primary frequency response to derive closed-form expressions for frequency limits. In all these works, the frequency nadir constraint is nonlinear, with squared terms [53] or square roots [71]. Extensive linearisation techniques have been used to integrate the frequency nadir constraint into a conventional unit commitment problem formulated as Mixed-Integer Linear Programming (MILP) [72–75]. It should be noted that modelling the frequency response of WTs and synchronous generators (SGs) with standard high-order IEEE models renders deducing linear frequency-security constraints well nigh impossible.

In order to accurately describe the dynamics of FFS from WTs alongside SGs, detailed dynamic models of these assets are expected to be introduced in a system scheduling framework, which is the main incentive behind data-driven approaches for deducing power system security rules. In essence, intelligent data-driven approaches deliver such models with fast and accurate online predicting capabilities, which describe the mapping relationship between the power system operating conditions (input) and the corresponding security status (output) [76]. It should be

recognised that the underlying properties of power systems are directly reflected in the data-driven models, which only focus on system security attributes and the most relevant features, which obviates the need for complicated model-based analysis without losing any information on dynamics.

Several classifiers have been adopted to represent system security rules for preventive and corrective control, for instance, decision trees (DTs) [48, 77, 78], artificial neural networks (ANNs) [79–81], deep learning [82, 83], Support Vector Machine (SVM) [84, 85] and logistic regression [86]. ANNs with their rapid computational speed and robust generalisation capabilities have found applications in diverse power system challenges, particularly where model-based approaches fall short in delivering the desired levels of accuracy and efficiency. In SVM, the linear technique involves finding a hyperplane that best separates the classes in the input space, which leverages the principle of structural risk minimization, reducing the need for extensive training samples. Deep learning has surpassed traditional machine learning methods and integrated seamlessly into research and industry, demonstrating the ability to autonomously extract valuable features for various tasks. These approaches have been proven effective for data-centric security evaluations of large power systems.

Given the nonlinear and nonconvex frequency security boundary in a high-dimensional space, SVM and logistic regression are limited by a hyperplane that simply divides the space into two regions, leading to poor accuracy. In addition, interpretability is of great importance for

power system operators, as trust in these classifiers is based on the level of understanding of their predicting processes [76]. Tree models with desired interpretability are advantageous over other methods that perform better in predicting, but are less interpretable. Compared with conventional DT models, OCTs maintain a simple tree structure with lower depth without losing prediction accuracy [48]. Thus, OCT helps to achieve a balance between predictive accuracy and interpretability. Besides, as opposed to neural networks, OCT with a concise structure ensures tractability of the economic optimisation by introducing significantly fewer binary variables, which is highly desirable for online system-wide economic models. An OCT model has been deployed in [87] for the extraction of linear frequency constraints, in which a detailed dynamic model is used for data generation.

In addition to model-specific interpretable methods, a growing body of research has explored model-agnostic post-hoc explainability tools such as SHAP [88] and LIME [89]. These methods are capable of explaining predictions from black-box models by attributing feature importance using local surrogate models (LIME) or Shapley values from cooperative game theory (SHAP). Their use has been demonstrated in power system security assessment, fault detection, and renewable forecasting tasks [90], [91]. However, in this work, I opt for inherently interpretable models—specifically Optimal Classification Trees (OCTs)—which provide global transparency and rule-based decision logic that are directly understandable by human operators. This choice prioritises operational interpretability over model complexity.

3.1.3 Present Work

Given this context, this paper intends to bridge the gap between the device-level converter control and the system-level optimal economic scheduling. An ADG control is proposed to fully utilise the frequency-supporting capability of WFs, while the ADG parameter is introduced as a decision variable in the data-driven frequency-security constraints, and optimised within a system scheduling framework. The main contributions of this paper are threefold:

a. A novel adaptive droop control for wind turbines to support frequency drops is proposed, where the optimal amount of kinetic energy can be extracted from the power system perspective. The ADG is formulated as a function of the electricity grid's operating condition, such as the overall level of reserve, while fully accounting for the dynamics of individual wind turbines.

b. The proposed ADG control framework is further incorporated into the system-level economic optimisation model through a data-driven method, using a tractable and transparent 'fully-secure' OCT formulation. The control parameters of wind turbines are allowed to be explicitly considered as decision variables, while guaranteeing that frequency stability is maintained in every instance.

c. Relevant case studies on an IEEE benchmark network demonstrate that our proposed system-aware control strategy leads to system savings of more than 8%, compared to a

system-unaware controller.

In this context, a 'fully secure' classification refers to the classifier's ability to reliably distinguish stable from unstable operating points within the current power system operating window. This definition is constrained by the temporal and operational scope of the training data, and does not imply universal security across all future scenarios. Rather, it reflects the classifier's capacity to ensure security compliance under the defined range of short-term operating conditions. The rest of this paper is organised as follows. Section 3.2 presents the model of variable speed WT considered and the proposed adaptive droop control. The Secure OCT and the OPF formulations are stated in Section 3.3. The results of several case studies implemented in both dynamic simulation and system scheduling frameworks, together with the corresponding analysis and discussion, are included in Section 3.4. Finally, Section 3.5 gives the conclusion.

3.2 Adaptive Fast Droop Control Strategy

Variable speed WTs are the focus of the ADG control proposed in this paper. This section offers an overview of the variable speed WT model used and the proposed FDC strategy, which applies to both doubly fed induction generator (DFIG)-based and permanent magnet synchronous generator (PMSG)-based WT systems.

3.2.1 Model for Variable Speed WT System

Able to operate under a wide range of wind speeds, variable speed WTs are capable of achieving maximum energy conversion efficiency by regulating the rotor speeds dynamically to maintain an optimal tip speed ratio λ, i.e. the ratio of the blade tip speed to the wind speed. The energy conversion efficiency, from available wind power to captured mechanical power, can be expressed as a power coefficient C_p, which is a function of both pitch angle β and tip speed ratio λ. Hence, the mechanical power captured by WTs is described as follows [92]:

$$P_m = \frac{1}{2}\,\rho\,\pi\,R^2\,v_w^3\,C_p(\lambda,\beta) \tag{3.1}$$

with air density ρ, turbine radius R and wind speed v_w. Without loss of generality, we use here the coefficients for $C_p(\lambda,\beta)$ described in [92]:

$$C_p(\lambda,\beta) = 0.5176\left(\frac{116}{\lambda_i} - 0.4\beta - 5\right)e^{-\frac{21}{\lambda_i}} + 0.0068\lambda \tag{3.2}$$

with

$$\frac{1}{\lambda_i} = \frac{1}{\lambda + 0.08\beta} - \frac{0.035}{\beta^3 + 1} \tag{3.3}$$

$$\lambda = \frac{w_r R}{v_w} \tag{3.4}$$

where w_r denotes the rotor speed of WTs.

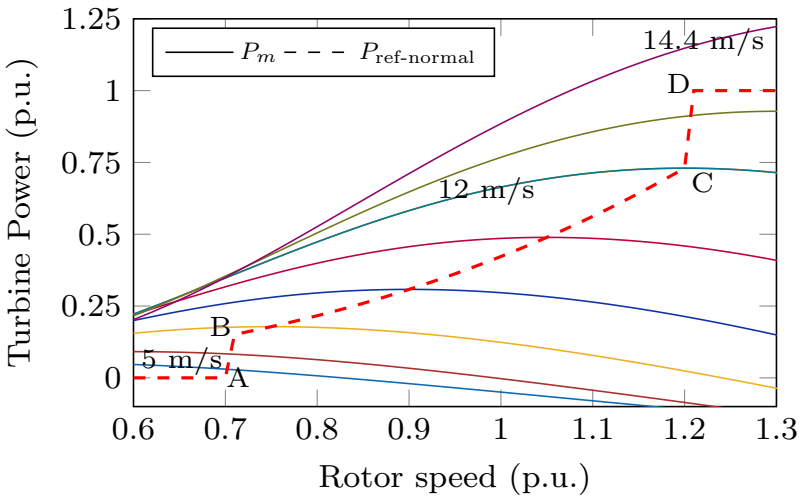

Figure 3.1: Turbine power characteristics (pitch angle $\beta = 0°$).

For the typical control schemes of DFIG-based and PMSG-based WT systems, the active power output of WTs is dictated by the pre-defined power-speed tracking characteristic, namely the active power reference in normal operation $P_{\text{ref-normal}}$ for the rotor-side converter [93]. Such characteristic curve is illustrated in Fig. 3.1 by the A-B-C-D superimposed curve, and $P_{\text{ref-normal}}$ can be expressed in per unit (p.u.) as follows:

$$P_{\text{ref-normal}} = \begin{cases} 0 & 0 \le w_r < w_A \\ \frac{P_B - P_A}{w_B - w_A}(w_r - w_B) + P_B & w_A \le w_r < w_B \\ k_{\text{opt}} \cdot (w_r / w_b)^3 & w_B \le w_r < w_C \\ \frac{P_D - P_C}{w_D - w_C}(w_r - w_D) + P_D & w_C \le w_r < w_D \\ P_{\text{max}} & w_D \le w_r \end{cases} \tag{3.5}$$

where $P_{\text{ref-normal}}$ is in p.u. of nominal mechanical power while w_r is in p.u. of generator syn-

chronous speed, with w_{base} as the base rotational speed.

It should be noted that, under MPPT operation (i.e. B-C curve in Fig. 3.1), $C_{p\text{-max}}$ can be achieved by maintaining $\lambda = \lambda_{\text{opt}}$ and $\beta = 0°$, i.e. $C_{p\text{-max}} = C_p(\lambda_{\text{opt}}, 0)$. Therefore, differentiating (3.2) with respect to λ, in order to obtain the value of $C_{p\text{-max}} = 0.48$, the value of $\lambda_{\text{opt}} = 8.1$ is calculated as the maximum. Furthermore, P_C is the maximal power at the base wind speed with $\beta = 0°$. In the pitch angle control system, depicted in Fig. 3.2, the pitch angle β remains zero degrees until the WTs' rotor speed w_r reaches point D, otherwise it is proportional to the speed deviation from point D.

The specific numerical parameters of the WT model used in this paper are shown in Table 3.2 [92].

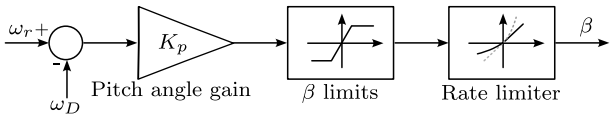

Figure 3.2: Pitch angle control system.

Table 3.2
Parameters of Variable Speed Wind Turbine

Nominal turbine mechanical output power (MW)	1.5
Tracking characteristic speeds [ABCD (p.u.)]	[0.7 0.71 1.2 1.21]
Wind speed at point C (m/s), base rotor speed w_b (p.u.)	12, 1.2
Optimal power gain [k_{opt}]	0.73
Tracking characteristic powers [ABCD (p.u.)]	[0 0.15 0.73 1.0]
Pitch angle controller gain [K_p]	500
Max. pitch angle (deg)	45
Max. rate of change of pitch angle (deg/s)	2

3.2.2 Proposed Adaptive Fast Droop Control

The conventional overproduction control for WTs replicates the natural inertial and governor response of SGs via two control loops, i.e. the RoCoF and droop loops. However, differentiating the noise components blended with the measured frequency signal induces large variations of power signal in the RoCoF loop, which accounts for intense torque pulsations in the drive-train of WTs [67]. The pure-droop control (i.e. droop loop only, with no RoCoF loop) accordingly becomes a viable alternative for overproduction control based on the case studies implemented in [67], where the optimal droop gain should notably be tuned dependently on the specific power system characteristics.

Nonetheless, the work in [67] did not consider the issue of WTs' potential over-deceleration during FFS provision. To address this issue, [94] proposes an ADG that is proportional to the real-time kinetic energy stored in the rotor of WTs: At the beginning of frequency falls, a WT with a larger rotor speed thus a larger stored KE is initially set with a larger ADG, while ADG decreases with a declining rotor speed in the subsequent process of KE extraction. A WT stops releasing their KE when the rotor speed w_r declines to the minimum permissible rotor speed $w_{r,\min}$ because ADG is zero. Otherwise, it can lead to over-deceleration in WT generators with limited KE for a large but fixed droop gain. Additionally, if wind speed drops during inertial

control, a low gain may even cause over-deceleration. The function of the ADG is given as:

$$\mathrm{ADG}(w_r) = K \cdot (w_r^2 - w_{r,\min}^2) \tag{3.6}$$

with a fixed constant K. The authors in [13] underscore that design purposes determine the value of K, i.e. this value depends on the power system under consideration. In [93], K has been devised as a function of the wind penetration level 'pl', that is:

$$\mathrm{ADG}(pl, w_r) = K(pl) \cdot (w_r^2 - w_{r,\min}^2) \tag{3.7}$$

Here K serves as a function of pl to account for the impact of wind penetration level on the aggregated FFS from WFs and hence the post-event frequency evolution. However, a large value of K possibly gives rise to an SFD at large wind speeds, which will be demonstrated in Section 3.4.1. Moreover, optimal scheduling of the frequency ancillary service of WFs entails information on the system's overall reserve determined by dispatches of other generation sources, which is not considered in (3.7).

Accordingly, we put forward the idea that the ADG may simultaneously consider the stable operation of individual WTs and 'optimal scheduling' for FFS from WFs. Furthermore, the 'optimal scheduling' relies on the 'optimal ADG' that renders the system post-fault frequency response respecting the security limits at the minimal operation cost of the power system,

which will be illustrated in Section 3.4.1. Consequently, our proposed ADG is formulated as an explicit function of WTs' real-time dynamic conditions (i.e. the real-time rotor speed w_r which can be readily measured by encoders in generators) and an implicit function of system-wide operating conditions, i.e. (3.9), that includes the wind speed v_w, the SGs' dispatches $\boldsymbol{P_G}$, the load levels L_D, the wind penetration level pl and the magnitude of the largest potential power loss ΔP_L. Note that the bold script for $\boldsymbol{P_G}$ means that it is a vector containing the pre-fault dispatches of all the SGs in the system. The proposed function for the ADG can be formulated as:

$$\mathrm{ADG}(v_w, \boldsymbol{P_G}, L_D, pl, \Delta P_L, w_r) = \widetilde{K}_{\mathrm{sys}} \cdot \underbrace{(w_r^2 - w_{r,\min}^2)}_{\text{deter over-deceleration}} \tag{3.8}$$

with

$$\widetilde{K}_{\mathrm{sys}} = f(v_w, \boldsymbol{P_G}, L_D, pl, \Delta P_L) \tag{3.9}$$

The 'optimal ADG' resorts to 'optimal $\widetilde{K}_{sys}$' in (3.8) for achieving the 'optimal scheduling' of FFS from WFs. The mapping relationship between the 'optimal K_{sys}' and the system-wide conditions can be implicitly determined by solving system economic optimisation integrated with frequency stability constraints where $\widetilde{K}_{sys}$ serves as a decision variable. Note that the previously proposed analytical methods for frequency security listed in Section 3.1 cannot provide closed-form constraints when $\widetilde{K}_{\mathrm{sys}}$ is modelled as a decision variable, especially considering all the arguments in the ADG included in (3.9). Therefore, the enhanced ADG control proposed

here necessitates a data-driven method for being incorporated into a system-wide economic optimisation, which is another critical novelty of this work. The economic optimisation minimises the system's operational cost given the equality and inequality constraints:

$$\min \quad \boldsymbol{c}_{\boldsymbol{m}}^{T} \boldsymbol{P}_{\boldsymbol{G}} \tag{3.10a}$$

$$\text{s.t.} \quad g(\boldsymbol{x}) = 0 \tag{3.10b}$$

$$h(\boldsymbol{x}, \widetilde{K}_{\text{sys}}) \leq 0 \tag{3.10c}$$

with the marginal cost of generating units $\boldsymbol{c_m}$ and $\boldsymbol{x}$ serves as a vector of steady-state decision variables of power systems, including active/reactive powers of generators and nodal voltage magnitudes/phase angles. (3.10b) are power balance equations in all nodes, while (3.10c) involve post-fault frequency stability constraints and a set of operational constraints considering branch flow limitations, generator capacities and nodal voltage limits. Note that $\widetilde{K}_{\text{sys}}$ would only appear in the inequality constraints which are in the form of (3.13). Hence, the 'optimal $\widetilde{K}_{\text{sys}}$' can be expressed as:

$$\widetilde{K}_{\text{sys}}^{opt} = \underset{\widetilde{K}_{\text{sys}} \in D}{\arg\min} \ \boldsymbol{c}_{\boldsymbol{m}}^{T} \boldsymbol{P}_{\boldsymbol{G}} \tag{3.11}$$

where D is the feasible region defined by (3.10b) and (3.10c). The proposed strategy of adaptive FDC is presented in Fig. 3.3. It is achievable to attain the 'optimal ADG' in local WF systems through hourly updating by the system operator based on communication networks: the system

operator needs to provide the local droop controller in WFs with hourly system-wide information, such as the wind penetration level and the predicted wind power and load. The real-time information, i.e. rotor speed measured from WTs' side and local frequency excursion measured by a phase-locked loop (PLL) connected to the grid, are delivered to the local controller as well. Note that P_w is the available wind power, as defined by the wind speed v_w in (3.5).

The proposed FDC strategy is remarkably applicable to both DFIG-based and PMSG-based WT systems with their rotor-side converters (RSCs) in power control: Under their grid-side converters (GSCs) oriented to the grid, the power command for RSCs, i.e. P_{ref} in Fig. 3.3, comes from the WT control centre to realize MPPT in normal cases or FFS in frequency contingencies. More precisely, the RSCs in back-to-back converters of both systems attempt to deliver their desirable active powers to grids by regulating the rotor speeds. However, the power flow in the rotor circuit for DFIG is bidirectional depending on the rotor speed compared with the synchronous speed of the grid, while PMSG constantly works in synchronous mode with unidirectional power flow in converters.

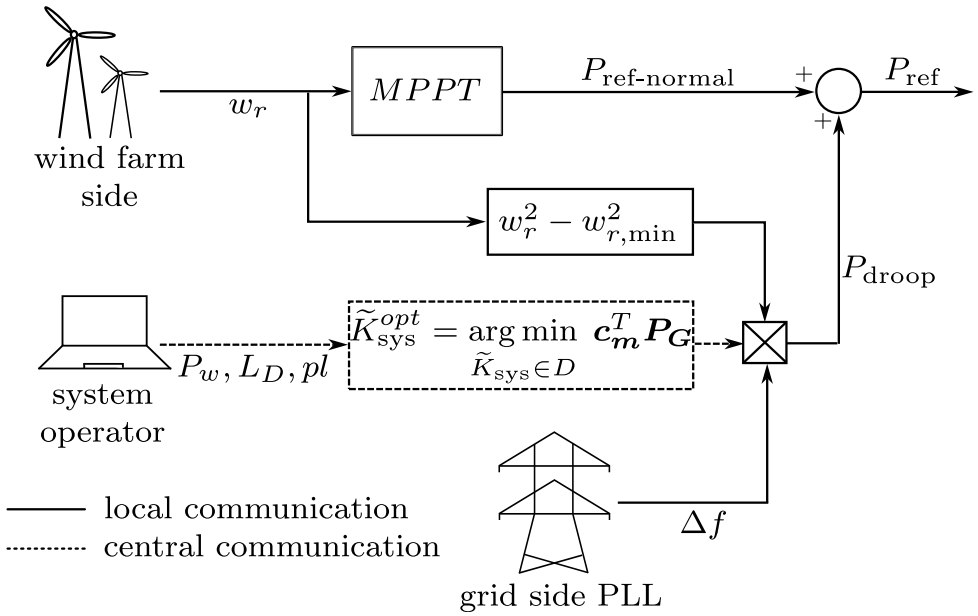

Figure 3.3: Control scheme for the proposed adaptive droop gain.

3.3 Frequency-secured System Operation via Data-driven Constraints

Here we present the proposed frequency-secured economic dispatch methodology. The problem is formulated as an OPF with frequency-limits constraints, where we introduce an improved OCT approach for power system frequency security, incorporating the optimal ADG control presented before.

3.3.1 Multivariate Optimal Classification Tree with Frequency-Security Guarantees

A multivariate optimal classification tree encoding the frequency-security guarantees (referred to as 'Secure OCT(M)') is formulated in this section as a mixed-integer optimisation problem. This is an enhanced formulation proposed in this paper, based on the OCT(M) approach introduced in [48], to remove the 'false safe' predictions. This is achieved by modifying the cost function in the OCT(M) model.

Given that the electricity grid is a safety-critical system, and that uncontrolled frequency decline could potentially lead to system collapse, this modified OCT(M) removes any 'false safe' predictions, as these correspond to 'unsafe' scenarios predicted as 'safe' operating points. In turn, removing 'false safe' predictions implies increasing the conservativeness of the tree, as will be discussed later. The proposed loss function in the Secure OCT(M) and associated constraints are formulated as follows. The remaining OCT(M) constraints are not included for conciseness, the interested reader can refer to [48].

$$\min \quad \frac{1}{\hat{\mathcal{L}}} \sum_{t \in \underline{\Omega}^{\mathcal{T}}} l_t + \alpha \sum_{m \in \underline{\Omega}^{B}} d_m \tag{3.12a}$$

$$\text{s.t.} \quad l_t \geq \omega \cdot n_{0t} - \mathcal{M} \cdot (1 - c_t) \qquad \forall t \in \underline{\Omega}^{\mathcal{T}} \tag{3.12b}$$

$$l_t \leq \omega \cdot n_{0t} + \mathcal{M} \cdot c_t \qquad \forall t \in \underline{\Omega}^{\mathcal{T}} \tag{3.12c}$$

$$l_t \geq n_{1t} - \mathcal{M} \cdot c_t \qquad \forall t \in \underline{\Omega}^{\mathcal{T}} \tag{3.12d}$$

$$l_t \leq n_{1t} + \mathcal{M} \cdot (1 - c_t) \qquad \forall t \in \underline{\Omega}^{\mathcal{T}} \tag{3.12e}$$

$$n_{1t} = \sum_{i \in \Omega^{\mathcal{N}}} z_{it} \cdot Y_i \qquad \forall t \in \underline{\Omega}^{\mathcal{T}} \tag{3.12f}$$

$$n_{0t} = \sum_{i \in \Omega^{\mathcal{N}}} z_{it} - n_{1t} \qquad \forall t \in \underline{\Omega}^{\mathcal{T}} \tag{3.12g}$$

The objective function (3.12a) aims to minimise the misclassification cost and maintain a simple tree structure as far as possible. More precisely, the first item in (3.12a) accounts for the total classification error in all candidate leaf nodes, and the second term penalises the number of branch nodes in the global tree. Parameter $\hat{\mathcal{L}}$ is a baseline value of misclassification error for the entire, i.e. the sample number of the minor class, while α is a complexity parameter for regulating the split number of a tree model and the detailed tuning procedures have been presented in [95].

The binary variable z_{it} is introduced to track if data point i is assigned to leaf node t. The number of observations labelled with class 1 in each leaf node, denoted as n_{1t}, is calculated in (3.12f) with the parameter $Y_i = 1$ for 'safe' observations. Accordingly, $Y_i = 0$ accounts for 'unsafe' data points, used to calculate the number of observations with class 0 for each leaf node in (3.12g). Decision variable c_t is used to track the prediction of each terminal node: $c_t = 1$ denotes that leaf node t predicts unseen observations as secure cases (corresponding to class 1), while $c_t = 0$ corresponds to the insecure class. The big-M constraints (3.12d) and (3.12e)

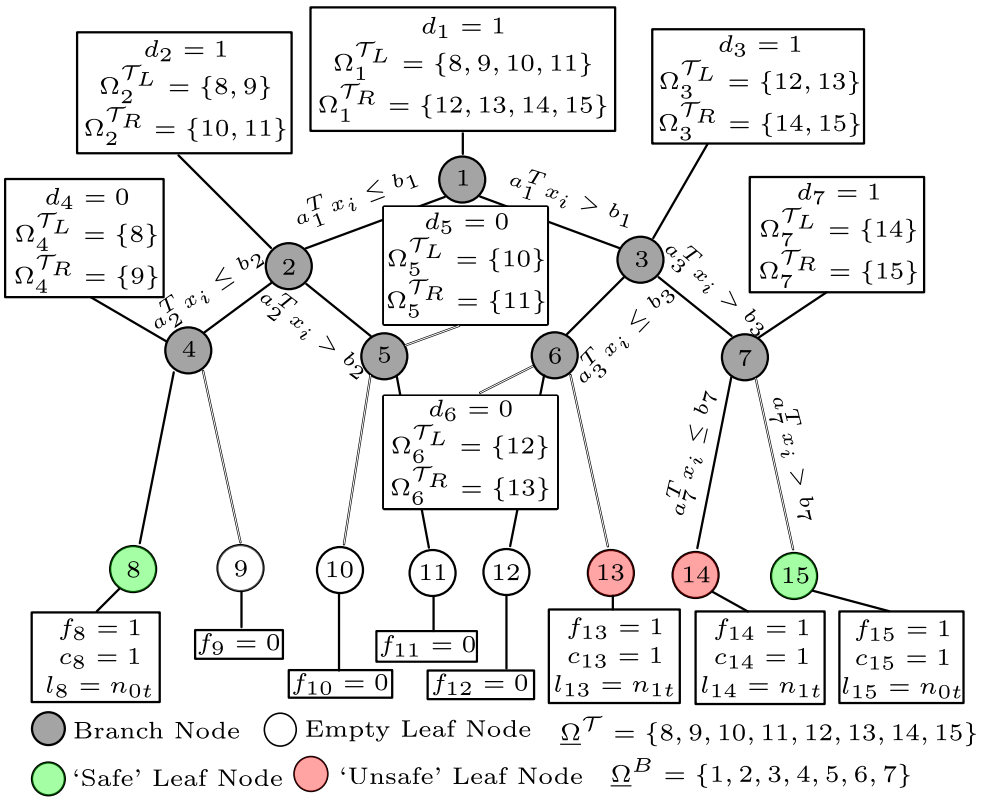

Figure 3.4: Demonstration model of multivariate OCT.

enforce the misclassification cost $l_t = n_{1t}$ if terminal node t corresponds to class 0. Constraints (3.12b) and (3.12c) enforce $l_t = n_{0t}$ if $\omega = 1$ with leaf node t assigned to 'safe' class ($c_t = 1$), while values of $\omega > 1$ allow increasing the weight of unsafe operating points; these constraints are instrumental to predicting 'unsafe' points, i.e. eliminating 'false safe' predictions.

We define the optimal ω as ω^*: The full precision of the trained model with ω^* can be evaluated on the validation set with the maximal accuracy achieved. A complete tuning process for identifying ω^* that would eliminate 'false safe' predictions follows:

a. Tune all the hyper-parameters in Secure OCT with $\omega = 1$ based on the validation set.

b. Use the grid-search technique, i.e. parameter sweep through a manually specified subset,

to find ω_0 from the CART model with the same hyper-parameters in Step 1 so that the maximal accuracy can be obtained without losing any precision.

c. Inject the CART solution and ω_0 as a warm start to the Secure OCT model for training.

d. Test the precision on the validation set based on the trained OCT model: if the precision is not 100%, increase ω from ω_0 to obtain ω^*. Otherwise, decrease ω to ω^* until the precision starts to decrease.

To exhibit the mathematical structure for encoding frequency-security guarantees, an OCT(M) is shown in Fig. 3.4 to give further insight into the integer programming. The splitting characteristic of branch nodes are dictated by the binary variable d_m: branch nodes 1, 3, 7 are built with their $d_m = 1$ while no splits are performed in nodes 2, 4, 5, 6 ($d_m = 0$). Furthermore, the OCT formulation restricts a branch node from applying a split if its parent node does not perform a split. For example, in Fig. 3.4, no splits are in node 4, 5 as no split is applied in node 2. Hence, leaf node 8 contains the same set of observations as branch node 2 given no splitting in nodes 2 and 4, i.e. $d_2 = 0$ and $d_4 = 0$. The same situation is applied to branch node 6 and leaf node 13. Therefore, no observations are located in branch node 5 and leaf nodes 9, 10, 11 and 12, leading to $f_t = 0$ for $t \in \{9, 10, 11, 12\}$. The concise structure of the OCT model has been reduced based on Fig. 3.4 by pruning the redundant nodes and branches and shown in Fig. 3.5 to help readers understand better.

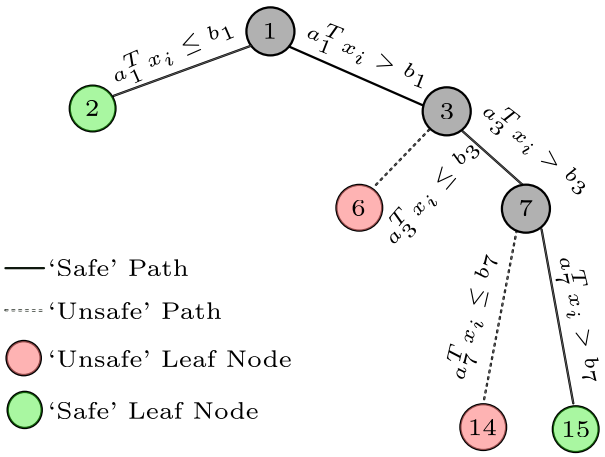

Figure 3.5: Concise equivalent model for multivariate OCT demonstration.

Branch node m splits the training set by $a_m^T x_i \leq b_m$ and $a_m^T x_i > b_m$, and they are followed by leaf node $t \in \Omega_m^{\mathcal{T}_L}$ terminating in the left branch of m and leaf node $t \in \Omega_m^{\mathcal{T}_R}$ terminating in the right branch of m respectively. The binary variable f_t indicates whether leaf node t is empty ($f_t = 0$) or not ($f_t = 1$). Given the limited numerical precision in MIP solvers, non-strict constraints $b_m + \epsilon - a_m^T x_i \leq 0$ are changed from inequality ones $a_m^T x_i > b_m$ in the course of integer programming. We need to introduce a binary variable p_m to track the 'safe' path in the tree which threads the critical branch nodes $m \in \underline{\Omega}^B$. The critical branch nodes in Fig. 3.4 are $m = \{1,\ 3,\ 7\}$. We specify that $p_m = 0$ implies $a_m^T x_i \leq b_m$ while $p_m = 1$ forces $b_m + \epsilon - a_m^T x_i \leq 0$ to be activated using big-M strategy. Hence, the mathematical structure for encoding frequency-security guarantees is presented here:

$$a_1^T x_i - b_1 \leq \mathcal{M} \cdot p_1 \tag{3.13a}$$

$$(b_1 + \epsilon) - a_1^T x_i \leq \mathcal{M} \cdot (1 - p_1) \tag{3.13b}$$

$$(b_3 + \epsilon) - a_3^T x_i \leq \mathcal{M} \cdot (1 - p_3) \tag{3.13c}$$

$$p_1 \leq p_3 \leq p_1 \tag{3.13d}$$

$$(b_7 + \epsilon) - a_7^T x_i \leq \mathcal{M} \cdot (1 - p_7) \tag{3.13e}$$

$$p_3 \leq p_7 \leq p_3 \tag{3.13f}$$

3.3.2 Second-Order Cone OPF with Mixed-Integer Linear Frequency-Security Constraints

Given that the alternating-current OPF problem is nonconvex, several approximations and relaxations have been proposed, such as direct-current (DC)-OPF, Second-Order Cone Programming (SOCP)-OPF and Semidefinite Programming (SDP)-OPF. SOCP-OPF exhibits several merits: on the one hand, it is more general than the linear DC-OPF approximation, allowing to model reactive power within the network; on the other, it is less sensitive to the network scale than the more general SDP-OPF, requiring fewer computational resources [96]. To test our proposed methodology for optimal kinetic energy extraction from WTs from a system-wide perspective, we use here a standard SOCP-OPF formulation such as the one described in [97]. Note however that the ADG strategy for fast frequency support and associated Secure OCT(M) are applicable to other OPF formulations.

The purpose of SOCP-OPF is to minimise the total generation cost subject to a set of steady-state constraints, such as active and reactive power balance, generation limits, voltage mag-

nitude limits and transmission line limits. We also include the frequency-security constraints accounting for maximum admissible frequency deviation ($\Delta f_{\max} \leq 0.8$ Hz, as per GB standards), maximum admissible RoCoF, $(df/dt)_{\max} \leq 1$ Hz/s, and maximum admissible frequency deviation at quasi-steady-state (q-s-s) ($\Delta f^{\text{ss}}_{\max} \leq 0.5$ Hz) [98].

The frequency-security constraints defined by the Secure OCT(M) model have been encoded within the SCOP-OPF in the pattern demonstrated in (3.13). The data used for training the Secure OCT(M) model is generated from the detailed dynamic system model implemented in MATLAB/Simulink. In essence, the set of MILP constraints provides an accurate approximation to the highly nonlinear, nonconvex boundary distinguishing the 'safe' and 'unsafe' frequency scenarios in the high-dimensional space, wherein the number of dimensions is in line with the number of data features (i.e., P_w, $\boldsymbol{P_G}$, L_D, pl, ΔP_L, $\widetilde{K}_{\text{sys}}$). The accuracy of the Secure OCT(M) as a frequency-security classifier is analysed in the following section.

3.4 Case Studies

Several case studies on a modified IEEE 14-bus system as shown in Fig. 3.6, implemented with the values from [99], are conducted to demonstrate the benefits of the proposed ADG control strategy, where the ADG value is optimised from a system-benefits perspective. Two models are used in this section: 1) a detailed dynamic model used to generate a data set of safe and

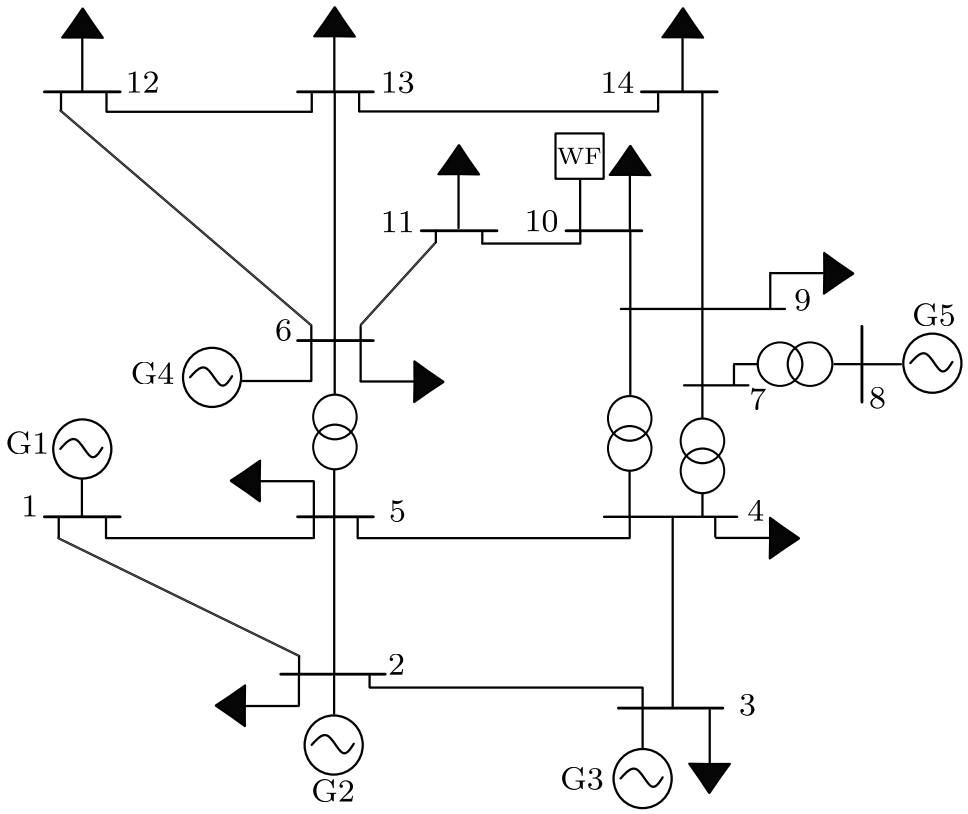

Figure 3.6: IEEE 14-bus test system.

unsafe operating points regarding frequency stability, which is then used as a training set for the Secure OCT(M); and 2) a frequency-secured MISOCP-OPF model to provide the optimal system dispatch. The full dynamic model is finally used again to validate the dispatch solutions, testing if the potential frequency excursions following the largest contingency would respect the pre-defined frequency limits.

The conventional IEEE type governors like DEGOV1 for diesel generators, IEEEG1 for gas and steam generators, together with AVRs (Automatic Voltage Regulators) such as SEXS for steam units, and GAS and EXST1 for diesel units, describe the dynamic characteristics of the thermal power units [100]. DFIG-based WT system has been employed with optimal torque control for the RSC and the GSC maintaining dc-link voltage and providing reactive power to the grid.

Table 3.3
Thermal generation mix within test case

	G1	**G2**	**G3**	**G4**	**G5**
Number of Units	2	2	1	1	1
Rated Power (MW)	112.5	70	100	95	105
Min Stable Generation (MW)	5	17.5	20	15	25
Governor Droop Gain (%)	N/A	N/A	0.08	0.06	0.05
Max governor response (MW)	N/A	N/A	65	35	70
Rated Reactive Power (Mvar)	10	50	40	24	24
Min Reactive Power (Mvar)	0	-40	0	-6	-6
Cost coefficient c_1 (£/MWh)	50	40	20	30	10
Cost coef. c_2 (£/(MW)^{2}h)	0.5	0.4	0.2	0.3	0.1

In our model, the PLL has served as a grid-synchronisation technique to account for its effects on system frequency response, such as the increasing oscillations and settling time [101]. The characteristics of the thermal units in Fig. 3.6 are presented in Table 3.3. Units G1 and G2 are assumed to be unsuitable for primary frequency control, given their slow dynamics. In our simulation, we include a WF in bus 10 modelled as an aggregation of several identical WTs with the same operating conditions. Data for wind and load profiles corresponding to the GB system are used, taken from [102]. The optimisation problem is formulated in MATLAB via the modelling layer YALMIP [103], and calling Gurobi as the solver, with default parameterisation. All simulations were carried out on a standard laptop with AMD Ryzen 7 5800H CPU, with a clock rate of 3.20 GHz and 16 GB of RAM.

3.4.1 Impact of System-Wide Conditions on Optimal $\widetilde{K}_{\mathbf{sys}}$

Several results of the detailed dynamic model, implemented in MATLAB/Simulink, are used here to showcase the dependency of $\widetilde{K}_{\text{sys}}^{\text{opt}}$ on system-wide conditions. As discussed in Section 3.2.2, the optimal $\widetilde{K}_{\text{sys}}$ is such a value that generation cost is minimised on the premise of system frequency security. For clarity in the explanations, we focus on cases where the frequency-nadir limit is the binding constraint (i.e. $\Delta f_{\max} \leq 0.8$ Hz), a typical case in low-inertia systems as demonstrated by [53, 69]. Hence, the optimal $\widetilde{K}_{\text{sys}}$ is such a value that the frequency drop is contained at exactly 0.8 Hz. The contingency under consideration is a generation loss of 5% of the total installed thermal capacity, i.e. $\Delta P_L = 0.05\, C_{\text{SG}}$, where C_{SG} is the total installed capacity of thermal generators in the system.

Interpretation of optimal $\widetilde{K}_{\mathbf{sys}}$

We consider a case with $v_w = 10$ m/s and $pl = 20\%$, and include the Center-of-Inertia (CoI) frequency excursions in Fig. 3.7, where the optimal $\widetilde{K}_{\text{sys}}$ arrests the FN to 0.8 Hz exactly. It is evident that the FN improvement is conditional on the value of $\widetilde{K}_{\text{sys}}$: a small value incurs a poor performance of post-fault frequency response, infringing the frequency security rules. In contrast, despite a medium value raising the FN to a better extent, the generation cost would not be minimum, as containing the FN well above the critical value of 0.8 Hz implies that more headroom than strictly necessary has been scheduled in the thermal generators (with

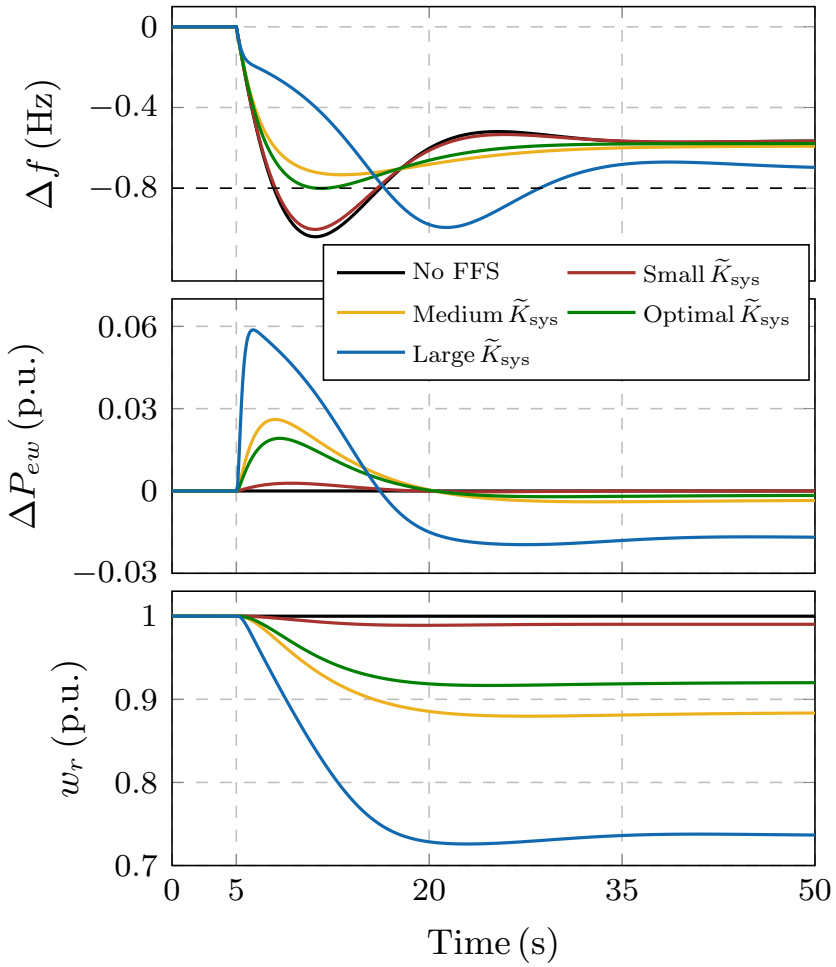

Figure 3.7: Results for Case A-1: (a) System frequency; (b) Active power output of WF; (c) Rotor speed of WTs.

the associated increase in system operation costs). It is noteworthy that a large value of $\widetilde{K}_{\text{sys}}$ instead worsens the FN incurring an SFD, as the electrical power reduces dramatically with the declining rotor speed of DFIG-based WTs, also shown in Fig. 3.7. The DFIG is operated stably above the minimum permissible rotor speed which is 0.7 p.u., considering DFIG-based WTs' rotors are generally designed to operate from 0.7 p.u. to 1.3 p.u. dynamically.

Optimal $\widetilde{K}_{\mathbf{sys}}$ depending on wind speed

With increasing wind speed 'v_w', the results demonstrate that the optimal value of $\widetilde{K}_{\text{sys}}$ follows a monotonically decreasing function, as illustrated in Fig. 3.8, which was obtained considering again a $pl = 20\%$. This trend can be understood by rewriting (3.8) to express the initial value of ADG as follows:

$$\begin{aligned} \text{ADG}_0(v_w) &= \widetilde{K}_{\text{sys}} \cdot (w_{r0}^2 - w_{r,\min}^2) \\ &= \widetilde{K}_{\text{sys}} \cdot \left[\left(\frac{\lambda_{\text{opt}} v_w}{R} \right)^2 - w_{r,\min}^2 \right] \\ &= \widetilde{K}_{\text{sys}} \cdot G(v_w) \end{aligned} \tag{3.14}$$

with the initial rotor speed w_{r0} assuming that WTs are operated in MPPT mode. The monotonically increasing function $G(v_w)$ entails a fall of $\widetilde{K}_{\text{sys}}^{\text{opt}}$ to balance the contribution from growing wind speeds.

Optimal $\widetilde{K}_{\mathbf{sys}}$ vs. wind penetration level

It can be clearly seen in Fig. 3.8 that the penetration level of wind, '*pl*', induces a steep decrease in the optimal value of $\widetilde{K}_{\text{sys}}$, where the results were obtained for a fixed $v_w = 10$ m/s. To better understand this trend, let us consider the definitions of active power increase in the WTs as dictated by the droop control, and of wind penetration level as a ratio of the rated power of

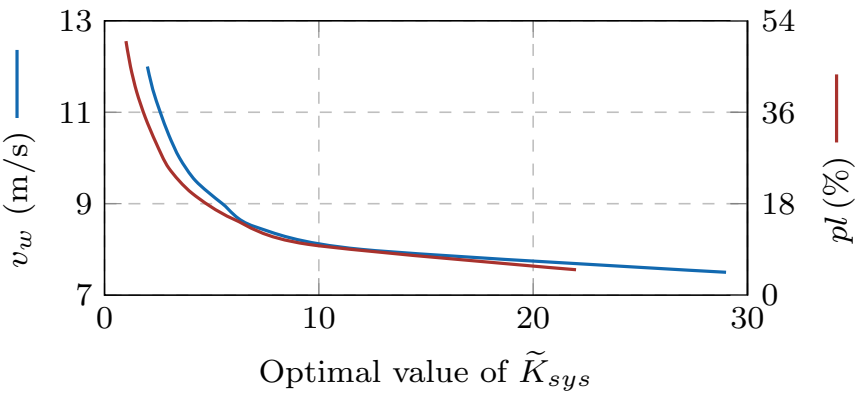

Figure 3.8: Optimal $\widetilde{K}_{\text{sys}}$ versus wind speed and wind penetration level '*pl*'.

the WF to total installed generation capacity:

$$P_{\text{droop}} = \underbrace{\widetilde{K}_{\text{sys}} \cdot (w_r^2 - w_{r,\min}^2) \cdot \Delta f}_{\text{per unit value}} \cdot C_{\text{WF}} \tag{3.15}$$

$$pl = \frac{C_{\text{WF}}}{C_{\text{WF}} + C_{\text{SG}}} \Rightarrow C_{\text{WF}} = \frac{pl}{1 - pl} \cdot C_{\text{SG}} \tag{3.16}$$

where C_{WF} corresponds to the rated power of the WF. Substituting (3.16) into (3.15) yields:

$$P_{\text{droop}} = \widetilde{K}_{\text{sys}} \cdot (w_r^2 - w_{r,\min}^2) \cdot \Delta f \cdot C_{\text{SG}} \cdot H(pl) \tag{3.17}$$

with $H(pl) = \frac{pl}{1-pl}$. Therefore, a decline of $\widetilde{K}_{\text{sys}}^{\text{opt}}$ moderates the contribution of $H(pl)$, which is a monotonically increasing function.

3.4.2 Assessment of Conservativeness and Reliability of Secure OCT(M)

As discussed in Section 3.3.1, appropriate tuning of the hyperparameter ω in the Secure OCT(M) is needed to guarantee frequency security in all instances, i.e. achieve full reliability. A larger value of ω implies that the prediction accuracy of the classifier will be reduced to a certain extent, as some 'safe' cases are likely to be misclassified, which is indicative of the conservativeness of the approach. In this section, we employ two metrics, precision and recall, to assess our proposed model's reliability and conservativeness. If 'safe' and 'unsafe' are defined as 'positive' and 'negative' outcomes respectively, a larger number of false-positive observations render a lower precision, i.e., a less reliable model. Likewise, the larger the number of false-negative cases is, the more conservative the model would be, i.e., the lower recall is. In this section, a total of 1500 operating scenarios were generated based on weekly wind and demand forecasts. These scenarios were uniformly sampled to reflect the expected variability across a typical scheduling week. For each scenario, dynamic simulations were conducted to determine frequency stability, and a binary classification label (secure or insecure) was assigned. The dataset was split into 70

The effect of different values of ω on the performance of the Secure OCT(M) is illustrated in Fig. 3.9, which shows a decrease of recall and increment of precision in the studied range of ω. A value of $\omega = 30$ fully mitigates the risk of 'false safe' predictions (100% precision). Regarding computing time, running the dynamic simulations for labelling the 1500 samples (i.e., creating

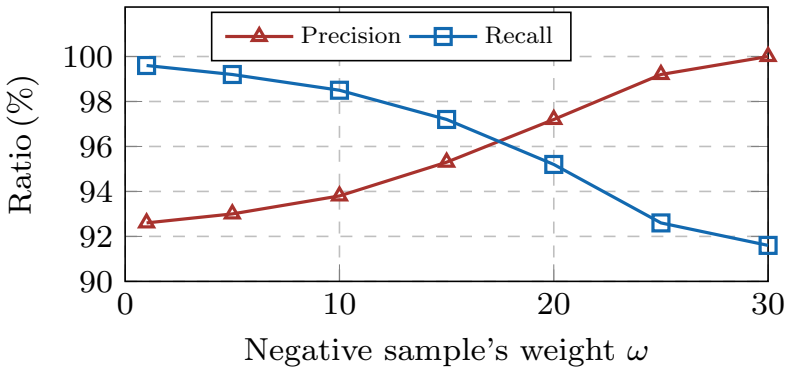

Figure 3.9: Prediction performance versus negative sample's weight ω.

Table 3.4
Assessment indices of three classification models

	Precision (%)	**Recall (%)**	**Depth**
Secure OCT(M) ($\omega^* = 30$)	100	91.62	2
OCT(M) in [48]	98.36	98.07	2
CART	86.69	96.65	6

the data set) took roughly two days, while just over 36 min were necessary for training the Secure OCT(M) with $\omega = 30$. The OCT training process involves solving a MILP problem. Using a small training dataset significantly reduces the training time. Consequently, frequency constraints can be updated monthly using small-size training datasets generated from short-term wind and load predictions. This approach ensures that the model stays up-to-date and efficient by continuously incorporating the latest data.

For benchmarking our proposed Secure OCT(M), two other tree methods are considered: conventional decision tree (CART), and OCT(M) in [48]. Table 3.4 presents the evaluation of the conservativeness and the reliability of these three models on the testing set. The results show that hyperparameter ω in the Secure OCT(M) improves the classifier's reliability by erasing false-positive samples by inevitably misclassifying some 'safe' scenarios. Accordingly, our pro-

posed model becomes more conservative but fully reliable, in contrast with the other two tree models.

In addition, OCT challenges the notion that optimal methods merely overfit the training set and fail to generalize effectively. The OCT model has been proven more efficient and robust versus CART in learning the ground truth of data, thus endowed with the adaptability of diverse datasets [95]. The learning curve shown in Fig. 3.10 represents the learning performance of our proposed OCT model on the training and validation sets as a function of the training set size, where the cross-validation technique has been used. The number of samples used in the training set increases from 500 to 2000. The prediction accuracy serves as the performance metric for both the training score and validation score. To diagnose the accuracy and generalisability of the model, we resort to the concept of bias-variance tradeoff. Bias refers to a measure of how closely a model's predictions match the true outcomes, while variance suggests how much the model's predictions vary when trained on different subsets of the training data. In Fig. 3.10, the training and validation scores converge to a high accuracy as the number of training samples increases, where high accuracy indicates low bias and convergence implies low variance. Hence, the result suggests that our proposed OCT model is a good fit, i.e. low bias and low variance, which has sufficient capacity to predict and generalise well. Note that Fig. 3.10 conveys not just the central tendency, i.e. mean scores, but also the variability, i.e. the filled area between the mean scores and the standard deviations, which helps to understand the reliability of the

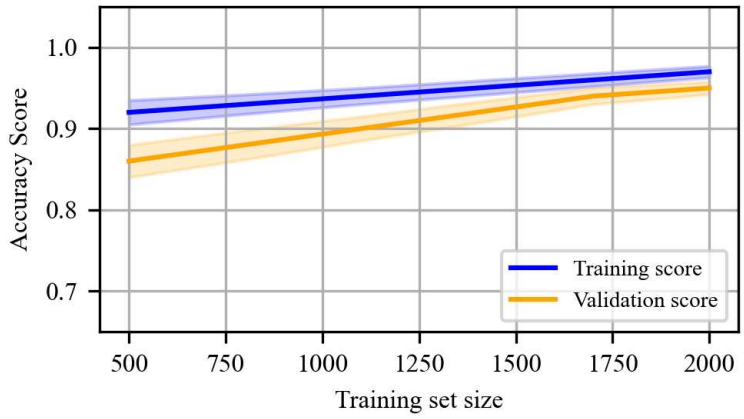

Figure 3.10: Learning curve of OCT(M): relationship between prediction accuracy and training set size.

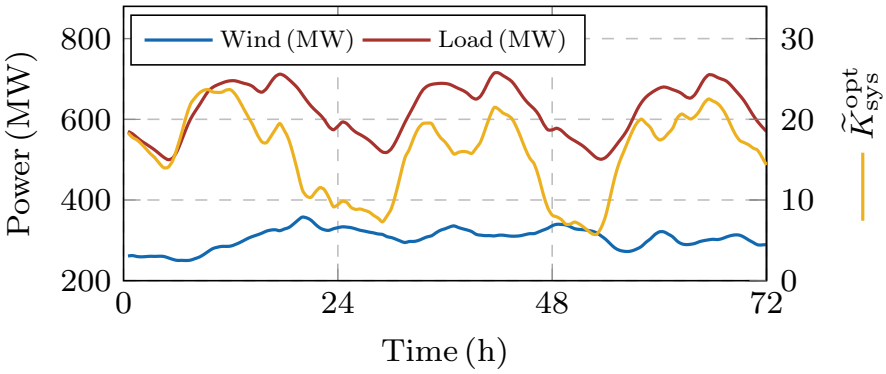

Figure 3.11: Three-day wind and load profiles and optimal $\widetilde{K}_{\text{sys}}$.

model.

3.4.3 Validation of Frequency-Security Constraints

In order to validate the frequency-security constraints defined by the Secure OCT(M), in this section the dispatch solutions from a multiperiod OPF model were fed into the dynamic model in MATLAB/Simulink. The system parameters in the scheduling model were set as follows: load demand $P_D \in [500, 715]$ MW and $pl = 30\%$. The contingency which defines the need for frequency services, ΔP_L, is optimally modelled as the largest single power output at any point

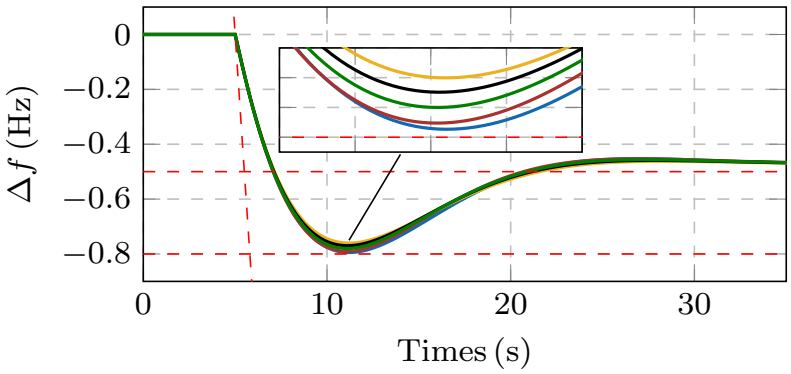

Figure 3.12: Dynamic simulations from five different OPF solutions.

Table 3.5
FREQUENCY NADIR ASSESSMENT

Linearisation Models	**Nadir (Hz)**		
	Min	**Mean**	**Max**
Secure OCT(M)	0.686	0.735	0.796
OCT(M) in [48]	0.740	0.789	0.823

Table 3.6
DISPATCH RESULTS UNDER SECURE VS. STANDARD OCT(M)

	Total cost (m)	**Reserves (MW)**
Secure OCT(M)	69.6	91.65
OCT(M) in [48]	65.6	88.35
Difference	0.6%	6.4%

in time, therefore this value is co-optimised along with the volume of frequency reserves and $\widetilde{K}_{\text{sys}}$. Fig. 3.11 displays a set of $\widetilde{K}_{\text{sys}}^{\text{opt}}$ obtained in the course of system scheduling for a three-day profile of load and wind power. It can be seen that the optimal $\widetilde{K}_{\text{sys}}$ fluctuates under the joint effect of wind speeds and pre-fault dispatches of thermal units. Simultaneously, the optimal $\widetilde{K}_{\text{sys}}$ is shown to be inversely proportional to wind power (i.e., wind speed), as demonstrated in Section 3.4.1.

Dynamic simulations were run in the Simulink model by feeding the dispatch solution for 5

different half-hour periods, arbitrarily chosen among all dispatch solutions for the three-day period in Fig. 3.11. The results in Fig. 3.12 demonstrate that the requirements for RoCoF, FN and q-s-s are respected in all cases, namely $(df/dt)_{\max} \leq 1.0$ Hz/s, $\Delta f_{\max} \leq 0.8$ Hz and $\Delta f^{\text{ss}}_{\max} \leq 0.5$ Hz. The nadir constraint is binding in all five OPF instances, while Fig. 3.12 shows that in some of these cases the FN does not hit the limit of 0.8 Hz. The trigger for this slight conservativeness in the nadir constraint is the use of the parameter ω in the Secure OCT(M): in order to achieve 100% precision, certain 'safe' observations in the vicinity of the FN limit are misclassified. However, compared with the OCT(M) with no security guarantee, the results in Table 3.5 demonstrate that the Secure OCT(M) achieves frequency reliability in all instances. This effect is also seen in the average half-hourly frequency reserves dispatched by the OPF, i.e. the average headroom in thermal generators, presented in Table 3.6: while our proposed method incurs in 6.4% extra reserves compared to the standard OCT(M), this safety margin allows achieving full reliability. The increase in system operating costs due to these extra reserves is of 0.6%, which is the cost of guaranteeing security at all times.

3.4.4 Impact of Optimal FFS on Power System Operating Cost

The cost of frequency services versus the wind penetration level, ranging from 0 to 50%, is depicted in Fig. 3.13, considering two scenarios: (1) with optimal FFS; and (2) without optimal FFS. As expected, WTs providing FFS indeed share the burden with thermal units of

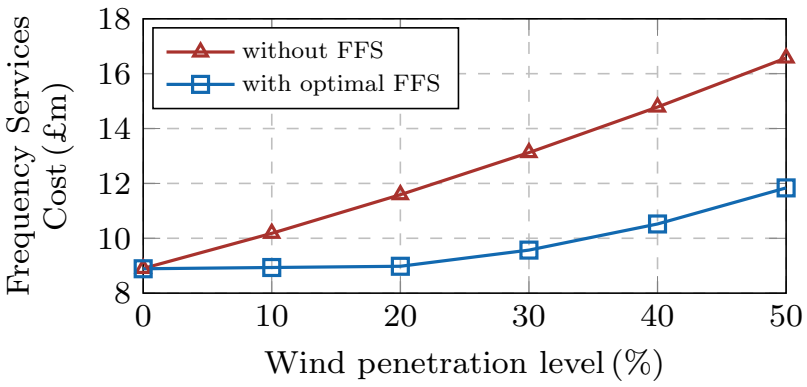

Figure 3.13: Impact of optimal FFS on the weekly cost of frequency services.

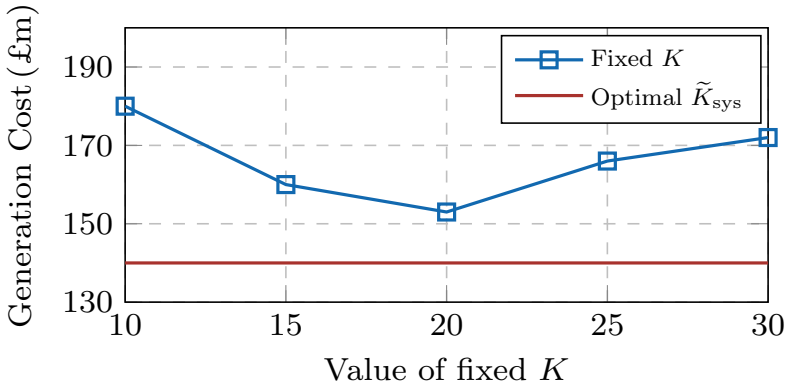

Figure 3.14: Weekly generation cost with different control strategies, for a 50% wind penetration level.

supporting frequency, which reduces the volume of necessary headroom in SGs compared to the case without optimal FFS, and thus decreases the system cost of frequency services.

Finally, we evaluate the value of optimising $\widetilde{K}_{\text{sys}}^{\text{opt}}$ in terms of system savings. To do this, the weekly operating cost resulting from the OPF is compared with a case where the droop gain is not optimised as a function of the system operating conditions, i.e. the simpler control strategy of fixing the value of K in (3.8) to a pre-set value. The results for the 50% wind penetration case are included in Fig. 3.14, where a range of values for the fixed $K \in [10, 30]$ has been considered. It should be noted that in Fig. 3.14 the generation cost based on optimal $\widetilde{K}_{\text{sys}}$ is constant, not

a function of the value of fixed K. The results in Fig. 3.14 show that generation cost decreases until $K = 20$, which is driven by the increasing FFS capability of WTs. After that point, the underproduction process of WTs triggers the growth of generation cost, as discussed in Section 3.4.1. It is clear that dynamically optimising $\widetilde{K}_{\text{sys}}$ significantly outperforms the 'fixed K strategy', leading to a minimal reduction of around 8% in system operating cost, which is calculated at $K = 20$ (implying that this is the optimal value in the set of 'fixed K' candidates). Furthermore, it is important to point out that the optimal value of fixed K can only be obtained by incorporating the fixed WT droop control into economic optimisation through the proposed data-driven method. This value of $K = 20$ could not be computed using previously proposed models, thus highlighting the benefit of the proposed framework.

3.5 Conclusion and Future Work

This paper proposes a fast droop control for WTs via an adaptive droop gain. The gain is optimised to maximise system-wide economic savings, using an OPF model with frequency-security constraints that are extracted from a detailed dynamic power system model. This is achieved by resorting to a data-driven method based on a revised optimal classification tree, which is demonstrated to achieve full frequency reliability with limited conservativeness. A modified IEEE 14-bus system has been used to conduct several case studies, assessing the effectiveness and the economic value of this system-aware control strategy for WTs. The results

highlight the importance of dynamically optimising the value of the adaptive droop gain within the system scheduling algorithm.

The main computational cost of the proposed method lies in the offline data generation phase, where dynamic simulations are required for a wide range of power system operating conditions. As the number of system scenarios increases—due to variations in load, wind generation, or network topology—the volume of required simulations grows proportionally. Additionally, in systems with a larger number of inverter-based resources (e.g., wind farms), the number of droop control parameters increases, introducing higher dimensionality to the control space. This expansion leads to more iterations for sampling and classification during offline training. However, the framework remains scalable in practice because the computationally expensive simulations are confined to the offline stage. Once the classifier is trained, online evaluation is fast and lightweight, making the method suitable for real-time decision support.

Future work will extend the scheduling model to a stochastic framework, to consider the inherent uncertainty in wind generation. In addition, the optimal KE extraction should be studied in view of every WT location within a WF, analysing if wake effects have a significant impact on the control strategy. Furthermore, the CoI-based model calls for a re-evaluation, i.e., the local frequency should be assessed for the purpose of designing local controllers for WFs providing frequency support.

Chapter 4

Efficient Sampling for Data-Driven Small-Signal Stability Constraints via Participation Analysis

With the increasing penetration of renewables and inverter-based resources (IBRs), traditional static power system operations, such as optimal power flow (OPF), are challenged to ensure real-time grid stability. Recent studies have shown the potential of including stability constraints into operation for stability support. However, most of the existing approaches assume that an analytical stability index exists and/or overlooks the heterogeneous dynamics and control of IBRs, resulting in conservative operations. Notably, the flexible and non-standardized internal

control systems endow inverters with significant potential to actively regulate grid stability amid the intermittent nature of renewable energy inputs. Therefore, this paper models the stability index as a function of both static operation points and device-level inverter control parameters. Due to the black-box settings of the IBR-rich power system, a constrained logistic regression-based stability assessment model is continuously updated on a fixed rolling window basis. To prepare a balanced and representative dataset, critical samples near the stability boundary are identified via the proposed participation-analysis sampling strategy. Finally, the performance of the proposed data-driven OPF with flexible IBR control parameters is demonstrated on a modified IEEE bus-14 system.

4.1 Introduction

The global drive to decarbonize electrical energy is rapidly advancing, marked by substantial increases in renewable capacity and the transition of numerous systems to relying on renewable sources for tripling renewable power capacity by 2030 as a goal [104]. Despite progress, several planning and operational challenges persist, particularly related to the intermittent nature of wind and solar resources and the interface of these systems with the grid using inverters. These inverters, known as inverter-based resources (IBRs), are crucial for integrating renewable energy sources into the grid [105].

The increasing deployment of inverters in power systems raises concerns about system dynamics and stability [19]. Incidents have linked inverters to issues such as unexpected disconnections during fault events and poorly damped responses to voltage fluctuations [20]. It is particularly problematic that instability may arise in the phase-locked loops of grid-following inverters integrated into a grid with low strength, often denoted as a weak grid [21]. Operators noted the emergence of poorly damped oscillations in areas where inverters dominate, expecting further investigation [22]. These stability challenges may intensify as inverter-based resources play a pivotal role in carbon-neutral power systems.

As previously elaborated, potential dynamic stability concerns, including small-signal instability, may manifest when integrating these resources into a weak grid [23]. In addition, the variable nature of renewable resources, such as wind and solar, possibly exposes power systems to small-signal instability, as a result of rapid variations of operating points of systems [24]. On the other hand, non-synchronous generations based on IBRs are steadily displacing conventional generators in current power systems, by which the inverters generally fail to enhance system inertia and thus small-signal stability [25]. Therefore, the small-signal security assessment is warranted to be carried out in the course of economic dispatching, such as Optimal Power Flow (OPF). The Small-Signal Stability Constrained Optimal Power Flow (SSSC-OPF) is an exemplary model that provides comprehensive re-dispatch details to ensure small-signal stability, taking into account both economic goals and technical limitations. Modeling the SSSC-OPF

directly is challenging due to the spectral abscissa's implicit dependence and non-Lipschitz behavior within the system state matrix. The papers solving SSSC-OPF are categorised as follows, considering small-signal stability constraints endowed with the non-smooth and non-linear nature.

- Iterative methods utilising eigenvalue sensitivities: This group of methods have used first-order and/or second-order Taylor series expansion of small-signal stability constraints where the gradients and/or Hessian matrices are evaluated by perturbations or computed by closed-form formulations in each iteration step. [26] developed an SSSC-OPF model to maintain security under stressed conditions by approximating the small-signal stability constraint with a first-order Taylor series expansion and successively solving SSSC-OPF. In addition to first-order sensitivities, [27–30] have also utilized second-order sensitivities to track dominant eigenvalues as accurately as possible and facilitate the efficiency of the iteration process.

- Noniterative methods based on semidefinite programming (SDP) from Lyapunov stability criterion: Without resorting to eigenvalue analysis, this category of methods derives explicit and equivalent small-signal stability constraints through working over differential-algebraic equations describing dynamic and algebraic relationships in power systems. Building on the insights from [31], [32] proposed to use a bilinear matrix inequality (BMI) for small-signal stability and SDP with objective penalization for efficient large-scale sys-

tem modelling. To ensure sufficient stability margins in inverter-based microgrids during optimal power generation, [33] applied SDP and parabolic relaxation to address non-linear, non-convex BMIs, preserving the conditions for small-signal stability [34], which is prohibitive for the current optimization tools.

Nevertheless, iterative methods relying on eigenvalue analysis face substantial computational challenges due to the repeated updates of the gradient and/or Hessian matrix, coupled with model linearization after each iteration, resulting in significant time consumption. In contrast, non-iterative methods based on SDP bypass these iterative updates but present two key challenges. First, ensuring a guarantee of convergence is essential to secure reliable solutions within a reasonable timeframe, especially in non-convex optimization problems where convergence is not inherently assured. Second, developing tighter convex relaxations is critical for enhancing solution accuracy by minimizing the gap between the relaxed and true optimal solutions, making the approach more effective and suitable for real-world applications. Furthermore, the aforementioned methods cannot be utilized when analytical models are unavailable, a likely scenario, as state-space models require detailed knowledge of each machine's hardware design and control algorithms. Unfortunately, this information is often inaccessible due to manufacturers withholding it and the lack of standardization across suppliers [22].

By reducing reliance on iterative eigenvalue computations and minimizing dependence on SDP relaxations, data-driven methods lower computational burdens and enhance real-time decision-

making [35]. These methods effectively capture the system's underlying properties by concentrating on key security attributes and the most relevant features, eliminating the need for complex model-based analysis while preserving essential dynamic information [36]. Advancements in data-driven methods have reshaped power system analysis, enabling more effective stability assessment and control. The Koopman operator framework has emerged as a powerful technique for capturing system dynamics and estimating the region of attraction through dominant eigenfunction analysis, eliminating the reliance on explicit system models [37]. Similarly, data-driven Lyapunov functions have been developed using real-time measurement data, offering a model-free approach to stability certification while bypassing traditional analytical formulations [38]. In operational stability analysis, techniques such as inertia estimation and frequency monitoring have been seamlessly integrated with wide-area measurement systems, leveraging machine learning algorithms for real-time grid monitoring [39]. Model Predictive Control has also benefited from data-driven enhancements, enabling adaptive and optimal decision-making in rapidly changing environments [40]. Furthermore, reinforcement learning has advanced learning-based controllers by enabling autonomous system operation under uncertain and dynamic conditions [41]. Collectively, these innovations demonstrate the transformative potential of data-driven approaches in modern power system stability and control through adaptive, scalable, and model-free frameworks.

However, the predictive performance of data-driven models is strongly influenced by the quality

of the training data, which should exhibit comprehensive coverage, sufficient variability, and balance [106]. Historical sampling generates operating conditions (OCs) by fitting probability distributions to past records and applying Monte Carlo methods [107], [108]. While useful, this approach is limited when future OCs diverge from historical trends or when the data predominantly represents secure conditions. To achieve robust model performance, the training dataset must include a balanced mix of secure and insecure conditions. In contrast, generic sampling strategies [109], [110] generate uniformly distributed data points across the feasible space, providing thorough coverage of all potential OCs. However, this method can be computationally expensive for large systems, often resulting in excessive data with limited contribution to the knowledge base. A well-designed sampling strategy must balance efficiency with the need for diverse, representative data.

To address the aforementioned challenges, Liu et al. [35] proposed a sampling method based on voltage sensitivity analysis to reduce feature dimensions and compress the sampling space. The approach involved two key steps. First, node voltage magnitudes were selected as features instead of active power, striking a balance between economic efficiency and system stability. Second, the 'direct walk' method was introduced, involving iterative optimization to generate critical samples closer to the stability boundary, effectively shrinking the sampling space. On the other hand, extensive research underscores that, in addition to OCs, the internal control parameters of IBRs are crucial for enhancing the small-signal stability of power systems [111,112].

Accordingly, dynamically tuning these control parameters during the power system scheduling process offers significant potential for improving small-signal stability, particularly in systems with a high penetration of renewable energy. This vision aligns with the concept of a software-defined grid, where IBR control strategies and parameters can be centrally optimized and dynamically updated via fast communication [63].

Given this context, this paper intends to present a novel scheduling strategy at the system level that leverages the flexible control merits of IBRs at the device level, offering significant practical value by relying solely on the apparatus's impedance models. Integrating IBR control parameters as decision variables within data-driven stability constraints enables system-level analyses to accurately enable individual IBR units to provide complementary stability support services autonomously. The main contributions of this paper are threefold:

a. To bridge the gap between system-level operations and device-level controls, enabling IBRs to deliver ancillary services that enhance small-signal stability through dynamic tuning control parameters during scheduling.

b. To largely decouple, for the first time, the small-signal stability and system operation cost, ensuring system stability almost without resorting to an economically disruptive rescheduling process.

c. To propose an efficient sampling scheme which leverages participation analysis to select

critical samples close to the stability boundary, enriching the training database with valuable information.

d. A constrained logistic regression-based stability assessment model is proposed to capture the most recent static operating status, dynamic IBR control strategies, and stability performance. Once trained, the stability assessment is encoded as stability constraint into real-time OPF with limited computation and cost overhead.

4.2 Participation-Analysis Sampling Based on Impedance Model

4.2.1 Preliminaries

The gradient-based sampling has been proposed based on the previous study of the whole-system impedance model and impedance participation analysis [22], [112], i.e., the grey-box method. To enhance understanding, these concepts are briefly reviewed first.

Whole-System Impedance Model

The whole-system impedance model forms the foundation for the participation analysis detailed in the subsequent section. An N-node meshed power network has been depicted in Fig. 1,

where small virtual voltage injections $\hat{v} = [\hat{v}_1, \hat{v}_2, ..., \hat{v}_N]^T$ are applied in parallel with each apparatus to induce corresponding voltage responses $\Delta i = [\Delta i_1, \Delta i_2, ..., \Delta i_N]^T$. The transfer matrix, denoted as whole-system impedance $\hat{Z}(s)$, maps the injected voltages $\hat{v}$ as input to the perturbed currents Δi as output, such that $\Delta i(s)/\hat{v}(s) = \hat{Z}(s)^{-1} = \hat{Y}(s)$. Note that the validity of the linearised system around the operating points requires $\hat{v}$ to have a sufficiently small magnitude. In [22], the whole system admittance matrix $\hat{Y}$ is given as follows:

$$\hat{\boldsymbol{Y}} = (\boldsymbol{I} + \boldsymbol{Y}_{\text{net}} \boldsymbol{Z}_m)^{-1} \boldsymbol{Y}_{\text{net}} \tag{4.1}$$

where

$$\boldsymbol{Z}_m = \text{diag}(Z_1, Z_2, ..., Z_N) \tag{4.2}$$

serves as a diagonal matrix containing the impedances of all terminal apparatus, such as generators, IBRs and loads. $\boldsymbol{Z}_{\text{net}}$ is the nodal admittance matrix of the network from which the nodal impedance matrix $\boldsymbol{Y}_{\text{net}}$ can be derived.

$\hat{\boldsymbol{Y}}$ is an $N \times N$ transfer function matrix with all its elements sharing identical poles, corresponding to the system's eigenvalues. The diagonal elements of $\hat{\boldsymbol{Y}}$ have a well-defined physical interpretation. For instance, the first diagonal element, $\hat{\boldsymbol{Y}}_{11}$ shown in Fig. 4.1, represents the admittance of a loop formed by Z_1, i.e. the impedance of apparatus at the first node, and Z_{g1}, i.e. the impedance of the rest of the networks seen from Z_1. Hence, $\hat{Y}_{11}$ can be expressed as

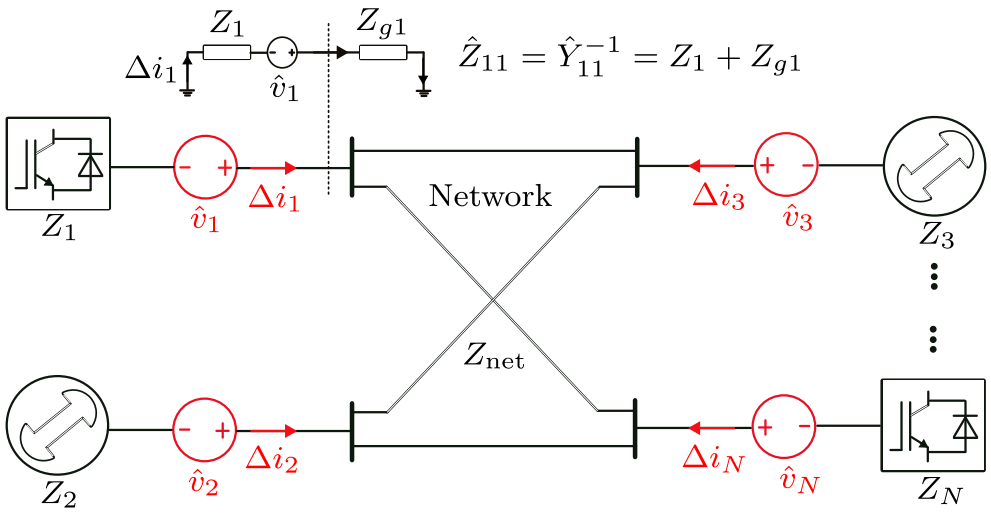

Figure 4.1: Demonstration of the whole-system admittance model. Virtual voltage injection $\hat{v}$ to generate Δi.

$\hat{Y}_{11} = \hat{Z}_{11}^{-1} = (Z_1 + Z_{g1})^{-1}$, and this concept extends to any other node k

$$\hat{Y}_{kk} = (Z_g + Z_{gk})^{-1}. \tag{4.3}$$

Furthermore, individual diagonal elements may exhibit different excitation levels, leading to variations in the magnitudes of resonant peaks at a specific pole. These variations reflect the relative participation of various nodes in a particular mode, which provides [112] with the basis for extracting accurate participation factors from the whole-system matrix $\hat{\boldsymbol{Y}}$.

Impedance Participation Analysis

As previously noted, the poles of the transfer function $\hat{Y}_{kk}$ directly correspond to the system's eigenvalues. Thus, [112] reveals that an eigenvalue's sensitivity to an apparatus's impedance is determined by the residue of the whole-system admittance, as viewed by the same apparatus,

where the residue is defined as the *impedance participation factor*

$$p_{\lambda,Z_k} \triangleq -Res_{\lambda}^{*}\hat{Y}_{kk} \tag{4.4}$$

such that

$$\Delta\lambda = \langle p_{\lambda,Z_k}, \Delta Z_k(\lambda)\rangle \tag{4.5}$$

where $\hat{Y}_{kk}$ is the whole-system admittance seen from node k and ΔZ_k considers a small perturbation on the impedance of apparatus at k-th node. λ is an eigenvalue of the state-space matrix $\boldsymbol{A}$ indicating an oscillatory mode in the system. It should be noted that the eigenvalues of the system serve exactly the poles of the transfer function $\hat{Y}_{kk}$. And $\langle .,. \rangle$ is the Frobenuis inner product of two matrices and $Res_{\lambda}^{*}\hat{Y}_{kk}$ is the conjugate transpose of the matrix of residues of $\hat{Y}_{kk}$ at $s = \lambda$. As derived from (4.5), $Res_{\lambda}^{*}\hat{Y}_{kk}$ quantifies the sensitivity of eigenvalues to changes in the impedance of apparatus, making it known as the impedance participation factor.

Small-Signal Dynamics in GFM and GFL

The duality between the small-signal dynamics of GFM and GFL converters is thoroughly examined in [111], where the synchronisation dynamics are described by $S_{i\theta}$ and $S_{v\theta}$ as follows:

$$S_{i\theta} = s^2 \underbrace{\frac{T_f}{m_d}}_{J} + s \underbrace{\frac{1}{m_d}}_{K_D} + \underbrace{(-I_{q0})}_{K_s} \tag{4.6}$$

and

$$S_{v\theta} = \frac{1}{1 + s\frac{k_{p,\mathrm{PLL}}}{k_{i,\mathrm{PLL}}}}(s^2 \underbrace{\frac{1}{k_{i,\mathrm{PLL}}}}_{J} + s \underbrace{\frac{k_{p,\mathrm{PLL}}}{k_{i,\mathrm{PLL}}} V_{d0}}_{K_D} + \underbrace{V_{d0}}_{K_s}) \tag{4.7}$$

The standard synchronising control strategies are demonstrated in [111], where the open-loop transfer function of GFM's droop control is $G_{\mathrm{FD}} = \frac{m_d}{1+T_f s}$ while that of GFL's PLL, i.e. a PI controller, is $G_{\mathrm{PLL}} = k_{p,\mathrm{PLL}} + \frac{k_{i,\mathrm{PLL}}}{s}$. Here we define $f_d = \frac{1}{T_f}$ as the bandwidth of droop control. As analogues to the swing motion of a virtual synchronous generator with inertia J, damping torque coefficient K_D and synchronising torque coefficient K_S, noting that I_{q0} and V_{d0} are the q-axis current component and d-axis voltage component at an equilibrium point. Authors in [111] conclude that raising the droop gain m_d for the GFM and expanding the PLL bandwidth f_{PLL} for the GFL, i.e. increasing G_{PLL}, both contribute to instability. Hence, higher synchronization controller gains essentially render inverters more prone to instability. Furthermore, the voltage loop bandwidth in GFM (f_v) and the current loop bandwidth in GFL (f_i) also influence small-signal stability when interacting with grid dynamics [111].

4.2.2 Motivation

Compressing the sampling space can significantly benefit data generation and storage, as sampling in high-dimensional spaces is challenging, and much of the generated data contributes minimal additional value to the database [106]. Moreover, efficient learning requires generating critical samples situated closer to the decision boundary. On the other hand, one challenge in

stability analysis is the absence of standardised and precise analytical models for the dynamic behaviour of IBRs. Although synchronous generators (SGs) operate based on physical principles, the performance of IBRs is highly dependent on their internal control systems, which are highly adaptable and have not yet been standardised [112]. Manufacturers often treat these control systems as proprietary, sharing only black-box models with system operators. However, the existing efficient sampling method in [35] based on white-box, i.e. eigenvalue analysis of state-space model, cannot apply to black-box models. In addition, considering the potential savings in electricity generation costs, [35] adopts a strategy that relies exclusively on the voltage magnitudes of the generators to stabilise the power system, but this offers limited effectiveness in improving small-signal stability during scheduling.

Hence, our expected sampling method should be featured with the following merits:

a. Generating samples without requiring detailed mathematical models of power systems

b. Identifying additional features that influence stability without directly compromising costs

c. Sampling close to the boundary to add maximal information into the dataset

d. Compressing sampling interval to cover the partial boundary and balance secure/insecure samples

4.2.3 Feature Selection via Participation Analysis

In our proposed sampling method, we select the voltage magnitudes of apparatus and stability-sensitive parameters based on Section 4.2.1 (i.e. m_d, f_d, f_{PLL}, f_i and f_v) of the participating apparatus as potential sample features, thereby balancing stability and cost neutrality, since the generation cost of power systems is directly affected by the scheduled active power outputs of generation plants. The participation analysis proposed in [112] is intrinsically valuable for identifying the most stability-relevant features, thereby effectively reducing the dimensionality of the sampling space. Specifically, (4.5) forms the core of the participation analysis, facilitating the tracking of parameters in control loops within the participating apparatus that underlie instabilities even without prior knowledge of the power system's state-space model:

As shown in Fig. 4.2, stages 1 and 2 of our sampling scheme utilize participation analysis to filter and identify the internal control parameters of the dominant apparatus responsible for the root cause of instability.

Sampling Stage-1

In this stage, for a given mode, i.e. a particular eigenvalue λ_n, we need to examine the participation of each apparatus to locate the dominant participants. The required prior information includes the impedance Z_k for all apparatus in the system and nodal admittance matrix Y_{net}, derived from the network's topology and line impedances. To this end, a uniform magnitude

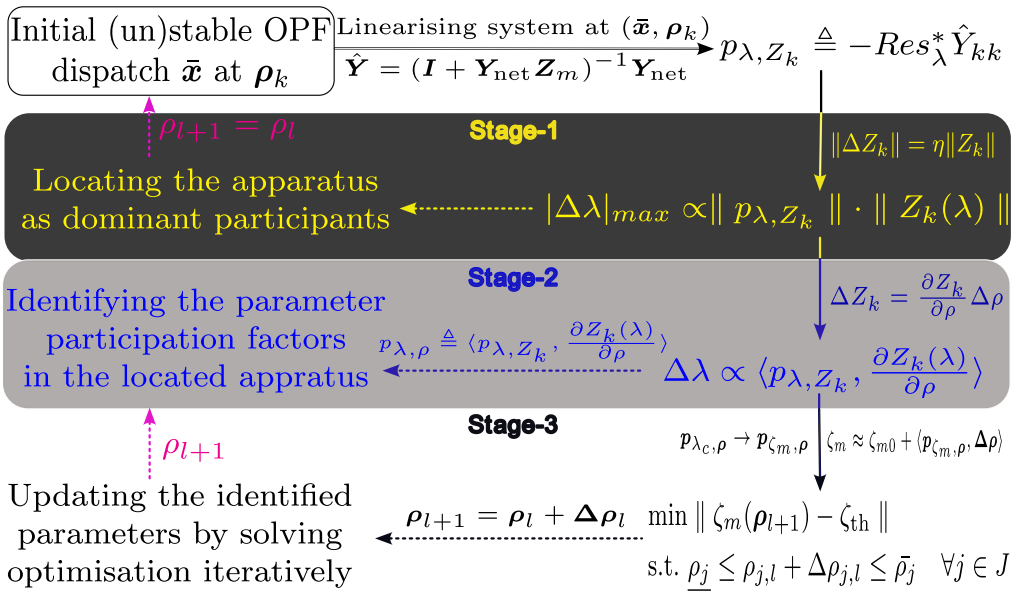

Figure 4.2: Feature selection cycle based on participation analysis.

perturbation is introduced to each Z_k to observe its impact on the eigenvalue λ_n. This perturbation is scaled by $|Z_k|$, expressed as $\|\Delta Z_k\| = \eta \|Z_k\|$, where η is a small positive constant. Using the Cauchy inequality, it follows that:

$$|\Delta\lambda_n| = |\langle p_{\lambda_n, Z_k}, \Delta Z_k(\lambda_n) \rangle| \leq \|p_{\lambda_n, Z_k}\| \cdot \|\Delta Z_k(\lambda_n)\| \tag{4.8}$$

which gives

$$|\Delta\lambda_n|_{\max} = \|p_{\lambda_n, Z_k}\| \cdot \|\Delta Z_k(\lambda_n)\| = \eta \|p_{\lambda_n, Z_k}\| \cdot \|Z_k(\lambda_n)\| \tag{4.9}$$

thus implying

$$|\Delta\lambda_n|_{\max} \propto \|p_{\lambda_n, Z_k}\| \cdot \|Z_k(\lambda_n)\| \tag{4.10}$$

Equation (4.10) shows that $\|p_{\lambda_n, Z_k}\| \cdot \|Z_k(\lambda_n)\|$ establishes the upper limit of $|\Delta\lambda_n|$, denoted as $|\Delta\lambda_n|_{\max}$, which signifies the maximum possible contribution of the corresponding apparatus.

Apparatuses with larger $|\Delta\lambda_n|_{\max}$ are likely, but not guaranteed, to participate in the λ_n-mode. As a result, $\|p_{\lambda_n,Z_k}\|\cdot\|Z_k(\lambda_n)\|$ is used as the main participation index in *Stage-1* of the sampling strategy. This layer identifies potential participants in a mode with minimal prior information.

Sampling Stage-2

In this stage, we aim to pinpoint the specific control loop responsible for the instability within the participating apparatus located in Stage-1. This insight directs which parameter requires re-tuning and how to adjust it to restore stability. Continuing from (4.5), if $\Delta Z_k(\lambda_n)$ can be expressed as $\frac{\partial Z_k(\lambda_n)}{\partial \rho}\cdot\Delta\rho$, we have

$$\Delta\lambda_n = \underbrace{\langle p_{\lambda_n,Z_k}, \frac{\partial Z_k(\lambda_n)}{\partial \rho}\rangle}_{p_{\lambda,\rho}}\cdot\Delta\rho \tag{4.11}$$

where $\partial Z_k/\partial\rho$ signifies impedance sensitivity to its internal parameters. Hence, any slight change in the parameters first produces a corresponding change in impedance and, through the chain rule, ultimately causes a shift in the eigenvalues. This process generates parameter participation factors $p_{\lambda,\rho}$ that identify which internal parameters should be fine-tuned to steer a particular eigenvalue toward the desired position on the complex plane.

Sampling Stage-3

In this stage, we attempt to generate the 'critical' samples close to the stability boundary by iteratively solving the optimisation problem in *Stage-3*:

$$\min \parallel \zeta_m(\boldsymbol{\rho}_{l+1}) - \zeta_{\text{th}} \parallel \tag{4.12a}$$

$$\text{s.t. } \underline{\rho_j} \leq \rho_{j,l} + \Delta\rho_{j,l} \leq \bar{\rho_j} \quad \forall j \in J \tag{4.12b}$$

with $\boldsymbol{\rho}_{l+1} = \boldsymbol{\rho}_l + \boldsymbol{\Delta\rho}_l$ wherein the jth control parameter filtered by *Stage-2*, i.e. ρ_j, should remain within the typical range, which is $[\underline{\rho_j},\ \bar{\rho_j}]$ for all j. We denote $\boldsymbol{\rho}_l \in \mathbb{R}^J$ as a column vector comprising the identified control parameters from Stage-2 at the lth iteration. The current system's minimum damping ratio ζ_m of the critical eigenvalue λ_c, which serves as a small-signal stability indicator, is approximated by a first-order Taylor expansion centred at ζ_{m0}. This expansion is derived from the power system's operating point $\bar{\boldsymbol{x}}$ and the parameter $\boldsymbol{\rho}_l$ (with the iteration index l omitted here for clarity), as follows:

$$\zeta_m = \zeta_{m0} + \langle \boldsymbol{p}_{\zeta_m,\boldsymbol{\rho}}, \boldsymbol{\Delta\rho} \rangle = \zeta_{m0} + (\boldsymbol{p}_{\zeta_m,\boldsymbol{\rho}})^T \boldsymbol{\Delta\rho} \tag{4.13}$$

where $\boldsymbol{p}_{\zeta_m,\boldsymbol{\rho}} = f(\boldsymbol{p}_{\lambda_c,\boldsymbol{\rho}}) = [p_{\zeta_m,\rho_1}, p_{\zeta_m,\rho_2}, ..., p_{\zeta_m,\rho_J}] \in \mathbb{R}^J$. This mapping function $f(\cdot)$ is given by $\frac{-\text{Re}(\cdot)}{\sqrt{\text{Re}(\cdot)^2+\text{Im}(\cdot)^2}}$. Here $\langle \cdot, \cdot \rangle$ is the dot product of two vectors in a Euclidean space. If $\zeta_m > \zeta_{\text{th}}$, the system is small-signal stable and vice versa, where ζ_{th} is the threshold of system minimum

damping ratio, typically ranging from 5% to 8% [113]. The sample is on the stability boundary if $\zeta_m = \zeta_{\text{th}}$. Thus, the sample ultimately stops near the boundary through this iterative process.

Accordingly, the *Stage-3* problem can be written as a standard constrained quadratic program (QP) using a differential objective, which is shown succinctly as:

$$\min_{\boldsymbol{\Delta\rho}_l} f(\boldsymbol{\Delta\rho}_l) = \frac{1}{2} \parallel \zeta_m(\boldsymbol{\Delta\rho}_l) - \zeta_{\text{th}} \parallel^2 \tag{4.14a}$$

$$\text{s.t.} \quad \underline{\rho_j} \leq \rho_{j,l} + \Delta\rho_{j,l} \leq \bar{\rho_j} \qquad \forall j \in J \tag{4.14b}$$

where we introduce $\boldsymbol{\Delta\rho}_l \in \mathbb{R}^J$ as the decision variable and the next iteration is given by $\boldsymbol{\rho}_{l+1} = \boldsymbol{\rho}_l + \boldsymbol{\Delta\rho}_l$ until reaching the stop criteria, which will be described in the following subsection.

4.2.4 Sampling Strategy Description

The approach generates the initial dispatch result $\bar{\boldsymbol{x}}$ from AC-OPF without stability constraints with apparatus's parameters $\boldsymbol{\rho}_k$ at the current iteration. After the stability examination, as presented in Fig. 4.3, either unstable or stable OCs start the cycle of feature selection until it is terminated if triggering one of the following stop criteria, while dropping straight into the training database.

a. $k > N_{max}$

b. OC changes from ‘unstable’ to ‘stable’

c. No applicable selection of apparatus in *Stage-1*

d. No applicable selection of parameters in *Stage-2*

Note that N_{max} is the maximum number of iterations performed during the feature selection process. The pseudocode for the proposed sampling strategy is detailed in Algorithm 3. Discarding samples that do not meet the stop condition (b) gives a balanced training database, as the algorithm generates paired observations, i.e. one ‘stable’ and one ‘unstable’ ($\mathcal{U}_l$, $\mathcal{S}_{l+1}$) or ($\mathcal{S}_l$, $\mathcal{U}_{l+1}$), when provided with an OC.

In each sampling cycle, the system first identifies the critical eigenvalue λ_c with the minimum damping ratio. This eigenvalue is then sent to *Stage-1*, where the K dominant apparatus participants are selected by choosing those with the largest $|\Delta\lambda_c|_{\max}$ values. In *Stage-2*, candidate control parameters for each located apparatus are filtered using a preset threshold ρ_{th}. Finally, *Stage-3* employs an iterative approach, mimicking Newton’s method, to adjust these parameters until λ_c crosses the ζ_{th} threshold, indicating a change in system stability. Hence, retuning internal parameters iteratively can restabilise an unstable operating condition, thereby unlocking the stability-regulating potential of IBRs in system-level scheduling.

Algorithm 3: Sampling via Participation Analysis

Input : set product of unstable or stable operating conditions and the corresponding parameters $\mathcal{X} \times \varrho_0 = \{u_{1,0}, ..., u_{n,0}\} = \{(\bar{\boldsymbol{x}}_1, \boldsymbol{\rho}_0), ..., (\bar{\boldsymbol{x}}_n, \boldsymbol{\rho}_0)\}$, denoted by $\mathcal{U}_0$(unstable) (same for $\mathcal{S}_0$ (stable)), network impedance matrix $\boldsymbol{Y}_{net}$, all apparatus impedance matrix $\boldsymbol{Z}_m$

Output : $(\mathcal{U}_l, \mathcal{S}_{l+1})$ or $(\mathcal{S}_l, \mathcal{U}_{l+1})$

$l = 0$

for $\{u_{i,0}\}_{i=1,\cdots n} \in \mathcal{U}_0$ **do**

  while *all STOP criteria is not satisfied* **do**

    `/* Find the critical eigenvalue with the minimum damping ratio */`

    $\lambda_c \xleftarrow{\arg\min_{\lambda\in\Lambda}\zeta(\lambda)} \hat{\boldsymbol{Y}}_l \xleftarrow{(4.1)} (\bar{\boldsymbol{x}}_i, \boldsymbol{\rho}_l)$ $\quad \Lambda$ is the set of eigenvalues obtained from $\hat{\boldsymbol{Y}}_l$

    `/* Stage-1: Locate the apparatus with the` K `(user-defined) largest` $|\Delta\lambda_{c,k}|$`; ` $\mathcal{K}$ `is the index set of all candidate apparatus. */`

$$\mathcal{Z} = \left\{k \in K \ : \ |\Delta\lambda_{c,k}| \text{ is among the } n \text{ largest in } \{|\Delta\lambda_{c,j}| : j \in \mathcal{K}\}\right\}$$

    `/* Stage-2: Identify the primary internal parameters responsible for significant eigenvalue shifts;` $\mathcal{J}$ `is the index set of all candidate parameters. */`

$$\rho = \left\{j \in J \ : \ \Delta p_{\lambda_n,\rho_j} \text{ is among in } \{|\mathrm{Re}(\Delta p_{\lambda_n,\rho_j}|) > \rho_{\mathrm{th}} : j \in \mathcal{J}\}\right\}$$

    `/* Stage-3: Generate the 'critical' samples close to the stability boundary */`

$$\zeta_m = \zeta_{m0} + \langle \boldsymbol{p}_{\zeta_m,\boldsymbol{\rho}}, \boldsymbol{\Delta\rho}\rangle \leftarrow \boldsymbol{p}_{\zeta_m,\boldsymbol{\rho}} = f(\boldsymbol{p}_{\lambda_c,\boldsymbol{\rho}})$$

$$\boldsymbol{\rho}_{l+1} = \boldsymbol{\rho}_l + \boldsymbol{\Delta\rho}_l \leftarrow \text{Solve constrained QP (4.12)}$$

  end

$$\mathcal{U}^l \cup \{u_i^l\} \leftarrow u_i^l = (\bar{\boldsymbol{x}}_i, \boldsymbol{\rho}_l),\ \mathcal{S}^{l+1} \cup \{s_i^{l+1}\} \leftarrow s_i^{l+1} = (\bar{\boldsymbol{x}}_i, \boldsymbol{\rho}_{l+1})$$

  or

$$\mathcal{S}^l \cup \{s_i^l\} \leftarrow s_i^l = (\bar{\boldsymbol{x}}_i, \boldsymbol{\rho}_l),\ \mathcal{U}^{l+1} \cup \{u_i^{l+1}\} \leftarrow u_i^{l+1} = (\bar{\boldsymbol{x}}_i, \boldsymbol{\rho}_{l+1})$$

end

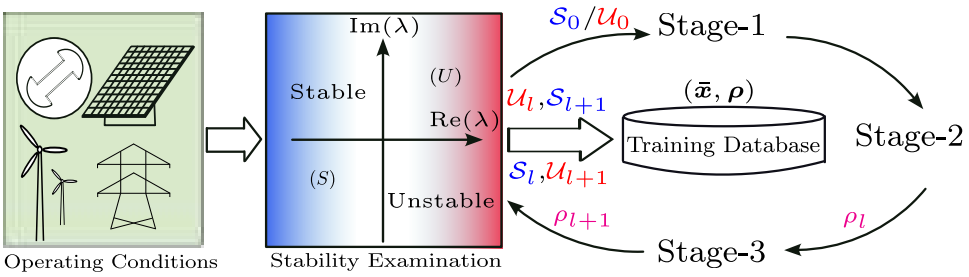

Figure 4.3: Sampling strategy framework.

4.2.5 Practical Implementation

This section details the practical application of the proposed sampling strategy. Prior to employing the method, four categories of data are necessary: the impedance Z_k, the system-wide admittance $\hat{Y}_{kk}$, the parameter vector $\boldsymbol{\rho}$, and the impedance Z_k again, specifically to compute the sensitivity $\partial Z_k/\partial\rho$ in *Stage-2*. All data are given in the frequency domain, i.e., as numerical spectra across a range of frequencies, enabling efficient computation without resorting to symbolic algebra and ensuring scalability for large systems [114].

Two main procedures can be used to acquire Z_k:

1) Model-Based Approach: This technique applies to cases where detailed analytical system models are available, typically from manufacturers. From these models, differential equations can be derived and linearised around an operating point to yield state-space representations. These state-space equations are then converted to transfer functions, substituting $s = j\omega$, to derive frequency responses. This route is used in this paper's case studies; the interested reader may consult [115] for code references.

2) Measurement-Based Approach: Suitable for both operators and manufacturers, this method involves injecting perturbation signals into the system and capturing the resulting frequency-domain outputs. By comparing inputs and outputs, impedance (or admittance) spectra are constructed. The input signal may be a pseudorandom waveform [116] or a frequency-swept signal [117], ensuring broad frequency excitation. Measurements can be taken via hardware testing or EMT (Electromagnetic Transient) simulations. Although this avoids manual derivation of equations, it is more time-intensive and can be affected by measurement noise.

Since Z_k is a function of the parameter ρ, its sensitivity is approximated numerically as:

$$\frac{\partial Z_k}{\partial \rho} \approx \frac{Z_{k,\Delta\rho} - Z_k}{\Delta\rho} \tag{4.15}$$

where $\Delta\rho$ is a small change in ρ, and $Z_{k,\Delta\rho}$ is the impedance under this perturbed condition. A recommended choice for the perturbation size is $\Delta\rho = 10^{-5}(1 + |\rho|)$ [112], balancing between relative and absolute perturbation effects. It is crucial that $Z_{k,\Delta\rho}$ accounts for changes in the system's equilibrium due to the perturbation, as these influence impedance during linearization.

Combining all Z_k components using equation (1) gives the system admittance $\hat{Y}_{kk}$. Poles and residues of $\hat{Y}_{kk}$ are then obtained via rational approximation techniques [118]. The primary computational load comes from matrix operations—particularly multiplication and inversion—which have a computational complexity of $O(N^3)$ or better with efficient algorithms [119].

This is similar to the computational burden of Newton-Raphson methods in steady-state power flow studies, making the sampling approach feasible for large networks.

It is also noteworthy that participation factors represent local sensitivities and are most accurate for small parameter changes. When broader parameter variation is necessary, repeated application of the sampling approach along the parameter path becomes essential. This iterative strategy is well-suited to continuous parameters, but less for discrete or logic-based ones. When poles are closely spaced or repeated, their residues may become indistinct, preventing direct analysis. In such cases, the poles can be temporarily treated as one and differentiated iteratively as parameters evolve.

While the sampling framework is tailored for small-signal analysis, it is highly complementary to EMT simulations when analysing large-signal behaviours. The sampling strategy provides interpretive insight into system dynamics, whereas EMT modelling captures full system nonlinearity, offering high-fidelity validation across a range of transient conditions.

4.3 Small-Signal Stability Constrained OPF

In the previous section, balanced stable-unstable samples are generated over a fixed time window T, i.e., $(\boldsymbol{z}, y) \in \mathcal{D}$. $\boldsymbol{z}$ represents a composed vector of static operation points and IBR control parameters; $y \in \{0, 1\}$ is the true label with 0 indicating a stable sample. Let $f(\cdot; \boldsymbol{\theta})$ be a

parametric stability assessor, its parameter $\boldsymbol{\theta}$ can be trained by the binary cross entropy loss (BCE) [120], e.g.,

$$\min_{\boldsymbol{\theta}} \mathcal{L}^{BCE}(\boldsymbol{\theta}) := \frac{1}{T}\sum_{t=1}^{T} y_t \cdot \log \sigma(\hat{y}_t) + (1-y_t)\cdot \log(1-\sigma(\hat{y}_t)) \tag{4.16}$$

where $\sigma(\cdot)$ is the sigmoid function and $\hat{y}_t = f(\boldsymbol{z}_t;\boldsymbol{\theta})$. Moreover, to ensure that all unstable samples are accurately identified, large penalisations can be amended for unstable samples [63, 120]. A constrained BCE (CBCE) loss is formulated as,

$$\begin{aligned} &\min_{\boldsymbol{\theta}} \mathcal{L}^{CBCE}(\boldsymbol{\theta}) := \frac{1}{T}\sum_{t\in\mathcal{D}_0} \log(1+\exp(f(z_t;\boldsymbol{\theta}))) \\ &\text{s.t. } f(z_t;\boldsymbol{\theta}) \geq 0, z_t \in \mathcal{D}_1 \end{aligned} \tag{4.17}$$

where $\mathcal{D}_0$ and $\mathcal{D}_1$ are stable and unstable index sets. The hard constraint on $\mathcal{D}_1$ ensures that all unstable samples are accurately classified.

Once $f(\cdot;\boldsymbol{\theta}^\star)$ is trained, it can be encoded into existing real-time OPF models [121], resulting in the following compact formulation,

$$\min_{\boldsymbol{z}} \; g(\boldsymbol{z}) \quad \text{s.t. } h(\boldsymbol{z};\boldsymbol{\xi}) \leq \mathbf{0},\; f(\boldsymbol{z};\boldsymbol{\theta}^\star) \leq -\tau \tag{4.18}$$

where $g(\cdot)$ is the OPF objective; $\boldsymbol{h}(\cdot)$ is the conventional OPF constraints; $\boldsymbol{\xi}$ are optimization parameters, such as real-time load and wind profiles. A confidence parameter $\tau \geq 0$ is added

to control the conservativity of the stability constraints. Moreover, to ensure that the stability constraint does not significantly increase the real-time computation overhead, a linear regression model, e.g., $\hat{y}_t = \boldsymbol{w}^T \boldsymbol{z}_t + b$ is adopted in the case study.

4.4 Case Study

This section presents several case studies on a modified IEEE 14-bus power system to illustrate the interplay between system-level analysis and device-level control. We highlight the effectiveness of the proposed participation-based sampling method and the economic advantages of leveraging IBR capacity to support small-signal stability within our data-driven OPF framework. Two models are employed: (1) a whole-system impedance model derived from detailed analytical representations using dynamic differential equations, and (2) an explicit data-driven SSSC AC-OPF model that generates the optimal system dispatch. Finally, the full dynamic model is used to re-assess system stability through eigenvalue analysis and Electromagnetic Transient (EMT) simulation.

The composite power system under test comprises IBRs in the form of Type-IV wind farms, representing an aggregation of several identical IBRs with the same operating conditions, as shown in Fig. 4.4. In this configuration, the SG on bus 6 operates in GFM mode, while GFLs replace SGs on buses 3 and 8. All SGs are parametrised per the settings in [122] with the

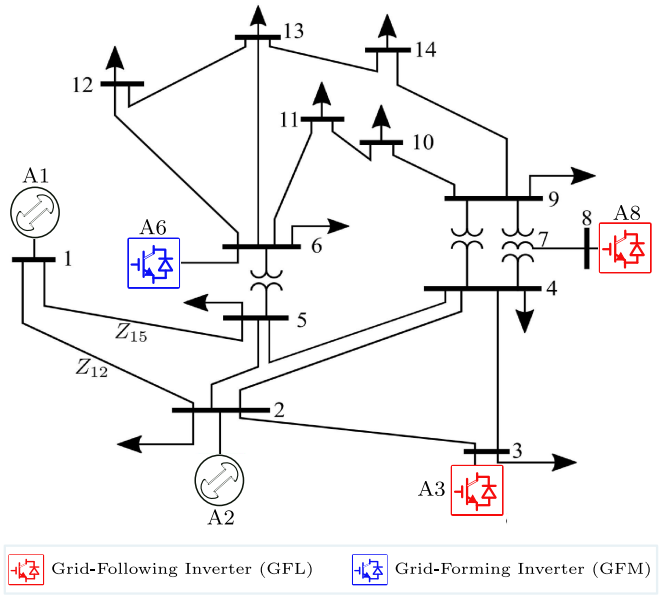

Figure 4.4: Modified IEEE 14-bus test system.

generation cost data in [99]. Comprehensive system data, simulation codes, and numerical results are available at `https://github.com/Future-Power-Networks/Publications` [115]. Wind and load data for the test system are adopted from [123]. The optimization problem was formulated in MATLAB using the YALMIP modeling layer [103] and solved with MATLAB's fmincon from the Optimization Toolbox under its default settings. All simulations were performed on a standard laptop equipped with an AMD Ryzen 7 5800H CPU (3.20 GHz) and 16 GB of RAM.

4.4.1 Performance of the Proposed Sampling Strategy

Prior to illustrating our proposed sampling strategy, we perform a modal analysis to intentionally detune the IBRs' control parameters, thereby increasing the system's susceptibility to oscillations. The whole-system admittance determined by (4.1) is plotted as the Bode diagram

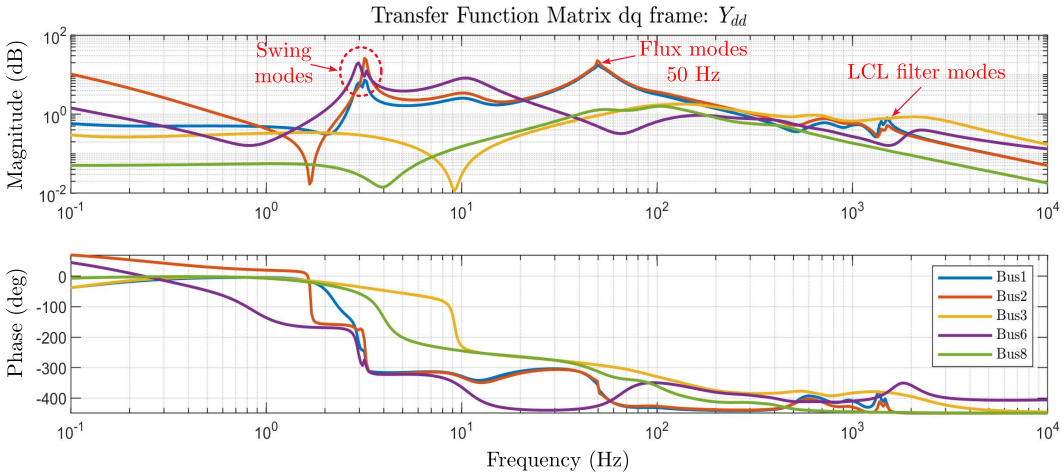

Figure 4.5: Bode diagram of whole system admittance $\hat{Y}_{kk}$ at apparatus bus in *dd* axis.

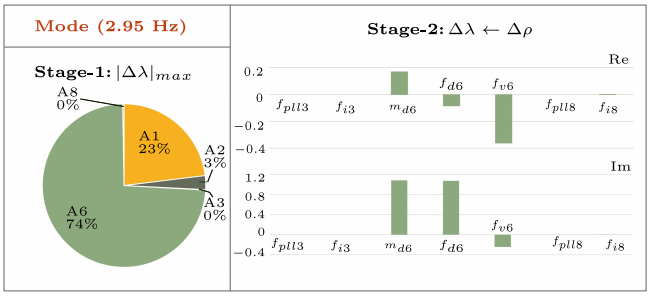

Figure 4.6: Participation analysis of the critical under-damped mode in Stage-1 and Stage-2 of the sampling strategy, where the results in Stage-2 are normalised to the base value.

in Fig. 4.5. Note that it is the Bode diagram of $\hat{Y}_{dd}$ as one of the four elements in 2×2 matrix $\hat{Y}_{kk}$ in *dq* frame. Several resonant peaks are visible in the plot, each corresponding to a different oscillatory mode. For instance, the 50 Hz mode, resulting from flux dynamics in windings and lines [112], is a standard feature, while modes around 1-2 Hz reflect swing behaviors and a high-frequency mode is associated with the LCL filter of the GFM. With deliberately detuning m_d and f_d by -30% and -66% respectively, the swing mode marked in Fig. 4.5 has become undamped to demonstrate the sampling process.

Following the algorithm 3, the critical eigenvalue has been pinpointed at the swing mode (2.95 Hz). Fig. 4.6 showcases the results of conducting *Stage-1* and *Stage-2* in the proposed sampling

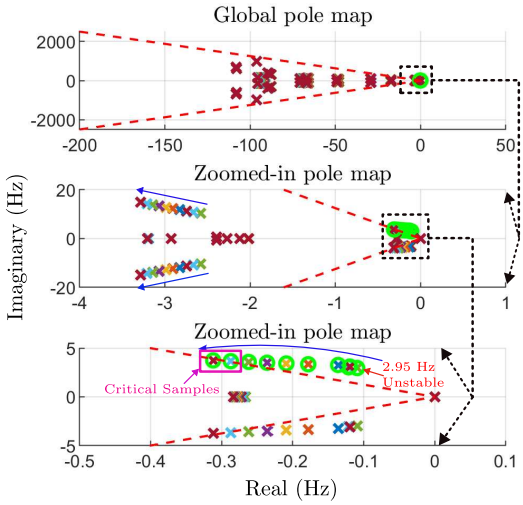

(a) System pole loci illustrating the trajectory of the critical mode in the sampling cycle.

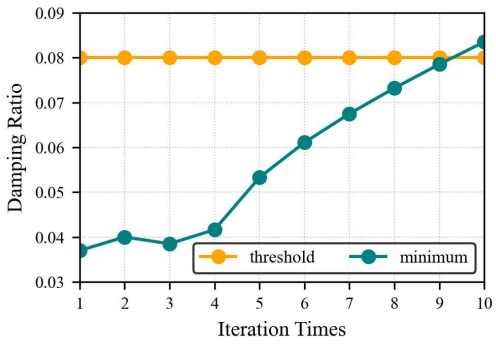

(b) Evolution of the system's minimum damping ratio in the sampling process.

Figure 4.7: Overall stability observation during sampling.

process. A6 among all three IBRs stands out in the first stage as the dominant apparatus, which yields the parameter candidates in *Stage-2*, i.e. m_{d6}, f_{d6} and f_{v6}. To validate our strategy, we are not only looking into the participating apparatus in *Stage-1* but figuring out the participation factors $p_{\lambda,\rho}$ regarding all parameter candidates in Fig. 4.6. We have to calculate the normalised participation factors $\bar{p}_{\lambda,\rho}$ by rewriting (4.11) as

$$\Delta\lambda_c = \underbrace{\langle p_{\lambda_c,Z_k}, \frac{\partial Z_k(\lambda_c)}{\partial \rho} \cdot \rho_{\text{base}} \rangle}_{\bar{p}_{\lambda,\rho}} \cdot \frac{\Delta\rho}{\rho_{base}}. \tag{4.19}$$

Using the chain rule in (4.19), we compute the $\bar{p}_{\lambda,\rho}$ for the critical mode to the internal parameters of A3, A6, and A8. These values are shown in the right-column chart of Fig. 4.6. The numerical results confirm the findings from *Stage-1*: the candidate parameters of A6 induce a larger critical eigenvalue perturbation, with $\bar{p}_{\lambda,\rho}$ exhibiting greater real and imaginary components compared to those of the other IBR control parameters.

Fig. 4.7a illustrates the evolution of the critical system mode at 2.95 Hz and the corresponding damping ratio as the sampling process proceeds. In Fig. 4.7a, the Global pole map plots the system poles on the complex plane, while the lower panels, the zoomed-in pole map, provide magnified views of the critical region near the stability boundary. The critical mode, initially exhibiting a damping ratio below the threshold, moves gradually toward and ultimately crosses the stability boundary, i.e. $\zeta_m = \zeta_{\text{th}}$, as the sampling iteration advances. Once the mode's damping ratio exceeds the threshold, i.e. the system is deemed stable.

Fig. 4.7b tracks the progression of the minimum damping ratio ζ_m across successive iterations, with the horizontal line representing the threshold, that is $\zeta_{\text{th}} = 8\%$. The curve demonstrates how the system's minimum damping ratio transitions from an unstable state to a stable one through repeated sampling. This process highlights the proposed sampling strategy, wherein 'critical' samples—those operating close to the stability boundary—are selected and included in the training database. By incorporating these boundary cases, the training set is enriched with instances that are most informative for improving the accuracy and robustness of subsequent

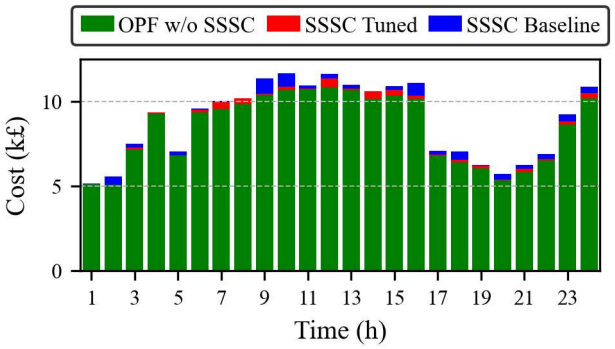

Figure 4.8: Comparison of the generation costs under one selected day for three OPF scenarios stability analyses.

4.4.2 Performance of the Small-Signal Stability Constrained OPF

To demonstrate the effectiveness and economic benefits of the proposed small-signal stability OPF model with dynamic IBR parameter optimization, three OPF scenarios are compared based on generation cost:

a. *OPF w/o SSSC:* OPF without SSSC.

b. *SSSC-OPF baseline:* SSSC-OPF parameter tuning disabled, serving as the baseline through the SGs' active power and voltage rescheduling process.

c. *SSSC-OPF tuned:* SSSC-OPF with parameter tuning enabled.

The overall system costs for the three cases were compared over the selected 24 hours in Fig 4.8. From the chart, the *OPF w/o SSSC* scenario consistently yields the lowest cost. In contrast, the *SSSC Baseline* approach incurs the highest cost because it relies on rescheduling

generators to address small-signal stability issues after the initial dispatch. Interestingly, the *SSSC Tuned* scenario matches the *OPF w/o SSSC* costs for many time intervals. This indicates that dynamically optimising IBR parameters can resolve instability without requiring any level of rescheduling. However, at certain hours, the *SSSC Tuned* bars rise above the *OPF w/o SSSC* bars, suggesting that additional constraints—most notably voltage magnitude constraints of the apparatus bus—become active and require some degree of rescheduling, thus increasing the overall cost. Overall, the results suggest that while dynamic parameter optimisation is highly effective in maintaining stability without additional cost, there are moments when system limitations, i.e. voltage constraints, force a trade-off between stability and cost efficiency.

The proposed two-stage feature selection method enhances scalability by hierarchically narrowing the scope of analysis. In *Stage-1*, key apparatus is identified based on its dominant contribution to system-wide stability margins. In *Stage-2*, parameter-level participation factors are calculated only for these selected apparatus and used to identify stability-relevant control parameters. This structured approach ensures that only a limited subset of features is retained for model training, reducing dimensionality and computational load, even in large-scale systems.

Chapter 5

Conclusions and Future Work

This chapter summarizes the thesis and explores potential future directions to further advance the research.

5.1 Summary and Conclusion

This thesis has demonstrated that data-driven approaches and optimization frameworks can significantly improve the stability and efficiency of power systems with high IBR penetration. The key findings include:

a. The development of an adaptive droop control strategy that dynamically adjusts wind turbine support based on system conditions, reducing frequency deviations.

b. The implementation of a participation-based sampling strategy that efficiently identifies critical stability boundaries, improving the robustness of optimization models.

c. The successful application of data-driven small-signal stability constraints in OPF formulations to enhance system security.

d. A data-driven approach to integrating parameters of IBRs as decision variables in system scheduling, ensuring small-signal stability while maintaining economic efficiency.

e. The validation of proposed methodologies through detailed simulations and case studies, highlighting their effectiveness in practical power system operations.

While this research has provided a solid foundation for enhancing power system stability through SDPS, several areas remain open for further exploration.

5.2 Future Work

Several areas can be explored to further enhance the research in this thesis. The key directions are outlined as follows.

- Advanced Probabilistic Forecasting for Synthetic Inertia: Future work should focus on developing probabilistic forecasting models that incorporate real-time wind speed variations, wake effects, and regional characteristics to improve accuracy and reliability.

- Optimal Allocation of Synthetic Inertia at the Wind Farm Level: While the current research determines aggregated synthetic inertia provision per wind farm, an open question remains on how best to allocate this inertia among individual wind turbines. Future studies could explore model predictive control techniques for real-time optimization, ensuring minimal wind energy loss while meeting system stability requirements.

- Locational Frequency Considerations in Low-Inertia Systems: Traditional power system models assume uniform frequency behaviour based on the Center-of-Inertia (CoI) approximation. However, in low-inertia systems, frequency deviations at different nodes can vary significantly. Future work should investigate nodal frequency dynamics and incorporate them into system-wide scheduling models to enhance accuracy and resilience.

- Short Circuit Contribution Modelling for inverter-based generation (IBG) Systems: In this thesis, IBG is modelled as constant current sources during faults. However, IBGs often behave as voltage-dependent current sources, especially when the electrical distance from the fault is significant. Future studies should refine these models to predict better IBG responses under different fault conditions, including unbalanced faults.

- Transient Voltage Stability during Faults: Future research should explore how IBGs can provide low-voltage ride-through (LVRT) capabilities and dynamic reactive power support to mitigate transient voltage instabilities.

- Impedance-Based Optimization Framework: Stability indices such as voltage stability,

synchronization stability, and rotor angle stability are all closely tied to system impedance. A unified impedance-based optimization framework could be developed to assess grid security holistically, allowing operators to optimize system stability and efficiency more effectively.

- Integration of Stability Constraints into Electricity Market Mechanisms: The deployment of frequency and voltage stability measures needs to be aligned with electricity market designs. Future studies should explore market-based approaches that incentivize IBGs to provide stability services while ensuring economic efficiency.

- Machine Learning for Stability-Constrained Scheduling: Leveraging AI and machine learning, future work could develop more adaptive scheduling mechanisms that predict stability constraints in real time. This could improve decision-making processes by reducing computational burden while maintaining high accuracy.

- Real-World Deployment and Validation: The proposed strategies must be tested in large-scale, real-world power systems. Collaborations with grid operators and industry stakeholders will be essential for validating theoretical findings and implementing pilot projects to assess real-time performance.

- Dynamic Optimization of Inverter-Based Grid Support: Future research should investigate how inverter-based resources can dynamically adjust their control strategies to provide optimal grid support in response to real-time operating conditions.

- Cyber-Physical Security in SDPS: As SDPS increasingly relies on digital control and data-driven decision-making, cybersecurity concerns must be addressed. Future work should explore how to develop resilient architectures to protect against cyber threats and ensure robust power system operations.

- Integration of Hybrid Energy Storage Systems: Investigating the potential of hybrid energy storage solutions, such as combinations of batteries and supercapacitors, to enhance grid stability and provide faster frequency response services.

By advancing these research areas, the principles outlined in this thesis can contribute to the development of resilient, flexible, and cost-effective power grids capable of supporting a sustainable energy future. These advancements will not only improve power system operations but also pave the way for a more adaptive and intelligent grid that efficiently integrates high levels of renewable energy sources.

Appendix A

Supplementary Material for Efficient Sampling for Data-Driven Frequency Stability Constraint via Forward-Mode Automatic Differentiation

A.1 Derivation of $\dot{\omega}(t = 0^+)$ in (2.5)

For the case of $K = 0$, let $M = M_0$ and $q = \omega = 0$ in (2.1a), it can be obtained that $\dot{\omega}(t = 0^+) = \frac{\Delta P}{M_0}$. For the case of $K \neq 0$, plugging (2.4) into (2.1a), it gives

$$K_{12}\dot{\omega}^2 - M_0\dot{\omega} + \Delta P = 0 \tag{A.1}$$

in which $\dot{\omega}$ can be solved as

$$\dot{w} = \frac{g(K_{12})}{h(K_{12})} \tag{A.2}$$

with $g(K_{12}) = M_0 \pm \sqrt{M_0^2 - 4K_{12}\Delta P}$ and $h(K_{12}) = 2K_{12}$.

Since $\lim_{K_2 \to 0} g(K_2) = \lim_{K_2 \to 0} h(K_2) = 0$, the L'Hopital's rule gives that

$$\lim_{K_2 \to 0} \frac{g(K_{12})}{h(K_{12})} = \lim_{K_2 \to 0} \frac{g'(K_{12})}{h'(K_{12})} = \pm \left(-\frac{\Delta P}{M_0} \right) \tag{A.3}$$

Therefore, only the minus sign is feasible when $K_2 \to 0$.

A.2 Derivation of the Augmented ODE (2.8b)

Starting from the (2.7), the time domain solution can be written as

$$x(t_1) = x_0 + \int_{t=0}^{t_1} f(x(t), \theta) dt \tag{A.4}$$

Do partial derivative on θ on each side,

$$\frac{\partial x(t_1)}{\partial \theta} = \frac{\partial x_0}{\partial \theta} + \int_{t=0}^{t_1} \frac{\partial f}{\partial x}\frac{\partial x}{\partial \theta} + \frac{\partial f}{\partial \theta} dt \tag{A.5}$$

Multiply the unit vector e_i on each side,

$$\underbrace{\frac{\partial x(t_1)}{\partial \theta} e_i}_{\hat{x}_i(t_1)} = \underbrace{\frac{\partial x_0}{\partial \theta} e_i}_{\hat{x}_i(t=0^+)} + \int_{t=0}^{t_1} \frac{\partial f}{\partial x} \underbrace{\frac{\partial x}{\partial \theta} e_i}_{\hat{x}_i(t)} + \frac{\partial f}{\partial \theta} e_i dt \tag{A.6}$$

which can be considered as the solution of the following ODE

$$\frac{d\hat{x}_i(t)}{dt} = \frac{\partial f}{\partial x}\hat{x}_i(t) + \frac{\partial f}{\partial \theta} e_i, \quad \hat{x}_i(t=0^+) = \frac{\partial x_0}{\partial \theta} e_i \tag{A.7}$$

For $i = 1, 3, 4$, $\frac{\partial x_0}{\partial \theta} e_i = 0$. For $i = 2$, referring to (2.6), $\frac{\partial x_0}{\partial \theta} e_2 = \left[0, \frac{\partial \dot{\omega}(t=0^+)}{\partial K_{12}}\right]^T$.

A.3 Baseline Methods

A.3.1 Unrolling Differentiation

The Euler's method for ODE can be viewed as a function whose input is the ODE's initial values and parameters. This function is composed of elementary operations whose derivatives are known. Therefore, if all steps of the computations over T are recorded on the computational

graph, a direct call to the automatic differentiation package such as `PyTorch` can be used to find the gradients. To perform the parallel computation, `torch.func.vmap` is implemented.

A.3.2 Finite Difference

Let e_i be the i-th unit vector whose entry i equals 1 and the remaining equals 0. Let $x(t', \theta)$ be the solution to (2.7) at time t with parameter θ. Define $\theta_{pi} = \theta + \epsilon \cdot e_i$ as the perturbed version of θ and the associated solution at time t' is $x(t', \theta_{pi})$. ϵ is a small number. The gradient with respect to θ_i is approximated as

$$\frac{\partial x(t', \theta)}{\partial \theta_i} \approx \frac{x(t', \theta_{pi}) - x(t', \theta)}{\epsilon} \tag{A.8}$$

Bibliography

[1] "EU Climate Action Progress Report 2023," European Commission, Report, 2023.

[2] "UK Net Zero Strategy: Progress Report 2023," UK Department for Business, Report, 2023.

[3] "China's Carbon Neutrality Roadmap," Ministry of Ecology and Environment of the People's Republic of China, Report, 2023.

[4] "World Energy Outlook 2023," International Energy Agency, Report, 2023.

[5] "Renewable Capacity Statistics 2023," International Renewable Energy Agency, Report, 2023.

[6] "Technical Report on Renewable Integration Challenges and Strategies," International Renewable Energy Agency, Report, 2023.

[7] "Grid Integration of Renewable Energy: Challenges and Opportunities in Modern Grids," National Renewable Energy Laboratory, Report, 2023.

[8] M. Dreidy, H. Mokhlis, and S. Mekhilef, "Inertia response and frequency control techniques for renewable energy sources: A review," *Renewable and Sustainable Energy Reviews*, vol. 69, pp. 144–155, 2017.

[9] E. Muljadi, V. Gevorgian, M. Singh, and S. Santoso, *Understanding inertial and frequency response of wind power plants*. IEEE, 2012.

[10] Z. Wu, W. Gao, T. Gao, W. Yan, H. Zhang, S. Yan, and X. Wang, "State-of-the-art review on frequency response of wind power plants in power systems," *Journal of Modern Power Systems and Clean Energy*, vol. 6, no. 1, pp. 1–16, 2018.

[11] K. Liu, Y. Qu, H.-M. Kim, and H. Song, "Avoiding frequency second dip in power unreserved control during wind power rotational speed recovery," *IEEE Transactions on Power Systems*, vol. 33, no. 3, pp. 3097–3106, 2017.

[12] Z. Chu, U. Markovic, G. Hug, and F. Teng, "Towards optimal system scheduling with synthetic inertia provision from wind turbines," *IEEE Transactions on Power Systems*, vol. 35, no. 5, pp. 4056–4066, 2020.

[13] J. Lee, G. Jang, E. Muljadi, F. Blaabjerg, Z. Chen, and Y. C. Kang, "Stable short-term frequency support using adaptive gains for a DFIG-based wind power plant," *IEEE Transactions on Energy Conversion*, vol. 31, no. 3, pp. 1068–1079, 2016.

[14] A. Attya, J. L. Dominguez-Garcia, and O. Anaya-Lara, "A review on frequency support provision by wind power plants: Current and future challenges," *Renewable and Sustainable Energy Reviews*, vol. 81, pp. 2071–2087, 2018.

[15] G. Xu and L. Xu, "Improved use of wt kinetic energy for system frequency support," *IET renewable power generation*, vol. 11, no. 8, pp. 1094–1100, 2017.

[16] D. Yang, M. Kang, E. Muljadi, W. Gao, J. Hong, J. Choi, and Y. C. Kang, "Short-term frequency response of a dfig-based wind turbine generator for rapid frequency stabilization," *Energies*, vol. 10, no. 11, p. 1863, 2017.

[17] M. Kheshti, S. Lin, X. Zhao, L. Ding, M. Yin, and V. Terzija, "Gaussian distribution-based inertial control of wind turbine generators for fast frequency response in low inertia systems," *IEEE Transactions on Sustainable Energy*, vol. 13, no. 3, pp. 1641–1653, 2022.

[18] J. Lee, E. Muljadi, P. Srensen, and Y. C. Kang, "Releasable kinetic energy-based inertial control of a DFIG wind power plant," *IEEE Transactions on Sustainable Energy*, vol. 7, no. 1, pp. 279–288, 2015.

[19] Y. Gu and T. C. Green, "Power system stability with a high penetration of inverter-based resources," *Proceedings of the IEEE*, 2022.

[20] B. R. Naidu, P. Bajpai, and C. Chakraborty, "Voltage fault ride-through operation of solar pv units: A review and way forward," in *2019 8th International Conference on*

Power Systems (ICPS), 2019, pp. 1–6.

[21] Q. Hu, L. Fu, F. Ma, and F. Ji, "Large signal synchronizing instability of pll-based vsc connected to weak ac grid," *IEEE Transactions on Power Systems*, vol. 34, no. 4, pp. 3220–3229, 2019.

[22] Y. Gu, Y. Li, Y. Zhu, and T. C. Green, "Impedance-based whole-system modeling for a composite grid via embedding of frame dynamics," *IEEE Transactions on Power Systems*, vol. 36, no. 1, pp. 336–345, 2020.

[23] W. Dong, H. Xin, D. Wu, and L. Huang, "Small signal stability analysis of multi-infeed power electronic systems based on grid strength assessment," *IEEE transactions on Power Systems*, vol. 34, no. 2, pp. 1393–1403, 2018.

[24] T. Weckesser, H. Jóhannsson, and J. Østergaard, "Real-time remedial action against aperiodic small signal rotor angle instability," *IEEE Transactions on Power Systems*, vol. 31, no. 1, pp. 387–396, 2015.

[25] U. Markovic, Z. Chu, P. Aristidou, and G. Hug, "Lqr-based adaptive virtual synchronous machine for power systems with high inverter penetration," *IEEE Transactions on Sustainable Energy*, vol. 10, no. 3, pp. 1501–1512, 2018.

[26] R. Zárate-Miñano, F. Milano, and A. J. Conejo, "An opf methodology to ensure small-signal stability," *IEEE Transactions on Power Systems*, vol. 26, no. 3, pp. 1050–1061,

2010.

[27] J. Condren and T. W. Gedra, "Expected-security-cost optimal power flow with small-signal stability constraints," *IEEE Transactions on Power Systems*, vol. 21, no. 4, pp. 1736–1743, 2006.

[28] H.-K. Nam, Y.-K. Kim, K.-S. Shim, and K. Y. Lee, "A new eigen-sensitivity theory of augmented matrix and its applications to power system stability analysis," *IEEE Transactions on Power Systems*, vol. 15, no. 1, pp. 363–369, 2000.

[29] S. K. Kodsi and C. A. Canizares, "Application of a stability-constrained optimal power flow to tuning of oscillation controls in competitive electricity markets," *IEEE Transactions on Power Systems*, vol. 22, no. 4, pp. 1944–1954, 2007.

[30] Y. Yang, J. Zhao, H. Liu, Z. Qin, J. Deng, and J. Qi, "A matrix-perturbation-theory-based optimal strategy for small-signal stability analysis of large-scale power grid," *Protection and Control of Modern Power Systems*, vol. 3, pp. 1–11, 2018.

[31] P. Li, H. Wei, B. Li, and Y. Yang, "Eigenvalue-optimisation-based optimal power flow with small-signal stability constraints," *IET Generation, Transmission & Distribution*, vol. 7, no. 5, pp. 440–450, 2013.

[32] P. Pareek and H. D. Nguyen, "A convexification approach for small-signal stability constrained optimal power flow," *IEEE Transactions on Control of Network Systems*, vol. 8,

no. 4, pp. 1930–1941, 2021.

[33] D. Pullaguram, R. Madani, T. Altun, and A. Davoudi, "Small-signal stability-constrained optimal power flow for inverter dominant autonomous microgrids," *IEEE Transactions on Industrial Electronics*, vol. 69, no. 7, pp. 7318–7328, 2021.

[34] P. Pareek, K. Turitsyn, K. Dvijotham, and H. D. Nguyen, "A sufficient condition for small-signal stability and construction of robust stability region," in *2019 IEEE Power & Energy Society General Meeting (PESGM)*. IEEE, 2019, pp. 1–5.

[35] J. Liu, Z. Yang, J. Zhao, J. Yu, B. Tan, and W. Li, "Explicit data-driven small-signal stability constrained optimal power flow," *IEEE Transactions on Power Systems*, vol. 37, no. 5, pp. 3726–3737, 2021.

[36] Q. Chen, L. Badesa, Z. Chu, and G. Strbac, "Adaptive droop gain control for optimal kinetic energy extraction from wind turbines to support system frequency," *IEEE Access*, 2024.

[37] M. Netto, Y. Susuki, and L. Mili, "Data-driven participation factors for nonlinear systems based on koopman mode decomposition," *IEEE control systems letters*, vol. 3, no. 1, pp. 198–203, 2018.

[38] H. Abdelraouf, F. Albalawi, and E. Feron, "On linear time invariant systems analysis via a single trajectory: A linear programming approach," in *2022 IEEE Conference on*

Control Technology and Applications (CCTA). IEEE, 2022, pp. 989–994.

[39] D. Rodales, A. Zamora-Mendez, J. A. de la O Serna, J. M. Ramirez, M. R. A. Paternina, L. Lugnani, G. E. Mejia-Ruiz, A. Sanchez-Ocampo, and D. Dotta, "Model-free inertia estimation in bulk power grids through o-splines," *International Journal of Electrical Power & Energy Systems*, vol. 153, p. 109323, 2023.

[40] L. Huang, J. Coulson, J. Lygeros, and F. Dörfler, "Decentralized data-enabled predictive control for power system oscillation damping," *IEEE Transactions on Control Systems Technology*, vol. 30, no. 3, pp. 1065–1077, 2021.

[41] J. Hu, Q. Wang, Y. Ye, and Y. Tang, "Toward online power system model identification: A deep reinforcement learning approach," *IEEE Transactions on Power Systems*, vol. 38, no. 3, pp. 2580–2593, 2022.

[42] J. Stiasny, S. Chevalier, R. Nellikkath, B. Sævarsson, and S. Chatzivasileiadis, "Closing the loop: A framework for trustworthy machine learning in power systems," https://arxiv.org/abs/2203.07505, 2022, presented at 11th Bulk Power Systems Dynamics and Control Symposium (IREP), Banff, Canada, 2022.

[43] C. Ren and Y. Xu, "A fully data-driven method based on generative adversarial networks for power system dynamic security assessment with missing data," *IEEE Transactions on Power Systems*, vol. 34, no. 6, pp. 5044–5052, 2019.

[44] C. Hamon, M. Perninge, and L. Söder, "An importance sampling technique for probabilistic security assessment in power systems with large amounts of wind power," *Electric Power Systems Research*, vol. 131, pp. 11–18, 2016.

[45] V. Krishnan, J. D. McCalley, S. Henry, and S. Issad, "Efficient database generation for decision tree based power system security assessment," *IEEE Transactions on Power systems*, vol. 26, no. 4, pp. 2319–2327, 2011.

[46] Y. Xu, Z. Y. Dong, J. H. Zhao, P. Zhang, and K. P. Wong, "A reliable intelligent system for real-time dynamic security assessment of power systems," *IEEE Transactions on Power Systems*, vol. 27, no. 3, pp. 1253–1263, 2012.

[47] F. Capitanescu, M. Glavic, D. Ernst, and L. Wehenkel, "Contingency filtering techniques for preventive security-constrained optimal power flow," *IEEE Transactions on Power Systems*, vol. 22, no. 4, pp. 1690–1697, 2007.

[48] J. L. Cremer, I. Konstantelos, and G. Strbac, "From optimization-based machine learning to interpretable security rules for operation," *IEEE Transactions on Power Systems*, vol. 34, no. 5, pp. 3826–3836, 2019.

[49] N. Hatziargyriou, J. Milanovic, C. Rahmann, V. Ajjarapu, C. Canizares, I. Erlich, D. Hill, I. Hiskens, I. Kamwa, B. Pal, P. Pourbeik, J. Sanchez-Gasca, A. Stankovic, T. Van Cutsem, V. Vittal, and C. Vournas, "Definition and classification of power system stability

– revisited amp; extended," *IEEE Transactions on Power Systems*, vol. 36, no. 4, pp. 3271–3281, 2021.

[50] J. Gao, B. Chaudhuri, and A. Astolfi, "Lyapunov-based transient stability analysis," in *2022 IEEE 61st Conference on Decision and Control (CDC)*, 2022, pp. 5099–5104.

[51] Z. Chu, S. Lakshminarayana, B. Chaudhuri, and F. Teng, "Mitigating load-altering attacks against power grids using cyber-resilient economic dispatch," *IEEE Transactions on Smart Grid*, vol. 14, no. 4, pp. 3164–3175, 2023.

[52] P. Li, J. Qi, J. Wang, H. Wei, X. Bai, and F. Qiu, "An sqp method combined with gradient sampling for small-signal stability constrained opf," *IEEE Transactions on Power Systems*, vol. 32, no. 3, pp. 2372–2381, 2017.

[53] L. Badesa, F. Teng, and G. Strbac, "Simultaneous scheduling of multiple frequency services in stochastic unit commitment," *IEEE Transactions on Power Systems*, vol. 34, no. 5, pp. 3858–3868, 2019.

[54] Z. Zhang, E. Du, F. Teng, N. Zhang, and C. Kang, "Modeling frequency dynamics in unit commitment with a high share of renewable energy," *IEEE Transactions on Power Systems*, vol. 35, no. 6, pp. 4383–4395, 2020.

[55] F. Bellizio, W. Xu, D. Qiu, Y. Ye, D. Papadaskalopoulos, J. L. Cremer, F. Teng, and G. Strbac, "Transition to digitalized paradigms for security control and decentralized

electricity market," *Proceedings of the IEEE*, vol. 111, no. 7, pp. 744–761, 2023.

[56] N. Zhang, H. Jia, Q. Hou, Z. Zhang, T. Xia, X. Cai, and J. Wang, "Data-driven security and stability rule in high renewable penetrated power system operation," *Proceedings of the IEEE*, vol. 111, no. 7, pp. 788–805, 2023.

[57] J. L. Cremer, I. Konstantelos, and G. Strbac, "Optimized operation rules for imbalanced classes," in *2019 IEEE Power & Energy Society General Meeting (PESGM)*. IEEE, 2019, pp. 1–5.

[58] Z. Li, Z. Chu, and F. Teng, "Optimal design of neural network structure for power system frequency security constraints," in *12th International Conference on Renewable Power Generation (RPG 2023)*, vol. 2023, 2023, pp. 230–236.

[59] U. Markovic, Z. Chu, P. Aristidou, and G. Hug, "Fast frequency control scheme through adaptive virtual inertia emulation," in *2018 IEEE Innovative Smart Grid Technologies - Asia (ISGT Asia)*, 2018, pp. 787–792.

[60] H. Saadat *et al.*, *Power system analysis*. McGraw-hill, 1999, vol. 2.

[61] Q. Shi, F. Li, and H. Cui, "Analytical method to aggregate multi-machine sfr model with applications in power system dynamic studies," *IEEE Transactions on Power Systems*, vol. 33, no. 6, pp. 6355–6367, 2018.

[62] U. Markovic, Z. Chu, P. Aristidou, and G. Hug, "Lqr-based adaptive virtual synchronous machine for power systems with high inverter penetration," *IEEE Transactions on Sustainable Energy*, vol. 10, no. 3, pp. 1501–1512, 2019.

[63] G. Cui, Z. Chu, and F. Teng, "Control-mode as a grid service in software-defined power grids: Gfl vs gfm," *IEEE Transactions on Power Systems*, pp. 1–13, 2024.

[64] T. Yu, S. Kumar, A. Gupta, S. Levine, K. Hausman, and C. Finn, "Gradient surgery for multi-task learning," *Advances in Neural Information Processing Systems*, vol. 33, pp. 5824–5836, 2020.

[65] A. G. Baydin, B. A. Pearlmutter, A. A. Radul, and J. M. Siskind, "Automatic differentiation in machine learning: a survey," *Journal of machine learning research*, vol. 18, no. 153, pp. 1–43, 2018.

[66] Z. Chu, N. Zhang, and F. Teng, "Frequency-constrained resilient scheduling of microgrid: A distributionally robust approach," *IEEE Transactions on Smart Grid*, vol. 12, no. 6, pp. 4914–4925, 2021.

[67] J. Van de Vyver, J. D. De Kooning, B. Meersman, L. Vandevelde, and T. L. Vandoorn, "Droop control as an alternative inertial response strategy for the synthetic inertia on wind turbines," *IEEE Transactions on Power Systems*, vol. 31, no. 2, pp. 1129–1138, 2015.

[68] L. Ruttledge and D. Flynn, "Emulated inertial response from wind turbines: gain scheduling and resource coordination," *IEEE Transactions on Power Systems*, vol. 31, no. 5, pp. 3747–3755, 2015.

[69] F. Teng and G. Strbac, "Assessment of the role and value of frequency response support from wind plants," *IEEE Transactions on Sustainable Energy*, vol. 7, no. 2, pp. 586–595, 2016.

[70] L. Badesa, F. Teng, and G. Strbac, "Optimal portfolio of distinct frequency response services in low-inertia systems," *IEEE Transactions on Power Systems*, vol. 35, no. 6, pp. 4459–4469, 2020.

[71] M. Paturet, U. Markovic, S. Delikaraoglou, E. Vrettos, P. Aristidou, and G. Hug, "Stochastic unit commitment in low-inertia grids," *IEEE Transactions on Power Systems*, vol. 35, no. 5, pp. 3448–3458, 2020.

[72] F. Pérez-Illanes, E. Álvarez-Miranda, C. Rahmann, and C. Campos-Valdés, "Robust unit commitment including frequency stability constraints," *Energies*, vol. 9, no. 11, p. 957, 2016.

[73] S. M. Mousavi-Taghiabadi, M. Sedighizadeh, M. Zangiabadi, and A. S. Fini, "Integration of wind generation uncertainties into frequency dynamic constrained unit commitment

considering reserve and plug in electric vehicles," *Journal of Cleaner Production*, vol. 276, p. 124272, 2020.

[74] P. Rabbanifar and N. Amjady, "Frequency-constrained unit-commitment using analytical solutions for system frequency responses considering generator contingencies," *IET Generation, Transmission & Distribution*, vol. 14, no. 17, pp. 3548–3560, 2020.

[75] M. Shahidehpour, T. Ding, Q. Ming, J. Catalao, and Z. Zeng, "Two-stage chance-constrained stochastic unit commitment for optimal provision of virtual inertia in wind-storage systems," *IEEE Transasctions on Power Systems*, 2021.

[76] A. Mehrzad, M. Darmiani, Y. Mousavi, M. Shafie-Khah, and M. Aghamohammadi, "A review on data-driven security assessment of power systems: Trends and applications of artificial intelligence," *IEEE Access*, 2023.

[77] W. D. Oliveira, J. P. Vieira, U. H. Bezerra, D. A. Martins, and B. d. G. Rodrigues, "Power system security assessment for multiple contingencies using multiway decision tree," *Electric Power Systems Research*, vol. 148, pp. 264–272, 2017.

[78] C. Liu, K. Sun, Z. H. Rather, Z. Chen, C. L. Bak, P. Thøgersen, and P. Lund, "A systematic approach for dynamic security assessment and the corresponding preventive control scheme based on decision trees," *IEEE Transactions on Power Systems*, vol. 29, no. 2, pp. 717–730, 2013.

[79] Y. Zhang, C. Chen, G. Liu, T. Hong, and F. Qiu, "Approximating trajectory constraints with machine learning microgrid islanding with frequency constraints," *IEEE Trans. Power Syst.*, pp. 1–1, 2020.

[80] A. Venzke and S. Chatzivasileiadis, "Verification of neural network behaviour: Formal guarantees for power system applications," *IEEE Transactions on Smart Grid*, vol. 12, no. 1, pp. 383–397, 2020.

[81] Y. Du, F. Li, and C. Huang, "Applying deep convolutional neural network for fast security assessment with n-1 contingency," in *2019 IEEE Power & Energy Society General Meeting (PESGM)*. IEEE, 2019, pp. 1–5.

[82] M. Sun, I. Konstantelos, and G. Strbac, "A deep learning-based feature extraction framework for system security assessment," *IEEE Transactions on Smart Grid*, vol. 10, no. 5, pp. 5007–5020, 2018.

[83] B. Tan, J. Yang, Y. Tang, S. Jiang, P. Xie, and W. Yuan, "A deep imbalanced learning framework for transient stability assessment of power system," *Ieee Access*, vol. 7, pp. 81 759–81 769, 2019.

[84] C. Li, Y. Liu *et al.*, "Online dynamic security assessment of wind integrated power system using sdae with svm ensemble boosting learner," *International Journal of Electrical Power & Energy Systems*, vol. 125, p. 106429, 2021.

[85] B. Wang, B. Fang, Y. Wang, H. Liu, and Y. Liu, "Power system transient stability assessment based on big data and the core vector machine," *IEEE Transactions on Smart Grid*, vol. 7, no. 5, pp. 2561–2570, 2016.

[86] M. Rajabdorri, E. Lobato, and L. Sigrist, "Robust frequency constrained uc using data driven logistic regression for island power systems," *IET Generation, Transmission & Distribution*, vol. 16, no. 24, pp. 5069–5083, 2022.

[87] D. T. Lagos and N. D. Hatziargyriou, "Data-driven frequency dynamic unit commitment for island systems with high RES penetration," *IEEE Transactions on Power Systems*, vol. 36, no. 5, pp. 4699–4711, 2021.

[88] S. M. Lundberg and S.-I. Lee, "A unified approach to interpreting model predictions," in *Advances in Neural Information Processing Systems (NeurIPS)*, vol. 30, 2017. [Online]. Available: https://proceedings.neurips.cc/paper_files/paper/2017/file/8a20a8621978632d76c43dfd28b67767-Paper.pdf

[89] M. T. Ribeiro, S. Singh, and C. Guestrin, "Why should i trust you? explaining the predictions of any classifier," in *Proceedings of the 22nd ACM SIGKDD International Conference on Knowledge Discovery and Data Mining*, 2016, pp. 1135–1144.

[90] T. Huang, M. Yang, Y. Xu, and Z. Y. Dong, "Interpretability-aware ai for decision support in power system operation," *IEEE Transactions on Power Systems*, vol. 37, no. 4, pp.

3136–3147, 2022.

[91] Z. Bo, B. Zhang, J. Xu, and Y. Yuan, "Black-box model interpretation for power grid fault diagnosis based on shap," *Electric Power Systems Research*, vol. 199, p. 107425, 2021.

[92] S. Heier, *Grid integration of wind energy: onshore and offshore conversion systems.* John Wiley & Sons, 2014.

[93] X. Zhao, Y. Xue, and X.-P. Zhang, "Fast frequency support from wind turbine systems by arresting frequency nadir close to settling frequency," *IEEE Open Access Journal of Power and Energy*, vol. 7, pp. 191–202, 2020.

[94] S. El Itani, U. D. Annakkage, and G. Joos, "Short-term frequency support utilizing inertial response of DFIG wind turbines," in *2011 IEEE Power and Energy Society General Meeting.* IEEE, 2011, pp. 1–8.

[95] D. Bertsimas and J. Dunn, "Optimal classification trees," *Machine Learning*, vol. 106, no. 7, pp. 1039–1082, 2017.

[96] Y. Chen, Y. Li, J. Xiang, and X. Shen, "An optimal power flow formulation with SOCP relaxation in radial network," in *2018 IEEE 14th International Conference on Control and Automation (ICCA).* IEEE, 2018, pp. 921–926.

[97] J. A. Taylor, *Convex optimization of power systems.* Cambridge University Press, 2015.

[98] A. Dyśko, D. Tzelepis, and C. Booth, "Assessment of risks resulting from the adjustment of vector shift (VS) based loss of mains protection settings. Phase II," 2017.

[99] R. D. Zimmerman, C. E. Murillo-Sánchez, and R. J. Thomas, "MATPOWER: Steady-state operations, planning, and analysis tools for power systems research and education," *IEEE Transactions on Power Systems*, vol. 26, no. 1, pp. 12–19, 2010.

[100] [Online]. Available: https://www.powerworld.com

[101] E. Rakhshani and P. Rodriguez, "Inertia emulation in ac/dc interconnected power systems using derivative technique considering frequency measurement effects," *IEEE Transactions on Power Systems*, vol. 32, no. 5, pp. 3338–3351, 2016.

[102] L. Badesa, G. Strbac, M. Magill, and B. Stojkovska, "Ancillary services in Great Britain during the COVID-19 lockdown: A glimpse of the carbon-free future," *Applied Energy*, vol. 285, p. 116500, 2021.

[103] J. Lofberg, "YALMIP: A toolbox for modeling and optimization in MATLAB," in *2004 IEEE international conference on robotics and automation (IEEE Cat. No. 04CH37508)*. IEEE, 2004, pp. 284–289.

[104] IRENA, "Tripling renewable power capacity by 2030," 2024. [Online]. Available: https://www.irena.org/Publications/2024/Mar/Tracking-COP28-outcomes-Tripling-renewable-power-capacity-by-2030

[105] A. Hoke, V. Gevorgian, S. Shah, P. Koralewicz, R. W. Kenyon, and B. Kroposki, "Island power systems with high levels of inverter-based resources: Stability and reliability challenges," *IEEE Electrification Magazine*, vol. 9, no. 1, pp. 74–91, 2021.

[106] A.-A. B. Bugaje, J. L. Cremer, and G. Strbac, "Split-based sequential sampling for real-time security assessment," *International Journal of Electrical Power & Energy Systems*, vol. 146, p. 108790, 2023.

[107] L. Zhu and D. J. Hill, "Data/model jointly driven high-quality case generation for power system dynamic stability assessment," *IEEE Transactions on Industrial Informatics*, vol. 18, no. 8, pp. 5055–5066, 2021.

[108] I. Konstantelos, M. Sun, S. H. Tindemans, S. Issad, P. Panciatici, and G. Strbac, "Using vine copulas to generate representative system states for machine learning," *IEEE Transactions on Power Systems*, vol. 34, no. 1, pp. 225–235, 2018.

[109] Q. Wu, H. Wang, S. Xie, L. Zhang, J. Wang, Z. Dong, and T. Zhao, "Effect of heat extraction on the thermal efficiency of salt gradient solar pond," *Energy Exploration & Exploitation*, vol. 37, no. 5, pp. 1502–1515, 2019.

[110] A. Venzke, D. K. Molzahn, and S. Chatzivasileiadis, "Efficient creation of datasets for data-driven power system applications," *Electric Power Systems Research*, vol. 190, p. 106614, 2021.

[111] Y. Li, Y. Gu, and T. C. Green, "Revisiting grid-forming and grid-following inverters: A duality theory," *IEEE Transactions on Power Systems*, vol. 37, no. 6, pp. 4541–4554, 2022.

[112] Y. Zhu, Y. Gu, Y. Li, and T. C. Green, "Participation analysis in impedance models: The grey-box approach for power system stability," *IEEE Transactions on Power Systems*, vol. 37, no. 1, pp. 343–353, 2021.

[113] Y. Li, G. Geng, Q. Jiang, W. Li, and X. Shi, "A sequential approach for small signal stability enhancement with optimizing generation cost," *IEEE Transactions on Power Systems*, vol. 34, no. 6, pp. 4828–4836, 2019.

[114] D. Yang, X. Wang, M. Ndreco, W. Winter, R. Juhlin, and A. Krontiris, "Automation of impedance measurement for harmonic stability assessment of mmc-hvdc systems," in *18th Wind Integration Workshop*, 2019.

[115] F. P. Networks, "Publications," https://github.com/Future-Power-Networks/Publications, 2025, accessed: March 27, 2025.

[116] T. Roinila, M. Vilkko, and J. Sun, "Broadband methods for online grid impedance measurement," in *2013 IEEE Energy Conversion Congress and Exposition*. IEEE, 2013, pp. 3003–3010.

[117] Y. A. Familiant, J. Huang, K. A. Corzine, and M. Belkhayat, "New techniques for measuring impedance characteristics of three-phase ac power systems," *IEEE Transactions on Power Electronics*, vol. 24, no. 7, pp. 1802–1810, 2009.

[118] B. Gustavsen and A. Semlyen, "Rational approximation of frequency domain responses by vector fitting," *IEEE Transactions on power delivery*, vol. 14, no. 3, pp. 1052–1061, 1999.

[119] S. Boyd and L. Vandenberghe, *Introduction to applied linear algebra: vectors, matrices, and least squares*. Cambridge university press, 2018.

[120] W. Xu, Z. Chu, F. Capitanescu, and F. Teng, "On the incorporation of stability constraints into sequential operational scheduling," *arXiv preprint arXiv:2411.11652*, 2024.

[121] A. J. Conejo and L. Baringo, *Power system operations*. Springer, 2018, vol. 14, no. 54.

[122] A. K. Singh and B. C. Pal, "Ieee pes task force on benchmark systems for stability controls report on the 68-bus 16-machine 5-area system," *IEEE Power Energy Soc*, vol. 3, 2013.

[123] J. Lu, X. Li, H. Li, T. Chegini, C. Gamarra, Y. Yang, M. Cook, and G. Dillingham, "A synthetic texas backbone power system with climate-dependent spatio-temporal correlated profiles," *arXiv e-prints*, pp. arXiv–2302, 2023.